VISUAL CORTICAL CIRCUIT DYNAMICS IN HEALTH AND DISEASE

by

Yu Tang

A Dissertation

Submitted to the Faculty of Purdue University

In Partial Fulfillment of the Requirements for the degree of

Doctor of Philosophy

Department of Biological Sciences

West Lafayette, Indiana

May 2022

THE PURDUE UNIVERSITY GRADUATE SCHOOL
STATEMENT OF COMMITTEE APPROVAL

Dr. Alexander A. Chubykin, Chair

Department of Biological Sciences

Dr. Daniel M. Suter

Department of Biological Sciences

Dr. Maria C. Dadarlat Makin

Department of Biomedical Engineering

Dr. Scott R. Pluta

Department of Biological Sciences

Approved by:

Dr. Janice Evans

To my parents Qingxiang Wang and Baojun Tang, and my grandmother, Caiyun You, who inspired and supported me to explore my possibilities in science

ACKNOWLEDGMENTS

First and foremost, I would like to thank my advisor Dr. Alexander Chubykin for giving me the opportunity to conduct cutting-edge neuroscience research, for making this thesis work possible, for giving me experiences collaborating with researchers from diverse backgrounds, for guiding me to grow into a neuroscientist through encouragement and criticism, for kind words and support when I struggle, and for forgiving me my occasional "bipolar-like" behaviors.

I also would like to thank my advisory committee for their guidance, help, and encouragement. I thank Dr. Scott Pluta, for critical and inspiring advice during the development of my projects, and for kind caring and mentoring throughout my doctoral training. I thank Dr. Daniel Suter, for reminding me of developing my scientific communication skills, and for kind assuring of my skills. I thank Dr. Maria Dadarlat Makin, for providing inspiring comments during one of my exploratory experiments, and for kind encouragement and assuring when I question myself. I also would like to thank Dr. Kimberly Kinzig and Dr. Zhongming Liu, who gave me opportunities to get exposed to neuroscience research when I was an undergraduate student at Purdue. Their kind words and assuring of my abilities helped me build confidence in exploring my potential in neuroscience. I also thank Dr. Donald Ready for teaching me confocal microscopy imaging, and Dr. Amy Brewster for sharing antibodies during difficult pandemic time.

I also would like to thank the collaborators of my projects. I thank Dr. Gong Chen for providing the opportunity to work on the NeuroD1 gene therapy project, and for valuable discussions and help on experiments. I thank Dr. Fang Huang for providing the opportunity to get to know super resolution imaging, and valuable joint meetings to discuss intersection between imaging and neuroscience. I thank Dr. Saeed Mohammadi for providing the opportunity to get to know wireless neural recorders, and for continuing efforts in pushing the technology to be applied *in vivo*. I thank Dr. Sreeganga Chandra for providing Auxilin knockout mice, and discussions on the experiment results.

I also would like to thank my colleagues, Dr. Samuel Kissinger, Dr. Qiuyu Wu, Dr. Alexandr Pak, Mang Gao, for valuable learning experiences, discussions on sciences, and joint efforts on projects, as well as Xi Cheng, Michael Zimmermann, Carlay LaTour, and Sanghamitra Nareddula, for their kind understanding when I was too occupied and could not teach them thoroughly.

I also would like to thank our previous undergraduate researcher and lab technician Esther Ryu who helped on the NeuroD1 project and some of my failed experiments, previous undergraduate researcher Renee Towers who bravely attempted behavior experiments on mice for the NeuroD1 project, current undergraduate researcher Catherine Gervais who helped on animal surgeries and behavior training in the visual cortical synchrony project, and current undergraduate researcher Rylann Moffitt who also helped on behavior training in the visual cortical synchrony project. I also thank other graduate students who I interacted with during collaborations for joint efforts to make things happen.

Finally, I would like to thank my parents, my grandma, and other family members for their understanding, support, and encouragement for me to explore my possibilities in science. They are the light in my life.

TABLE OF CONTENTS

LIST OF FIGURES

ABSTRACT

Vision is one of the most important senses to guide behaviors, and visual functions heavily rely on the underlying neuronal circuits. The mouse visual cortex has diverse roles in encoding not only visual information, but also visually related non-visual information after learning. Its diverse functions are attributed to the dynamic functional circuits, which undergo plastic changes not only during development and learning but also during post-injury recovery throughout life. My thesis work revolves around characterizing plastic functional circuits in the mouse visual cortex using silicon probe recordings, and it covers neuronal circuit dynamics in normal visual familiarization, diseased conditions, as well as post-injury recovery.

Visual perceptual experience induces 4-8 Hz oscillations in mouse V1, which extend beyond the visual stimulation window and may encode visual familiarity. Such 4-8 Hz oscillations could reflect top-down effects and visual working memory, and may mediate inter-areal communications across visual cortical areas. To explore whether the oscillations exist and modulate activities across multiple visual cortical areas, we recorded simultaneous activities in V1 and one of the higher order visual areas (HVA), lateromedial (LM) and anterolateral (AL) areas, at a time. Following the visual perceptual experience, 4-8 Hz oscillations were enhanced in V1, as well as in both LM and AL superficial layers. After familiarization of the stimulus that maximally induced visually locked response in LM, V1 local field potentials (LFPs) became more persistently phase locked to LFPs in LM in 4-8 Hz range, but not to LFPs in AL. In parallel, after familiarization of the stimulus that maximally induced visually locked response in AL, V1 became more persistently phase-locked to AL, but not LM, in 4-8 Hz. Unit population became to spike at more consistent 4-8 Hz phases in response to the entrained spatial frequency (SF) and temporal frequency (TF), regardless of their cortical origins. Furthermore, V1 units and HVA units showed higher spiking synchrony, especially for the post-stimulus responding units, and the post-stimulus firing peaks in V1 were reduced when HVAs were optogenetically inactivated. These results demonstrated that visual experience induced persistent 4-8 Hz LFP synchrony between V1 and the HVA that had functional preference matched with the entrained SF and TF, which was accompanied by stronger 4-8 Hz modulated unit spiking and higher spiking synchrony between V1 and HVAs.

Neural circuits underlying brain functions are vulnerable to damage, including ischemic injury, leading to neuronal loss and gliosis. Recent technology of direct conversion of endogenous astrocytes into neurons *in situ* can simultaneously replenish the neuronal population and reverse the glial scar. However, whether these newly reprogrammed neurons undergo normal development, integrate into the existing neuronal circuit, and acquire functional properties specific for this circuit is not known. We investigated the effect of NeuroD1-mediated *in vivo* direct reprogramming on functional recovery in a mouse model of ischemic injury. After performing electrophysiological extracellular recordings, we discovered that visual cortex acquired direct visual responses, and fast spiking units exhibited delayed recovery of visual responses. Furthermore, units' orientation selectivity sharpened over time after NeuroD1 delivery, and optogenetically tagged converted neurons exhibited selective responses to orientations. Our results show that visual cortical responses recovered and acquired selectivity to orientations after NeuroD1 mediated gene therapy.

CHAPTER 1. INTRODUCTION

Vision is one of the most important senses to guide behaviors. The visual systems of mammals, from rodents to primates, share a lot of similarities, and the mouse visual system has been extensively used to study visual perception, as well as learning and memory. These functions heavily rely on the underlying neuronal circuits, whose computation is built through their intricate anatomical connectivity and the dynamic physiological interactions between the components. Thanks to modern technology, great progress has been made in understanding the neuronal code in the visual cortex, revealing its diverse roles for encoding not only visual information but also visually related information. The diversity could not be achieved without selectively recruiting functional circuits, which undergo plastic changes not only during development but also during learning or post-injury recovery throughout life. My thesis work revolves around characterizing plastic functional circuits in the mouse visual cortex using silicon probe recordings, and it covers neuronal circuit dynamics in normal visual familiarization, diseased conditions, as well as post-injury recovery.

1.1 The mouse visual system

Despite mice's low visual acuity compared to those of cats or primates, mice use vision to guide behaviors in many cases. When a looming stimulus that mimics an approaching predator is presented, mice manifest defensive behaviors, such as escaping or freezing (Yilmaz and Meister, 2013). When vision is perturbed, mice chase preys less efficiently (Hoy et al., 2016). In addition to simple visual detection, mice are able to visually discriminate visual features, such as contrasts, orientations (Glickfeld et al., 2013a), coherent motions (Douglas et al., 2006), visual categories (Goltstein et al., 2021), natural scenes (Yu et al., 2018), and even visual illusions (Okuyama-Uchimura and Komai, 2016; Pak et al., 2020). Hence, the mouse visual system is widely used for visual processing studies, especially the visual cortex due to its clear retinotopic organization and selective responses to visual features. Interestingly, the visual cortex has also been shown to be involved in reporting visually related non-visual information. Sustained visual response duration is associated with reward timing after a visual cue (Chubykin et al., 2013), and sustained neuronal

response is selectively expressed when mice anticipate reward (Poort et al., 2015). Hence, the mouse visual cortex can be used in studies of sensory integration and predictive coding.

1.1.1 Anatomy of the mouse visual system

In mice, the retina converts light into electrical signals, which are transmitted to subcortical structures, including the lateral geniculate thalamic nuclei (LGN, about 40% projections) and superior colliculus (SC). Neurons in the dorsal LGN (dLGN) mostly project to the mouse primary visual cortex (V1), while the neurons in the SC projects to the lateral posterior nuclei (LP). LP neurons then project directly to higher-order visual areas and V1 (Figure 1.1A) (Seabrook et al., 2017; Juavinett et al., 2020).

Mouse V1 has six layers, which are categorized by their cell subtype compositions and their connectivity to other regions (Figure 1.1B) (Harris and Shepherd, 2015; Gouwens et al., 2019; Niell and Scanziani, 2021). Layer 4 receives most of the thalamocortical inputs. Layer 2/3 sends projections to higher-order visual areas (HVAs). Projections from HVAs to V1 mostly target layer 2/3 and layer 5/6. Layer 5/6 sends projections to multiple subcortical structures. Within the cortical neuronal population, the majority of neurons are excitatory (Exc., > 80%) and the rest are inhibitory (Ihb.). Both excitatory and inhibitory neurons are widely present from layer 2 to layer 6, except that the layer 1 mostly contains neuronal processes and some inhibitory neurons. Excitatory and inhibitory neurons have many subtypes, which can be categorized by their transcriptomics, morphology, electrophysiological properties, and others. The categorization of excitatory neurons in circuit neuroscience is usually done by their layer locations, projection patterns, and molecular identities. The most popular categorization of interneurons is based on their molecular identities, and the major types are parvalbumin-positive (PV) interneurons, somatostatin-positive (SOM) interneurons, and 5-HT3AR serotonin receptor-positive interneurons. Some of the intracortical microcircuit structures of interest will be discussed later in the thesis.

The anatomical connectivity across visual cortices in mice shares similarities with primates, in that they together form a hierarchical structure and form two clusters based on their connection densities between areas, namely ventral stream and dorsal stream (Wang et al., 2012; Wang and Burkhalter, 2013). In primates, the ventral stream is considered as the “what” pathway, which processes spatial details of visual information, and the dorsal stream is considered as the

"where" pathway, which locates where the visual objects are and is responsible for visually guided actions (Milner and Goodale, 2008; Sheth and Young, 2016). The evidence of anatomical connection clusters in mice led to a lot of research in studying visual cortical network in mice and its functions (Glickfeld et al., 2014), and revealed more evidence for necessities of multiple HVAs together in visual tasks, with each HVA having biased contributions to visual feature recognition, acting to visual information, and having preferential processing in different parts of the visual fields (Milner and Goodale, 2008; Jin and Glickfeld, 2020). The anatomical connectivity between V1 and HVAs in mice also showed interconnected structures that were hierarchical or nonhierarchical (Han et al., 2018; D'Souza et al., 2022), supporting both generalized and specialized responses of HVAs associated with visual perception and related actions.

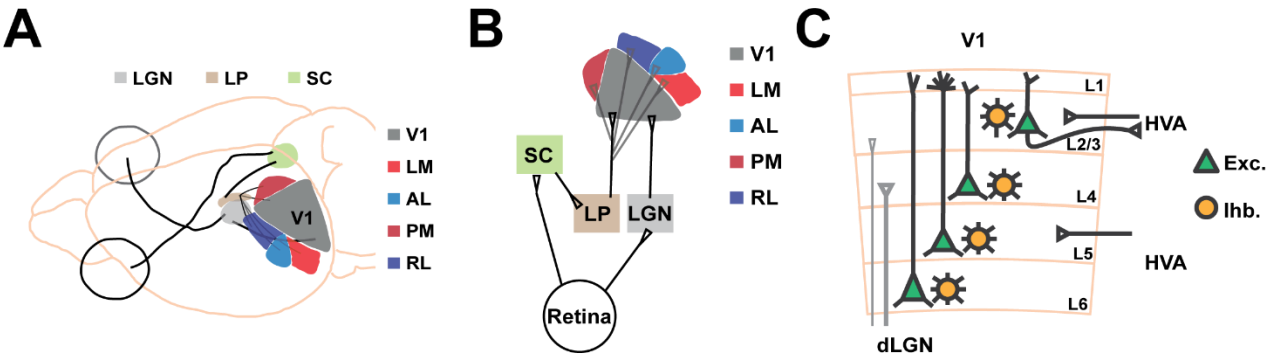

Figure 1.1 Anatomy of the mouse visual system. (A) Selected brain regions and connections between them in the mouse visual system. LGN: lateral geniculate nucleus of thalamus; LP: lateral posterior nucleus of thalamus; SC: superior colliculus; V1: primary visual cortex; LM: lateromedial visual cortex; AL: anterolateral visual cortex; PM: posteromedial visual cortex; RL: rostrolateral visual cortex. (B) Connectivity between brain regions (C) The layered structure of the mouse V1.

1.1.2 Functions of the mouse primary and higher-order visual cortical areas

Encoding visual information is the foremost function of the mouse visual cortex. In mice, dLGN neurons already start to show selective responses to orientations or directions (Piscopo et al., 2013), while the selectivity of visual cortical neurons is sharper and are not solely inherited from thalamic inputs (Niell and Stryker, 2008; Lien and Scanziani, 2018). Neurons in V1 do not form clear functional column structure based on their orientation or direction preferences (Ohki and Reid, 2007), yet the neurons that respond to adjacent visual fields are tangentially organized together to form a retinotopic map in V1 (Schuett et al., 2002; Zhuang et al., 2017). Higher-order visual cortical areas (HVAs) also form individual retinotopic maps individually, with some biased visual space representation (Garrett et al., 2014). Unlike the wide range of visual feature

preferences of V1 neurons, HVA neurons show preferential responses to spatial and temporal frequencies content of visual stimuli (Andermann et al., 2011; Marshel et al., 2011), suggesting possible parallel processing of visual features. These biased preferences could be partially attributed to biased V1 inputs (Glickfeld et al., 2013b; Kim et al., 2018). Interestingly, the selectivity of V1 neuron responses to spatial frequencies, temporal frequencies, orientations, and directions could be reduced or enhanced when HVAs are inactivated (Huh et al., 2018; oude Lohuis et al., 2021). Such alteration could be attributed to receptive field property changes, and some evidence has shown that HVA inactivation could alter V1 receptive field size (Keller et al., 2020), as well as spatial integration response (Nurminen et al., 2018; Pak et al., 2020). These feature selective V1 responses could be sharpened by mouse arousal and behavioral state (Vinck et al., 2015; Dadarlat and Stryker, 2017), as well as experience and learning (Jurjut et al., 2017; Smith et al., 2017; Gao et al., 2021), suggesting that V1 is able to integrate non-visual signals.

It has been recently shown that V1 could report non-visual information. Sustained visual cortical response duration can report reward timing (Chubykin et al., 2013). Neurons that prefer the rewarded orientation show sustained post-stimulus response only when mice correctly anticipate reward (Poort et al., 2015). Persistent oscillatory activity can report the familiar spatial frequency content of visual stimuli (Kissinger et al., 2018). A visual cortical neuron can also show a signal for spatial expectation for a reward even when a visual cue is absent (Pakan et al., 2018). At the same time, studies have also shown that HVAs are not only involved in visual perception, but also are necessary for integrating visual information for actions (Jin and Glickfeld, 2020), suggesting their capability in encoding integrated nonsensory information. Given such response specificity to non-visual information such as expectations, the visual cortex has become a model for studying predictive coding theory, which proposes that internal predictions may influence neuronal responses in V1, especially to familiar stimuli (Kissinger et al., 2020; Gao et al., 2021).

1.1.3 Visual cortical functional microcircuit

Functional cortical circuits in mouse cortical areas share a conserved canonical circuits structure (Bastos et al., 2012). The V1 canonical circuits start with thalamocortical projections synapsing on to the layer 4 neurons, and then layer 4 neurons send projections to layer 2/3 neurons. Some of layer 2/3 neurons send projections to layer 5, and some project to other regions like HVAs. Such structure is mostly preserved in the mouse visual cortex. However, recently discovered new

non-conventional connections such as intrinsic cortical feedback connections from layer 5 pyramidal cells to layer 4 fast-spiking interneurons may provide additional non-visual functions such as working memory and visual familiarity .

V1 computation for orientation and direction selectivity is partially inherited from a spatial and temporal combination of on and off receptive fields of the thalamocortical inputs (Lien and Scanziani, 2018), and is locally amplified in the cortical circuit through similarly tuned inputs (Lien and Scanziani, 2013), potentially through the cortical like-to-like connections (Ko et al., 2011). Interestingly, when a large visual stimulus activates a group of neurons, the visually evoked activity does not necessarily represent a simple summation, but rather gets suppressed (Adesnik et al., 2012; Nurminen and Angelucci, 2014). The suppressed response has been attributed to SOM interneurons that are activated by a large number of inputs. For an individual V1 neuron, its visually evoked response gets suppressed when the visual stimulus is much larger than its receptive field, which is likely associated with the inhibition from SOM interneurons and inputs from higher-order visual areas.

Another visual cortical circuit performing computations for non-visual information processing is usually associated with learning. In a task where mice need to learn licking after a visual cue to get a reward, V1 layer 2/3 neurons showed a larger response to the stimulus when mice expected to receive a reward, but a smaller response when mice missed the reward (Poort et al., 2015). In a task where mice get familiarized with a virtual tunnel containing visual cues, mouse visual cortical neurons can exhibit different responses to the same stimulus at different virtual spatial locations, and some of the neurons develop predictive responses to an upcoming visual stimulus (Fiser et al., 2016). Visual cortical neurons can also exhibit a larger response to sound when it is coupled with visual stimulus, and the larger response is likely attributed to direct inputs from the auditory cortex (Garner and Keller, 2022). The non-visual information encoding such as prediction could be resulted from distal inputs from other brain regions as well, such as cingulate cortex (ACC) (Zhang et al., 2014a; Fiser et al., 2016), and retrosplenial cortex (RSC) (Makino and Komiyama, 2015).

1.2 Neural oscillations in the visual cortex

Oscillatory changes in neuron population excitability are widely seen across brain regions in many animals, and they exhibit in different frequencies (delta: <4 Hz; theta: 4-8 Hz; alpha: 8-

12 Hz; beta: 12-30 Hz; low gamma: 30-50 Hz; high gamma: 50-80 Hz) depending on behavioral contexts. Using electroencephalography (EEG), slow frequency oscillations (delta and theta) are observed during sleep (Adamantidis et al., 2019), and the rhythm transitions to an alpha frequency when waking up, and to higher frequencies in some awake tasks, such as visual perception. These frequencies are not mutually exclusive, and slow rhythmic excitability modulates the expression of higher frequency oscillations in a lot of situations. The frequency difference can be attributed to many factors including rhythmic-firing pacemaker neurons, neuromodulation control of the pacemaker neurons, the involvement of different neuronal circuitry ensembles, the engagement of interneuron subtypes in the population activity, etc. The oscillatory activity in the visual cortex has been studied for a long time in cats, primates, humans, and recently in mice. Despite the brain size differences among species, the behavior associated oscillation frequencies are relatively conserved. High frequencies (>30 Hz) are generally considered to reflect the activity of local microcircuits that are associated with visual feature processing when feedforward visual inputs are present (Nase et al., 2003), while low frequencies (<30 Hz) during wakefulness are usually associated with attention and working memory, and can be found in multiple brain regions, such as prefrontal cortex, visual cortices, and hippocampus (Liebe et al., 2012; Tamura et al., 2017; Spyropoulos et al., 2018; Han et al., 2019). Gamma oscillation (>30 Hz) in the mouse visual cortex has been shown to be characteristic of communication with dLGN (McAfee et al., 2018; Schneider et al., 2021). Previous studies have shown that cortical PV interneurons are important for the gamma oscillation expression in the cortex (Bartos et al., 2007), while others have also shown SOM interneurons' role in low gamma oscillations (Veit et al., 2017). Recent work in mice start to reveal the presence of low frequency visual cortical oscillations in mice during viewing salient visual stimuli (Huang et al., 2020a), visual familiarization (Kissinger et al., 2018), and visually-cued associative learning (Zold and Hussain Shuler, 2015), yet whether the visual cortical low-frequency oscillation in mice mediates communication with other brain regions is not clear. Theta oscillations in mouse prefrontal and visual cortices measured using EEG have shown to be reversely correlated when a mouse performs a sustained visual attention task (Han et al., 2019). It has also been shown that the visual cortical neurons can be phase-locked to theta oscillations in the hippocampus in a visually cued virtual corridor (Fournier et al., 2020). The low frequency oscillations across visual areas are mostly studied in primates, and cumulating evidence suggested that high frequency oscillations mediated feedforward inputs from the primary visual cortex to

higher order visual cortices, and low frequency oscillations mediated feedback inputs from higher order visual cortices (Michalareas et al., 2016). Though the cellular mechanism of such directional oscillatory communication is not clear, the difference in feedforward and feedback targets, their connection strength, and interneuron subtypes may play an important role in these oscillations (Mejias et al., 2016; Cardin, 2018; Zhang and Zhang, 2021).

The functional role of 4-8 Hz oscillation in the mouse V1 still remains elusive. In *ex vivo* brain slices, cholinergic input induced theta oscillation in the hippocampus can induce synaptic plasticity, and the neurons that spike in the phase of the oscillation would induce long term potentiation (LTP), and the ones that spike out of phase of the oscillation would induce long term depression (LTD). It is likely that the visual cortical oscillation that is seen after experience and learning is a form of synaptic plasticity *in vivo* (Huerta and Lisman, 1995; Buzsaki and Draguhn, 2004). The possibility for bidirectional plasticity allows input selection, such that the inputs that align with the excitable phases are more likely to communicate with the recipient (Fries, 2005). Communication through coherence theory proposed that brain regions or neurons that have synchronized excitability fluctuation would communicate more effectively than the ones with excitability changes in different frequencies or misaligned phases. Given the longer duration of excitability window of the low frequency oscillations, the experience-induced 4-8 Hz oscillations are likely to mediate cross-regional communications, such as top-down feedback inputs to the visual cortex. The persisting rhythmic excitability fluctuation induced by visual experience would be able to allow communication cross brain areas for a longer period of time.

CHAPTER 2. VISUAL PERCEPTUAL EXPERIENCE INDUCES PERSISTENT 4-8 HZ LFP SYNCHRONY AND SPIKE SYNCHRONY BETWEEN V1 AND HIGHER ORDER VISUAL AREAS

2.1 Abstract

Visual perceptual experience induces 4-8 Hz oscillations in mouse V1, which extend beyond the visual stimulation window and may encode visual familiarity. Such 4-8 Hz oscillations could reflect top-down effects and visual working memory, and may mediate inter-areal communications across visual cortical areas. To explore whether the oscillations exist and modulate activities across multiple visual cortical areas, we recorded simultaneous activities in V1 and one of the higher order visual areas (HVA), LM and AL, at a time. Following the visual perceptual experience, 4-8 Hz oscillations were enhanced in V1, as well as in both LM and AL superficial layers. After familiarization of the stimulus that maximally induced visually locked response in LM, V1 LFPs became more persistently phase locked to LFPs in LM in 4-8 Hz range, but not to LFPs in AL. In parallel, after familiarization of the stimulus that maximally induced visually locked response in AL, V1 became more persistently phase-locked to AL, but not LM, in 4-8 Hz. Unit population became to spike at more consistent 4-8 Hz phases in response to the entrained SF and TF, regardless of their cortical origins. Furthermore, V1 units and HVA units showed higher spiking synchrony, especially for the post-stimulus responding units, and the post-stimulus firing peaks in V1 were reduced when HVAs were optogenetically inactivated. These results demonstrated that visual experience induced persistent 4-8 Hz LFP synchrony between V1 and the HVA that had functional preference matched with the entrained spatial frequency (SF) and temporal frequency (TF), which was accompanied by stronger 4-8 Hz modulated unit spiking and higher spiking synchrony between V1 and HVAs.

2.2 Introduction

Recent studies have demonstrated that neuronal responses in the mouse visual cortex may convey information not only about the features of the stimulus but also visually related non-sensory information. Neurons that preferentially respond to rewarded visual stimulus are less responsive when mice correctly reject unrewarded trials than when they do not (Poort et al., 2015).

This non-sensory expectation information may also be encoded in the neuronal activity persisting beyond the time of the initial stimulus, and it has been shown that sustained response duration of visual cortical neuron can report visually cued reward timing (Chubykin et al., 2013; Zold and Hussain Shuler, 2015). Interestingly, visual perceptual experience alone is also able to induce sustained neuronal activity in the mouse primary visual cortex (V1), and manifests as persistent oscillatory activity in the 4-8 Hz range (Kissinger et al., 2018; Gao et al., 2021), in addition to population response amplitude changes (Frenkel et al., 2006; Kissinger et al., 2018). These oscillations are specifically expressed when familiar visual features, such as spatial frequency, are presented (Kissinger et al., 2018), suggesting its association with visual familiarity. Sustained theta oscillations have been widely studied in working memory tasks, across brain regions including primate V4 and prefrontal cortex, rodent hippocampus and prefrontal cortex, and recently mouse primary visual cortex (V1) (Lee et al., 2005; Rutishauser et al., 2010; Liebe et al., 2012; Wang and Dragoi, 2015; Tamura et al., 2017). The experience induced low-frequency oscillation is likely associated with visual working memory, and is better posited to mediate long-range network communications, such as inter-areal communication between visual cortices (van Kerkoerle et al., 2014; Bastos et al., 2015b), because of their longer excitability duration (Engel et al., 1991; Buzsaki and Draguhn, 2004; Fries, 2005; Bastos et al., 2015a).

Recent studies have demonstrated that even simple visual feature processing was distributed in V1 and HVAs. The HVAs are functionally specialized (Andermann et al., 2011; Marshel et al., 2011; Han et al., 2020; Siegle et al., 2021) and form two hierarchical clusters both anatomically and functionally (Wang et al., 2011; Wang et al., 2012; Murakami et al., 2017; Smith et al., 2017). Among the HVAs, the lateromedial (LM) area and the anterolateral (AL) area are considered as gateways to these two clusters (Wang et al., 2011; Wang et al., 2012). The inter-areal connections between visual cortical areas are also functionally specialized (Glickfeld et al., 2013b; Kim et al., 2018) and play important roles in visual feature selectivity, receptive field properties, and responses to visual illusions (Huh et al., 2018; Marques et al., 2018; Nurminen et al., 2018; Keller et al., 2020; Pak et al., 2020). Optogenetic suppression of LM or AL impairs mouse's discriminability in perceiving orientations and contrasts, and suppressing the posteromedial (PM) area impairs initiating actions following sensory perception more than sensory perception alone in mice (Jin and Glickfeld, 2020). Inhibiting feedback from LM to V1 also partially impairs mouse visual detection of contrast changes (Goldbach et al., 2021).

To investigate whether visual perceptual experience induces oscillations in HVAs and whether V1 and HVA interactions are modulated by oscillations following the experience, we recorded simultaneous activity from V1 and LM or from V1 and AL using two silicon probes. Here, we report universal expression of 4-8 Hz oscillations in V1, LM, and AL after visual experience, but region-specific 4-8 Hz phase-locking between V1 and a selective HVA. After mice familiarized a stimulus that maximally induced LM response, LM, but not AL, became more phase locked with V1 in 4-8 Hz range in response to the familiar stimulus. Likewise, after mice familiarized a stimulus that maximally induced AL response, AL, but not LM, became more phase locked with V1 in 4-8 Hz range. Additionally, unit population became to spike in a visually locked cluster and post-stimulus clusters after visual experience, and they spiked at more consistent 4-8 Hz phases in relation to local LFPs, regardless of their cortical origins. Units with visually locked firing peaks in V1 exhibited either increased or decreased spiking synchrony with units in LM and AL after visual experience, and units with post-stimulus firing peaks in V1 exhibited overall increased spiking synchrony with units in both LM and AL. Additionally, optogenetic inhibition of HVAs further demonstrated that HVA provided top-down modulation of V1 post-stimulus spiking clusters.

These results, for the first time, characterized experience induced 4-8 Hz oscillations in mouse visual cortices, 4-8 Hz LFP synchrony between V1 and the HVA that had visual feature preference matched the entrained SF and TF, as well as stronger 4-8 Hz modulated unit spiking and higher inter-areal spiking synchrony, especially for units with post-stimulus firing peaks, suggesting the role of experience induced 4-8 Hz oscillations in mediating inter-areal functional communications even when external visual input was absent.

2.3 Materials and methods

2.3.1 Animals

Male and female C57BL/6 mice (Jackson Lab) at the age of 2-3 months were used for all experiments. Mice were housed in 12-hour light/dark cycle with full access to water and chow food. All animal use was approved by Purdue IACUC and followed NIH guidelines.

2.3.2 Headplate installation and virus injection

Before surgeries, mice were first anesthetized using 5% isoflurane in oxygen or room air (SomnoSuite system) in an induction chamber. After deep anesthesia was confirmed by a foot pinch, mice were transferred to a stereotaxic frame (Kopf or NeuroStar) and maintained anesthetized using 1.5-2% isoflurane delivered through a nose cone. A heating pad was put underneath the mouse's body to prevent hypothermia. Eye ointment was applied to the mouse eyes to prevent dryness. The skin over the mouse skull was removed using sterile scissors, and 3% hydrogen peroxide was applied to the skull to remove connective tissues. V1, LM and AL were labeled with a permanent marker using stereotaxic coordinates (relative to lambda: V1: ±2.8 mm lateral, 0.5 mm anterior; LM: ±4.0 mm lateral, 1.0mm anterior; AL: ±3.8 mm lateral, 2.4 mm anterior). For some mice, retrograde or antegrade viruses that carry fluorescence (AAV1-CAG-tdTomato, rgAAV-CAG-GFP, Addgene #59462, #37825) were injected into V1 to label HVAs (25-30 nl at 300 and 600 μm below the brain surface, Nanojet III). For LM optogenetic inhibition experiments, 50 nl of AAV5-CAG-ArchT-GFP was locally injected in LM (±4.0 mm lateral, 1.0 mm anterior to the lambda) at 300 and 700 μm below the brain surface. A gold-plated reference pin (WPI 5482) was inserted through the skull and above brain surface (0.5 mm anterior to the bregma), and a customized headplate was placed on top of the skull. The skull, the reference pin, and the headplate were covered with Metabond (Parkell S380) at the end. Carprofen (Rimadyl, 0.01 ml/g of 0.05 mg/ml for each mouse) and enrofloxacin (Baytril, 0.005 ml/g of 1 mg/ml for each mouse) were subcutaneously injected to the mice for three days post-surgery. Three weeks after the surgeries, mice started habituation to the head-fixation setup.

2.3.3 Visual experience paradigm and visual stimulation

To let the mice habituate to the setup, mice were head-fixed while allowed to freely run on a customized treadmill in a dark environment for at least 1.5 hour per day for more than 3 days. A luminance linearly calibrated monitor was placed 20cm in front of the mouse showing a gray screen during the habituation. Visual stimuli were displayed during the passive visual experience and recording sessions. For the visual stimuli, a pink noise picture was first spatially filtered around five spatial frequencies (0.015, 0.03, 0.06, 0.12, 0.24 cycles/degree). For each filtered pink noise image, its light intensity at each pixel changed in sinusoidal functions of time at five temporal

frequencies (0.75, 1.5, 3, 6, 12 Hz), which, combined, generates 25 total pink noise movies. The pink noise image (1920x1080 pixels) was first generated using Matlab and then processed using Python. Visual stimuli were displayed using PsychoPy. For the passive visual experience, either one of two pink noise movies were used (0.12 cycles/degree and 0.75 Hz or 0.03 cycles/degree and 6 Hz). During the visual experience, one pink noise movie was presented for 0.2 s in each trial, for 200 trials per day for 4-6 days, with a variable 5.5-7.5 s gray screen in between trials. During recording sessions, the stimulus used for the visual experience was presented repetitively for 20 trials, followed by pseudorandom presentations of 25 pink noise movies with 20 trials for each, and 5.5-7.5 s inter-trial intervals.

2.3.4 Extracellular recording preparation

After habituation or visual experience, extracellular activities in the visual cortex were recorded in head-fixed mice. One day before the recording, fluorescence expressions in HVAs were examined under a stereoscope using a portable lamp (NIGHTSEA). Fluorescence was excited through a thinned skull over pre-labeled areas and was examined using fluorophore compatible filters attached on the stereoscope. If bright fluorescence showed up around the pre-labeled HVA location, the HVA probe was inserted at the brightest fluorescence location the next day. In the case of dim fluorescence labeling, the HVA probe was inserted at the pre-labeled location. The V1 probe was inserted at the pre-labeled V1 location. On the day of extracellular recording, two craniotomies were made over V1 and one HVA when the mouse was anesthetized using isoflurane on the stereotaxic frame. The mouse was then transferred to the head-fixation setup, and two 64 channel silicon probes (Shobe et al., 2015) were positioned above the two craniotomies using micromanipulators (NewScale). Sterile saline was added on top of the brain surface before probe insertion. For some experiments, probes were dipped in fluorescent dye (DiD or DiO, Thermofisher, V22887, V22886) to label probe tracks. The probes were inserted perpendicular to the surface of the brain at the speed of 50 μm/min to a depth of 950μm. Ten minutes after probe insertions, data acquisition started.

For optogenetics experiments, the silicon probe recording preparation was similar to what previously described (Kissinger et al., 2018; Tang et al., 2021). In addition to silicon probe insertion, an optical fiber (Thorlabs, CFMLC12U-20 connected to FT200EMT, Ø200 μm Core, 0.39 NA,) was placed above brain surface. The optical fiber was connected to a 532 nm laser

(OEM laser), which was triggered on by a TTL signal. Before experiments, the laser light power was measured at the tip of the optical fiber using a power meter (Thorlabs PM121D), and the power was kept between 4.5-10 mW during experiments.

2.3.5 Data acquisition

Data was acquired at 20 kHz using 64 channel silicon probes, Intan headstages, and OpenEphys (Siegle et al., 2017) acquisition system. Each trial recording was triggered using a TTL signal, and the visual stimulus onset timestamps were recorded by another TTL signal. Raw data was 300 Hz low-pass filtered and down-sampled to 1 kHz for LFP analysis, and was band-pass filtered between 300-6000 Hz for spike clustering using Kilosort/Kilosort2. Clustered units were manually curated in Phy to remove noisy units. LFP and clustered spike data were analyzed using Python.

2.3.6 Mouse perfusion and histology

For some mice, brain tissue was extracted to visualized probe tracks, similarly to previously described (Tang et al., 2021). Briefly, after extracellular recordings, mouse was anesthetized with ketamine and xylazine and the anesthesia status was checked by a firm foot pinch. Once no reflex observed after a foot pinch, an incision was made at the mouse's abdomen, and the heart was exposed after removing the skin and muscle. Mouse tissue was first perfused with 1x PBS until the liver cleared, then perfused with 4% PFA in PBS to fix the tissue. Brain tissue was extracted and sliced (50-100 μm) using a vibratome, and brain slices were imaged using a confocal microscope. Mouse brain reference atlas was mapped to the brain slice using Allen CCFv3.

2.3.7 Data acquisition, analyses, and statistics

For LFP analysis, LFPs were first separated based on cortical depths. Within each recording, the LFP with the largest amplitude within 50-150 ms post- visual stimulation onset was identified as the middle layer LFP for each channel column. Then, the middle layer boundaries were identified as the depths 100μm above and below the middle layer LFP channel. The LFP with the largest amplitude within 50-1000 ms post- visual stimulation onset were then selected within the channels above the middle layer upper boundary as the superficial layer LFP, and below the

middle layer lower boundary as the deep layer LFP. Oscillation peak amplitudes were quantified using the minimal values within three time windows (50-150 ms, 250-350 ms, 450-600 ms post-stimulus onset). Power spectra of LFPs were calculated using the Welch's method. For the inter-areal LFP phase-locking analysis, LFPs were filtered at multiple frequencies between 2-90 Hz using the Morlet wavelet method. LFP phases at each frequency were acquired using Hilbert transformation, and the inter-areal phase differences were calculated for each trial, and the vector sum of the phase differences across 20 trials were calculated as the phase-locking value (PLV) for each LFP pair. PLV was calculated using $\left|\frac{1}{N}\sum_{n=1}^{N} e^{j\Delta\varphi_n(t)}\right|$, where N is the number of trials, and $\Delta\varphi_n(t)$ is the phase difference at time *t* (Liebe et al., 2012; Aydore et al., 2013).

For single unit analysis, peristimulus time histograms (PSTHs) were calculated for each unit by smoothing the spike histogram using a Gaussian kernel (with 30 ms as one standard deviation), and then the normalized response was calculated using the Z-score of each unit's PSTH ((FR_t-mean($FR_{t0\text{-}t1}$))/std($FR_{t0\text{-}t1}$)). To identify preferred SF and TF of each visual cortical area, unit population responses to SFs and TFs were first normalized by the largest response within each mouse to make the largest response to 1. Then the normalized responses to 25 features were averaged across mice to get the unit population normalized response heatmap for each area. To identify the hotspot of the heatmap for each visual cortical area, the original 5x5 map was first upsampled to 50x50 using linear interpolation and smoothed using a 2D gaussian filter (sigma=5 heatmap pixels). The pixel that had the highest value was selected as the hotspot for each region, and the corresponding SF and TF were considered as the preferred feature. For intra-areal spike-phase analysis, the LFP from the channel where the unit showed the largest spike amplitude was chosen for each unit. For inter-areal spike-phase analysis, layer 2/3 LFPs were used. The phases of the Butterworth band pass filtered LFP at spike times of each trial were used for further spike-phase consistency analysis. To quantify spike phase consistency of each unit, a bias-free measure of pairwise-phase consistency (PPC) for each unit was used (Vinck et al., 2010). PPC was calculated using $\frac{2}{N*(N-1)} * \sum_{n=1}^{N-1}\sum_{m=n+1}^{N}\cos(d_{(\varphi_m,\varphi_n)})$, where *N* is the number of spikes of a unit, and $d_{(\varphi_m,\varphi_n)}$ is the angular distance between phases of spike *m* and spike *n*.

For spike train cross correlation analysis, jitter corrected and firing rate normalized cross correlation (50 ms jitter window) was calculated for all possible simultaneously recorded unit pairs (Smith and Kohn, 2008; Jia et al., 2013; Siegle et al., 2021). Unit pairs that showed larger than two

standard deviations (baseline ±50 ms from zero) within ±5 ms from zero were considered as "highly synchronized pairs" (Salkoff et al., 2015). For the "highly synchronized pairs" (less than 5% of all possible inter-areal unit pairs), the tight synchronization index was computed using the area under the curve within ±5 ms from zero. For other unit pairs, the synchronization index was computed using the area under the curve within ±50 ms from zero.

Statistical tests were performed using statistical packages from SciPy, Pingouin (Vallat, 2018a), and Astropy. Data normality was tested using Shapiro-Wilk test. For normally distributed data, student's t-tests were used. For non-normally distributed data, Mann–Whitney U tests were used. P values of multiple comparisons were corrected by keeping the false discovery rate at 5% using the Benjamini & Hochberg (FDR-BH) method. For comparisons between circular data distributions, Kuiper test was used.

2.4 Results

To record simultaneous activity in V1 and HVAs, we used two silicon probes: one to record activity from V1 and one to record activity from a HVA (LM or AL) in head-fixed awake mice (Figure 2.1A). Due to proximity of the visual cortical areas and spatial constraints of the equipment that we used, only two areas were recorded at a time. We first characterized HVAs' functional preferences for spatial frequencies (SFs) and temporal frequencies (TFs) using pink noise stimuli that were spatially filtered around five SFs with the light intensity of each pixel changed in sinusoidal functions at five TFs (Figure 2.1A), which in turn form twenty five SF/TF combinations. To optimally target HVAs, retrograde or anterograde adeno-associated viruses (AAV) that carried GFP or tdTomato were injected in V1 at 3 weeks prior to recordings, to label projections between V1 and HVAs, thus labeling HVAs. Before recordings, the fluorescence in HVAs was checked under a stereoscope and used to guide probe insertion together with stereotaxic coordinates. Representative histology showed GFP labeling V1 and LM (Figure 2.1B, top), tdTomato labeling AL/RL (Figure 2.1B, middle), and probe insertions in HVAs. Functional preferences of the visual areas were characterized using unit population averaged responses. Within each mouse, unit firing rates were averaged across the population for each stimulus, then 25 responses were normalized by dividing by the largest response. Finally, for each region, the normalized responses were averaged across all mice and shown in heatmaps (Figure 2.1C-E).

Figure 2.1. 4-8 Hz oscillations were enhanced in superficial layers of V1 and LM after entrainment of SF and TF that matched LM's functional preference. (A)The experimental setup. Extracellular activity in V1 and a higher-order visual area (LM or AL) were recorded simultaneously in a head-fixed awake mouse running on a treadmill. 25 pink noise stimuli that were spatially filtered around five spatial frequencies (SFs) with pixel light intensity changed at five temporal frequencies (TFs) were presented. (B) Representative histology showed fluorescence labeling of V1 and higher-order visual areas (green-LM, red-AL) which was achieved by injecting either retrograde or anterograde AAV in V1. The brain atlas was mapped to the brain slice using Allen CCFv3. Probes were dipped in DiD or DiO for labeling recording locations. A representative brain slice showed the probe track for LM recording in red, and another slice showed the probe track for AL recording in green. (C) Averaged visually locked responses of V1 units across mice in responses to five SFs and five TFs were plotted in heatmaps. The visually locked firing rates of unit population in responses to stimuli were normalized (25 responses normalized to 0-1 range) within each mouse, and then averaged and plotted in heatmaps. N=18 mice. (D) Averaged visually locked responses of LM units across mice in responses to five SFs and five TFs were plotted in heatmaps. The visually locked responses were normalized firing rates (25 responses normalized to 0-1 range) within each mouse. N=9 mice. (E) Averaged visually locked responses of AL units across mice in responses to five SFs and five TFs were plotted in heatmaps. The visually locked responses were normalized firing rates (25 responses normalized to 0-1 range) within each mouse. N=6 mice. (F) The SF and TF that induced the largest response in LM was used in the visual experience (SF=0.12 cpd, TF=0.75 Hz). The same stimulus was presented for 200 repeats per day for 4-6 days. Averaged LFP traces across mice before and after visual experience were shown below. (G) Negativity peak amplitudes (the median value of negativity peak amplitudes within 700 ms post stimulus onset for each LFP trace) were plotted. Data were presented as mean ± 68% CI. V1: N_{pre}=54 LFPs, 18 mice, N_{post}=42 LFPs, 14 mice; LM: N_{pre}=45 LFPs, 15 mice, N_{post}=30 LFPs, 10 mice; AL: N_{pre}=36 LFPs, 12 mice, N_{post}=21 LFPs, 7 mice. V1: Sup.: common language effect size (CLES)=0.637, p=0.016; Mid.: CLES=0.709, p=3.64×10^{-4}; Deep: CLES=0.735, p=1.15×10^{-4}; LM: Sup.: CLES=0.759, p=4.71×10^{-4}; Mid.: CLES=0.521, p=0.758; Deep: CLES=0.445, p=0.631; AL: Sup.: CLES=0.590, p=0.396; Mid.: CLES=0.436, p=0.427; Deep: CLES=0.606, p=0.396. Mann-Whitney U test with FDR-BH correction. (H) Power spectra of superficial layer LFPs within 700 ms post stimulus onset. Data were represented as mean ± 68% CI. V1: 4-8 Hz: CLES=0.705, p=5.46×10^{-4}, 8-12 Hz: CLES=0.726, p=3.56×10^{-4}, 12-30 Hz: CLES=0.601, p=0.097, 30-50 Hz: CLES=0.427, p=0.197, 50-80 Hz: CLES=0.290, p=5.22×10^{-4}; LM: 4-8 Hz: CLES=0.691, p=0.018, 8-12 Hz: CLES=0.577, p=0.329, 12-30 Hz: CLES=0.490, p=0.884, 30-50 Hz: CLES=0.378, p=0.125, 50-80 Hz: CLES=0.316, p=0.018; AL: 4-8 Hz: CLES=0.641, p=0.096, 8-12 Hz: CLES=0.634, p=0.096, 12-30 Hz: CLES=0.362, p=0.096, 30-50 Hz: CLES=0.364, p=0.096, 50-80 Hz: CLES=0.236, p=0.005, Mann-Whitney U test with FDR-BH correction. (I) 4-8 Hz power ratios (post- to pre- visual experience) in responses to 5 SFs and TFs were plotted in heatmaps. Statistically significant differences in 4-8 Hz power between post- and pre-experience for each visual stimulus were labeled. Mann-Whitney U test with FDR-BH correction. See extended table 1-1 for detailed statistics. *-p<0.05, **-p<0.01, ***-p<0.001, n.s.-p>0.05.

Figure 2.1 continued

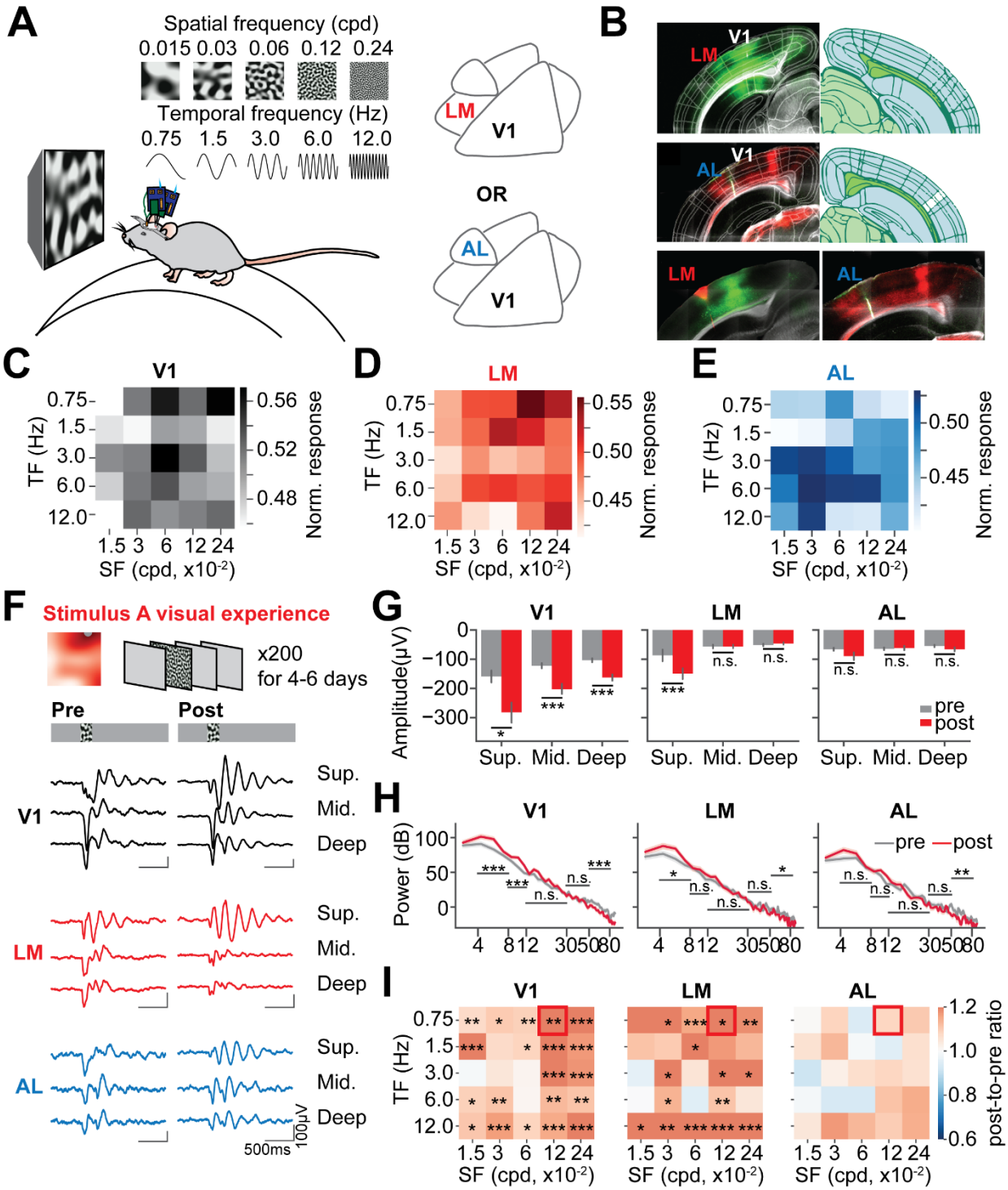

2.4.1 Persistent 4-8 Hz oscillations in V1 and HVA superficial layers after visual experience

To maximally induce LM activity during the visual experience, the stimulus that induced the largest visually locked response in LM was used (Figure 2.1F). The SF and TF were chosen by selecting the hot spot of the LM response heatmap (SF=0.12 cycles per degree (cpd), TF=0.75 Hz, details see Methods). During the visual experience, mice were head-fixed in front of the monitor, and the stimulus (200 ms duration) was presented 200 times with 5.5-7.5s inter-stimulus interval between trials, per day for four to six days. Following the visual experience, the averaged local field potential (LFP) in V1 superficial (sup.), middle (mid.) and deep layers showed more prominent oscillatory activity (Figure 2.1F) in response to the entrained SF and TF. The superficial layer LFPs in LM and AL also showed similar oscillations with smaller amplitudes. The median amplitudes of V1 oscillation troughs within 700 ms post-stimulus onset were significantly larger in sup., mid., and deep layers, after entrainment of SF and TF that matched LM's functional preference (Figure 2.1G left). The median amplitudes of the oscillation troughs in LM superficial layer LFPs also showed significant increases (Figure 2.1G middle), while the median amplitudes of the oscillation troughs in AL did not show significant changes at any cortical depth (Figure 2.1G right). We then focused on analyzing superficial layer LFPs in V1, LM, and AL, because of the prevalence of the oscillations in the superficial layers and the existence of inter-areal feedforward and feedback projections in the superficial layer of V1. To examine the power of superficial layer oscillations across frequency bands, power spectra of trial averaged LFPs within 700 ms post-stimulus onset were calculated for each LFP. Both V1 and LM superficial layer LFPs showed increased 4-8 Hz power post-experience, but AL superficial layer LFPs did not show significant change in 4-8 Hz power (Figure 2.1H). To inspect SF and TF specificity of the oscillation, the ratios of post- to pre- experience 4-8 Hz power in relation to SFs and TFs were plotted in heatmaps (Figure 2.1I). The 4-8 Hz power in V1 and LM significantly increased in response to the entrained SF and TF, but also increased in responses to other SFs and TFs to a less extent. The 4-8 Hz power in AL did not show significant changes in response to any stimulus.

To investigate whether the enhanced 4-8 Hz oscillation can be induced in other HVAs, such as AL, we recorded activity in V1, LM, and AL in another set of mice who experienced a stimulus that matched AL's SF and TF preference (SF=0.03 cpd, TF=6 Hz). Following the entrainment of SF and TF that matched AL's functional preference, the averaged LFP traces in V1, LM, and AL showed more prominent oscillations in response to the entrained SF and TF

(Figure 2.2A), and the 4-8 Hz power increased significantly in V1 and AL, as well as in LM (Figure 2.2B). When we compared 4-8 Hz power between post- and pre- experience in relation to SFs and TFs, significant increases were found in V1, LM, and AL, in response to not only the entrained SF and TF, but also other SFs and TFs that were close to the entrained SF and TF (Figure 2.2C). These results demonstrated that visual experience could induce stronger 4-8 Hz oscillations in superficial layers of V1, LM, and AL.

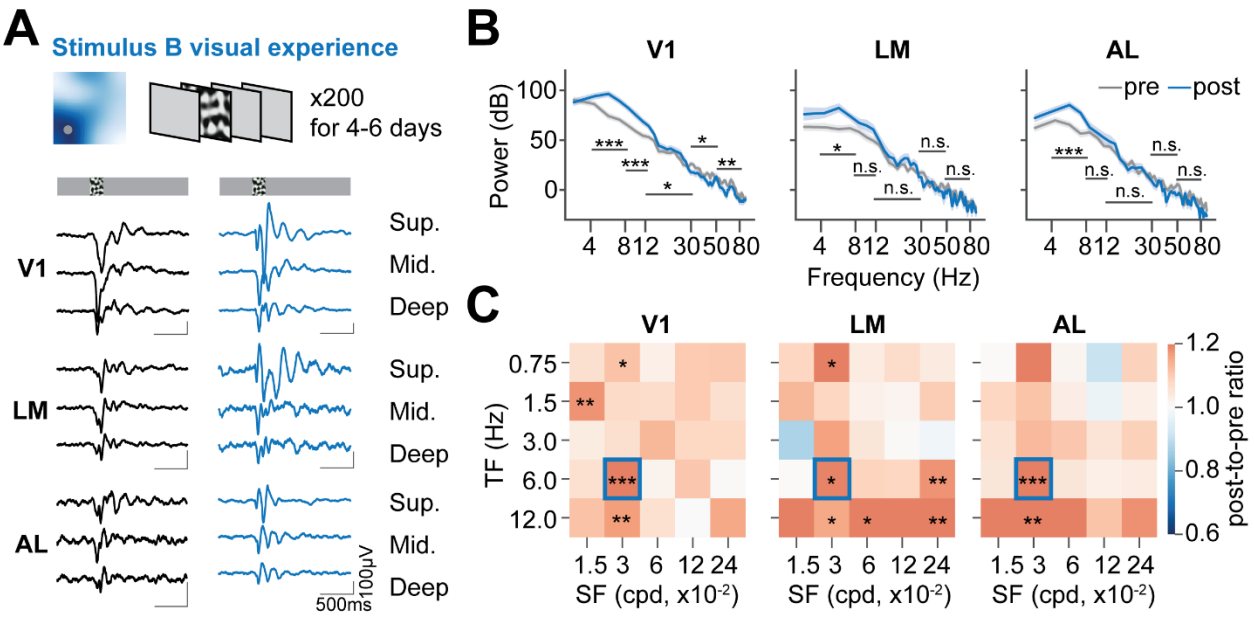

Figure 2.2. 4-8 Hz oscillations were enhanced in superficial layers of V1, LM, and AL after entrainment of SF and TF that matched AL's functional preference. (A) The SF and TF that induced the largest visually locked response in AL was used in the visual experience (SF=0.03 cpd, TF=6 Hz). The same stimulus was presented for 200 repeats per day for 4-6 days. Averaged LFP traces across mice before and after visual experience were shown below. V1: N_{pre}=54 LFPs, 18 mice, N_{post}=42 LFPs, 14 mice; LM: N_{pre}=45 LFPs, 15 mice, N_{post}=21 LFPs, 7 mice; AL: N_{pre}=36 LFPs, 12 mice, N_{post}=21 LFPs, 7 mice. (B) Power spectra of superficial layer LFPs within 700 ms post visual stimulus onset. Data were represented as mean ± 68% CI. V1: 4-8 Hz: CLES=0.785, p=1.02x10^{-5}, 8-12 Hz: CLES=0.752, p=4.93x10^{-5}, 12-30 Hz: CLES=0.639, p=0.024, 30-50 Hz: CLES=0.375, p=0.035, 50-80 Hz: CLES=0.331, p=7.21x10^{-3}; LM: 4-8 Hz: CLES=0.735, p=0.011, 8-12 Hz: CLES=0.604, p=0.259, 12-30 Hz: CLES=0.593, p=0.258, 30-50 Hz: CLES=0.413, p=0.259, 50-80 Hz: CLES=0.398, p=0.259; AL: 4-8 Hz: CLES=0.832, p=1.71x10^{-4}, 8-12 Hz: CLES=0.590, p=0.330, 12-30 Hz: CLES=0.419, p=0.470, 30-50 Hz: CLES=0.381, p=0.231, 50-80 Hz: CLES=0.337, p=0.106, Mann-Whitney U test with FDR-BH correction. (C) 4-8 Hz power ratios (post- to pre- visual experience) in responses to 5 SFs and TFs were plotted in heatmaps. Statistically significant differences in 4-8 Hz power between post- and pre- experience for each visual stimulus were labeled. See extended table 2-1 for detailed statistics. *-p<0.05, **-p<0.01, ***-p<0.001, n.s.-p>0.05

2.4.2 The HVA with functional preference matching the entrained SF and TF became phase locked to V1 in 4-8 Hz after visual experience

Reliable inter-aerial communications may require phase coherence between areas (Fries, 2005; Bastos et al., 2015a; Kohn et al., 2020). To investigate whether there was phase-locking between V1 and HVAs, we calculated phase locking values (PLV) between superficial layer LFPs from V1 and LM, or from V1 and AL, respectively. Following the entrainment of SF and TF that matched LM's functional preference, V1 and LM exhibited enhanced phase-locking in 4-8 Hz range persisting beyond the visual stimulus time window (Figure 2.3A), and the 4-8 Hz PLV averaged within 700 ms post-stimulus onset was significantly increased post-experience (Figure 2.3B). Interestingly, the phase difference between V1 and LM (V1 phase – LM phase) within 700 ms post-stimulus onset showed a more concentrated and right-shifted distribution after visual experience (Figure 2.3C), suggesting a more constant delay in LM response. To examine whether the increased 4-8 Hz phase-locking between V1 and LM was specifically expressed in response to the entrained SF and TF, we built a comprehensive two-dimensional map with median 4-8 Hz PLVs (within 700 ms post-stimulus onset) of all LFP pairs in response to each stimulus and compared the PLVs between post- and pre- visual experience for each stimulus. V1-LM PLVs increased in response to the entrained SF and TF, as well as to other stimuli that shared similar SF or TF with the entrained SF and TF. Meanwhile, the V1-LM PLVs significantly decreased in responses to stimuli that had distinct SF or TF from the entrained SF and TF (Figure 2.3D). On the contrary, there was no significant change in PLVs between V1 and AL in response to the entrained SF and TF (Figure 2.3E, F). The distribution of phase differences between V1 and AL within 700 ms post-stimulus onset did not show significant changes after visual experience (Figure 2.3G). Intriguingly, the V1-AL PLVs were reduced in response to the stimuli that had SFs or TFs distinct from the entrained SF and TF, though no significant change was found in response to the entrained SF and TF (Figure 2.3H).

.

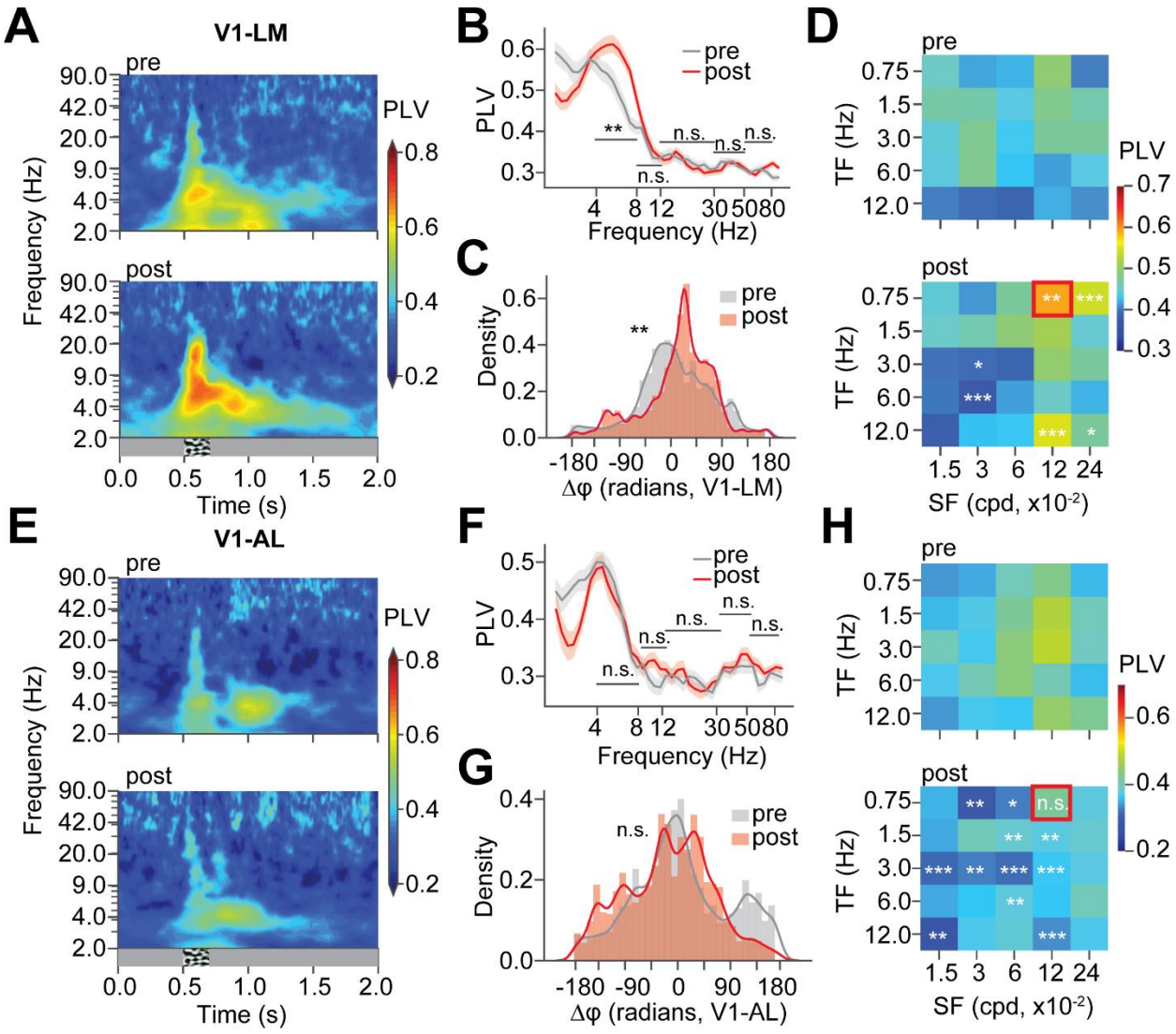

Figure 2.3. LM, but not AL, became more phase locked to V1 in 4-8 Hz after entrainment of SF and TF that matched with LM's functional preference. (A) Phase-locking values (PLV) of V1 and LM LFP pairs over time across frequencies were averaged and plotted in heatmaps. N_{pre}=90 LFP pairs, 10 mice; N_{post}=90 LFP pairs, 10 mice. (B) PLV values (median within 700 ms post stimulus onset) of V1-LM LFP pairs across frequencies. Data were presented as mean ± 68% CI. 4-8 Hz: CLES=0.648, p=3.06x10^{-3}, 8-12 Hz: CLES=0.539, p=0.611, 12-30 Hz: CLES=0.506, p=0.885, 30-50 Hz: CLES=0.454, p=0.611, 50-80 Hz: CLES=0.492, p=0.885, Mann-Whitney U test with FDR-BH correction. (C) 4-8 Hz oscillation phase differences between V1 and LM (within 700 ms post stimulus onset) were plotted in density plots. D=0.323, p=5.02x10^{-3}, Kuiper test. (D) Median 4-8 Hz PLV values of V1-LM LFP pairs in responses to 5 SFs and 5 TFs were plotted in heatmaps. Statistically significant differences between post- and pre- experience were labeled. See extended table 3-1 for detailed statistics. (E) PLVs of V1 and AL LFP pairs over time across frequencies were averaged and plotted in heatmaps. N_{pre}=81 LFP pairs, 9 mice; N_{post}=54 LFP pairs, 6 mice. (F) PLV values (median within 700 ms post stimulus onset) of V1-AL LFP pairs across frequencies. Data were presented as mean ± 68% CI. 4-8 Hz: CLES=0.484, p=0.758, 8-12 Hz: CLES=0.606, p=0.192, 12-30 Hz: CLES=0.473, p=0.745, 30-50 Hz: CLES=0.528, p=0.745, 50-80 Hz: CLES=0.581, p=0.277, Mann-Whitney U test with FDR-BH correction. (G) 4-8 Hz oscillation phase differences between V1 and AL (within 700 ms post stimulus onset) were plotted in density plots. D=0.198, p=0.747, Kuiper test. (H) Median 4-8 Hz PLV values of V1-AL LFP pairs in responses to 5 SFs and 5 TFs were plotted in heatmaps. Statistically significant differences between post- and pre- experience for each stimulus were labeled. See extended table 3-2 for detailed statistics. *-p<0.05, **-p<0.01, ***-p<0.001, n.s.-p>0.05.

To further test whether such synchrony could be induced between V1 and AL, we looked at the PLVs between areas in another set of mice after entrainment of SF and TF that matched AL's functional preference. Similarly to the entrainment described earlier, we found 4-8 Hz phase-locking between V1 and AL persisting beyond visual stimulus time window post-experience (Figure 2.4A,B), but V1 and LM did not show as strong of phase-locking as between V1 and AL (Figure 2.4E,F). The distribution of phase differences between V1 and LM did not show changes in the variability but were slightly, but significantly right shifted (Figure 2.4C), whereas phase differences between V1 and AL within 700 ms post-stimulus onset became more concentrated after visual experience (Figure 2.4G). When we looked at the PLVs in relation to SFs and TFs, V1-LM PLVs did not show significant change in response to the entrained SF and TF, but showed significant increases in responses to other SFs and TFs (Figure 2.4D). On the contrary, V1-AL PLVs had a significant increase in response to the entrained SF and TF, as well as to other stimuli that had similar SFs or TFs to the entrained SF and TF that matched AL's functional preference (Figure 2.4H). These results demonstrated that the HVA that had functional preference matched the entrained SF and TF became more phase-locked to V1 in the 4-8 Hz range following the visual experience, while the other HVA did not, and this phase-locking increase was expressed specifically when the familiar stimulus was presented.

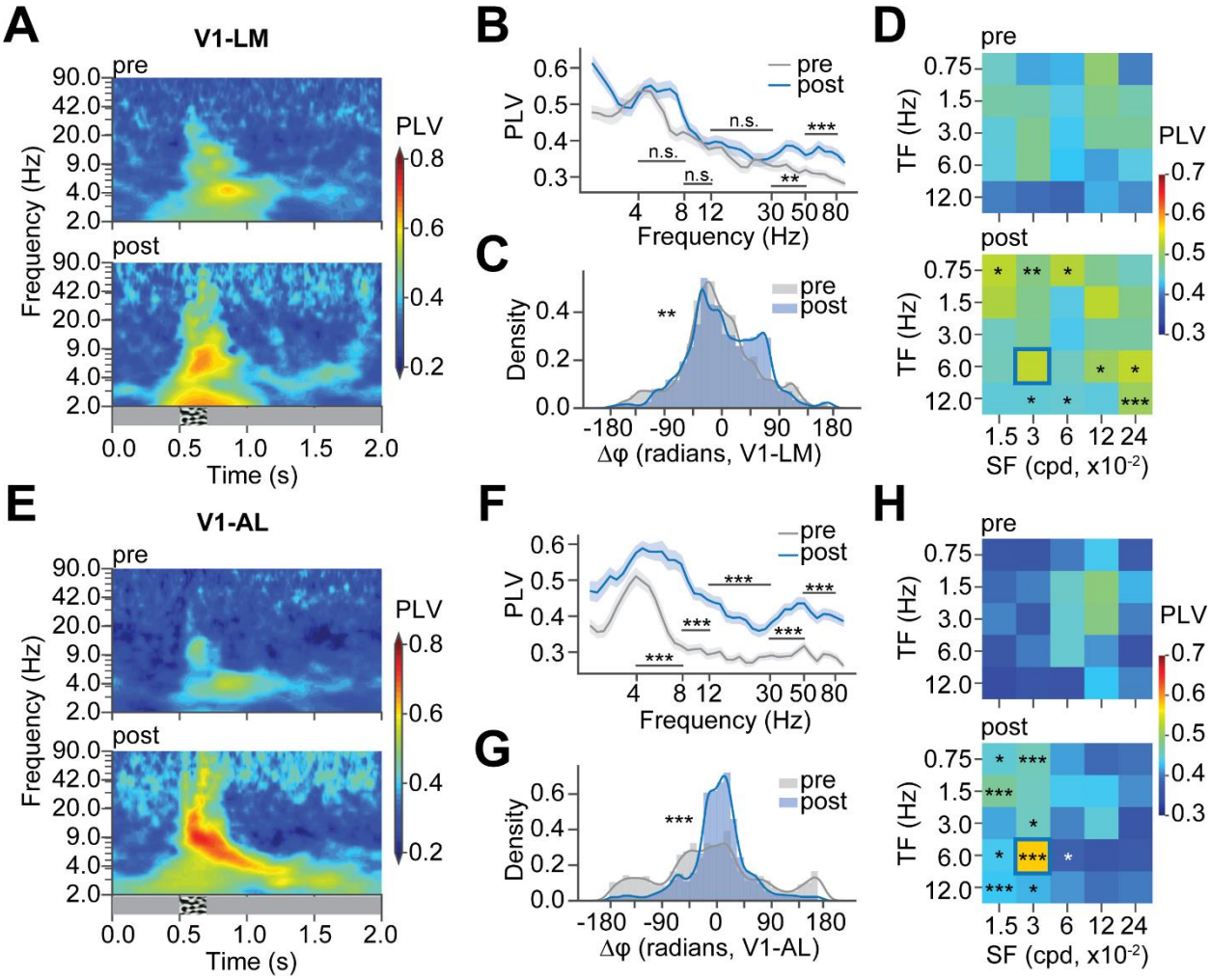

Figure 2.4. AL, but not LM, became more phase locked to V1 in 4-8 Hz after entrainment of SF and TF that matched AL's functional preference. (A) Phase-locking values (PLV) of V1 and LM LFP pairs over time across frequencies were averaged and plotted in heatmaps. N_{pre}=90 LFP pairs, 10 mice; N_{post}=63 LFP pairs, 7 mice. (B) PLV values (median within 700 ms post stimulus onset) of V1-LM LFP pairs across frequencies. Data were represented as mean ± 68% CI. 4-8 Hz: CLES=0.523, p=0.796, 8-12 Hz: CLES=0.502, p=0.972, 12-30 Hz: CLES=0.597, p=0.069, 30-50 Hz: CLES=0.657, p=2.50x10^{-3}, 50-80 Hz: CLES=0.790, p=5.55x10^{-9}, Mann-Whitney U test with FDR-BH correction. (C) 4-8 Hz oscillation phase differences between V1 and LM (within 700 ms post stimulus onset) were plotted in density plots. D=0.378, p=4.68x10^{-3}, Kuiper test. (D) Median 4-8 Hz PLV values of V1-LM LFP pairs in responses to 5 SFs and 5 TFs were plotted in heatmaps. Statistically significant differences between post- and pre- experience for each visual stimulus were labeled. See extended table 4-1 for detailed statistics. (E) PLVs of V1-AL LFP pairs over time across frequencies were averaged and plotted in heatmaps. N_{pre}=81 LFP pairs, 9 mice; N_{post}=54 LFP pairs, 6 mice. (F) PLV values (median within 700 ms post stimulus onset) of V1-AL LFP pairs across frequencies. 4-8 Hz: CLES=0.774, p=2.49x10^{-9}, 8-12 Hz: CLES=0.844, p=3.57x10^{-13}, 12-30 Hz: CLES=0.806, p=3.63x10^{-11}, 30-50 Hz: CLES=0.806, p=3.63x10^{-11}, 50-80 Hz: CLES=0.820, p=8.84x10^{-12}, Mann-Whitney U test with FDR-BH correction. (G) 4-8 Hz oscillation phase differences between V1 and AL (within 700 ms post stimulus onset) were plotted in density plots. D=0.454, p=2.33x10^{-4}, Kuiper test. (H) Median 4-8 Hz PLV values of V1-AL LFP pairs in responses to 5 SFs and 5 TFs were plotted in heatmaps. Statistically significant differences between post- and pre- experience for each stimulus were labeled. See extended table 4-2 for detailed statistics. *-p<0.05, **-p<0.01, ***-p<0.001, n.s.-p>0.05.

2.4.3 Units exhibited spiking clustering and became more phase-locked to local 4-8 Hz LFPs after visual experience

Next, we looked at how single unit firing was modulated by the oscillations. We first compared population firing patterns between pre- and post- experience, by plotting the z-score normalized firing rates of all units in response to the entrained SF and TF that matched with LM's functional preference in heatmaps (**Figure 2.5**A). After the entrainment of SF and TF that matched LM's functional preference, V1 units spiked in clusters that were visually locked or post-stimulus responsive, despite that the spiking clustering in LM or AL units were less obvious. To investigate the unit spiking clustering in relation to the 4-8 Hz oscillations, we looked at spike phase distributions in relation to local 4-8 Hz LFPs. We first separated units into early- (visually-locked), middle- and late- (post-stimulus responsive) firing units based on their peak firing time windows (0.5-0.7s, 0.7-0.9s, and 0.9-1.2s), considering the heterogenous response types of the unit population (**Figure 2.5**B). After entrainment of SF and TF that matched LM's functional preference, spike 4-8 Hz phases of early- (E.), middle- (M.), and late- (L.) firing units in V1 all showed more concentrated distributions centered around 180 degrees, which were LFP troughs. The changes in concentrations of LM and AL spike 4-8 Hz phase distributions were less obvious compared to V1's. To quantify the 4-8 Hz modulated unit spiking, we first defined phase-selective units as the units with non-uniform spike 4-8 Hz phase distributions (Rayleigh test $p<0.05$), and then we measured the phase locking for each phase-selective unit using a biased-free measure called pairwise phase consistency (PPC), where a higher PPC value suggested stronger phase locking. The percentages of phase-selective units out of the early- and out of late- firing units in V1 significantly increased, but the percentages of phase-selective units in LM and AL did not show significant changes in any of early-, middle-, and late- firing unit groups (**Figure 2.5**C). The visually-locked (E.) and post-stimulus (M. and L.) phase-selective units showed significantly increased PPCs after the entrainment of SF and TF that matched LM's functional preference, in V1, LM, and AL (**Figure 2.5**D), suggesting that the unit spiking clustering was more modulated by the 4-8 Hz oscillations. Given the region non-specific PPC increases, we next measured whether there was any significant shift in spike 4-8 Hz phases after visual experience. The mean spike phase of each phase-selective unit was first determined using the circular mean of the phases, and then their mean spike phases were plotted in boxplots (**Figure 2.5**E). The spike phases of V1 and

LM units did not show significantly shifted distribution (**Figure 2.5**E left and middle), but the spike phases of the visually-locked (E.) units in AL became more concentrated and shifted to be following the local 4-8 Hz LFP troughs (180 degree) (**Figure 2.5**E right). The post-stimulus middle-firing (M.) units in AL also showed the trend to spike following the troughs (180 degree) (**Figure 2.5**E right). We also inspected whether the unit phase-locking was specific to the entrained SF and TF, by plotting median PPCs of phase-selective units in relation to SFs and TFs in heatmaps (**Figure 2.5**F). PPCs of the phase-selective units increased significantly in response to the entrained SF and TF, as well as to other SFs and TFs to a less extent (**Figure 2.5**F). Similarly to the entrainment of SF and TF that matched LM's functional preference, when we looked at spike 4-8 Hz phases after entrainment of SF and TF that matched AL's functional preference this time, units also spiked in clusters that were visually-locked or post-stimulus responsive (**Figure 2.6**A), and spike 4-8 Hz phases showed more concentrated distributions centered around 180 degrees, most prominently in V1 (**Figure 2.6**B). The percentages of phase-selective units out of the visually-locked (E.) units in V1 was significantly increased (**Figure 2.6**C top), but the percentages of phase-selective units out of the post-stimulus unit groups did not change significantly, in V1, LM, or AL (**Figure 2.6**C middle and bottom). When we measured phase-locking of the phase-selective units using PPCs, both visually-locked (E.) and post-stimulus (M. and L.) units in V1 showed significantly increased PPCs (**Figure 2.6**D left). The visually locked (E.) units in LM did not show significantly changed PPCs, but the post-stimulus middle-firing (M.) units in LM showed significantly increased PPCs after visual experience (**Figure 2.6**D middle). The visually locked (E.) units in AL, as well as post-stimulus middle-firing (M.) units in AL, showed significantly increased PPCs (**Figure 2.6**D right). We also investigated whether there was any shift in spike phases of the phase-selective units (**Figure 2.6**E), and found that the distributions of the phases of V1 units or AL units did not showed significant changes (**Figure 2.6**E left and right), while the visually-locked (E.) and post-stimulus middle-firing (M.) units in LM showed more concentrated distribution of spike 4-8 Hz phases, and the phases were right-shifted to be following the local 4-8 Hz LFP troughs (180 degree) (**Figure 2.6**E middle), corresponding to the phenomenon seen after the entrainment of SF and TF that matched LM's functional preference. We also examined whether the unit phase-locking change was specific to the entrained SF and TF, and we plotted the median PPCs of phase-selective units in responses to SFs and TFs in heatmaps. Similarly to the entrainment of SF and TF that matched with LM's functional preference, the PPC increase was

not restricted to the entrained SF and TF, but also generalized to other SFs and TFs, especially in V1 (**Figure 2.6**F).

Figure 2.5. Visually locked and post-stimulus responsive units in V1, LM, and AL spiked at more consistent 4-8 Hz local phases after entrainment of SF and TF that matched with LM's functional preference. (A) Units' firing rate z-scores over time were plotted in heatmaps. V1: N_{pre}: 1171 units, 18 mice, N_{post}: 1617 units, 19 mice; LM: N_{pre}: 965 units, 14 mice, N_{post}: 1173 units, 13 mice; AL: N_{pre}: 783 mice, 12 mice, N_{post}: 480 units, 6 mice. (B) Units were grouped into early-, middle-, and late- firing units based on their peak firing rate z-score time windows. 4-8 Hz phases of all spikes in relation to local LFPs were plotted in density plots. (C) Percentages of 4-8 Hz phase selective units from each mouse were plotted in boxplots. V1: N_{pre}: 18 mice, N_{post}: 19 mice; LM: N_{pre}: 14 mice, N_{post}: 13 mice; AL: N_{pre}: 12 mice, N_{post}: 6 mice. V1: early: CLES=0.776, p=0.013, middle: CLES=0.678, p=0.074, late: CLES=0.737, p=0.021; LM: early: CLES=0.426, p=0.610, middle: CLES=0.607, p=0.610, late: CLES=0.439, p=0.610; AL: early: CLES=0.694, p=0.617, middle: CLES=0.438, p=0.963, late: CLES=0.5, p=0.963, Mann-Whitney U test with FDR-BH correction. (D) Pairwise phase consistency values (PPC, calculated using spike phases within 700 ms post stimulus onset) of 4-8 Hz phase selective units were plotted in bar plots. V1: Pre: N_{early}: 497 units, N_{middle}: 199 units, N_{late}: 81 units, 18 mice, Post: N_{early}: 766 units, N_{middle}: 320 units, N_{late}: 147 units, 19 mice; LM: Pre: N_{early}: 158 units, N_{middle}: 129 units, N_{late}: 65 units, 14 mice, Post: N_{early}: 117 units, N_{middle}: 194 units, N_{late}: 68 units, 13 mice; AL: Pre: N_{early}: 96 units, N_{middle}: 141 units, N_{late}: 87 units, 12 mice, Post: N_{early}: 83 units, N_{middle}: 92 units, N_{late}: 62 units, 6 mice. Data are represented as median ± SEM. V1: early: CLES=0.686, $p=1.02\times10^{-28}$, middle: CLES=0.743, $p=2.10\times10^{-20}$, late: CLES=0.803, $p=4.14\times10^{-14}$; LM: early: CLES=0.609, $p=2.51\times10^{-3}$, middle: CLES=0.635, $p=1.2\times10^{-4}$, late: CLES=0.652, $p=2.51\times10^{-3}$; AL: early: CLES=0.704, $p=3.71\times10^{-6}$, middle: CLES=0.685, $p=3.71\times10^{-6}$, late: CLES=0.618, p=0.015, Mann-Whitney U test with FDR-BH correction. (E) Phase preferences of phase-selective units were plotted in boxplots. V1: early: D=0.076, p=0.201, middle: D=0.136, p=0.086, late: D=0.149, p=0.247; LM: early: D=0.105, p=0.595, middle: D=0.083, p=0.595, late: D=0.113, p=0.595; AL: early: D=0.194, p=0.049, middle: D=0.171, p=0.053, late: CLES=0.111, p=0.775. Kuiper test with FDR-BH correction. (F) Median PPCs of phase-selective units in relation to 5 SFs and 5 TFs were plotted in heatmaps. Statistically significant differences between post- and pre- experience for each visual stimulus were labeled. See extended table 5-1 for detailed statistics. *-p<0.05, **-p<0.01, ***-p<0.001, n.s.-p>0.05.

Figure 2.5 continued

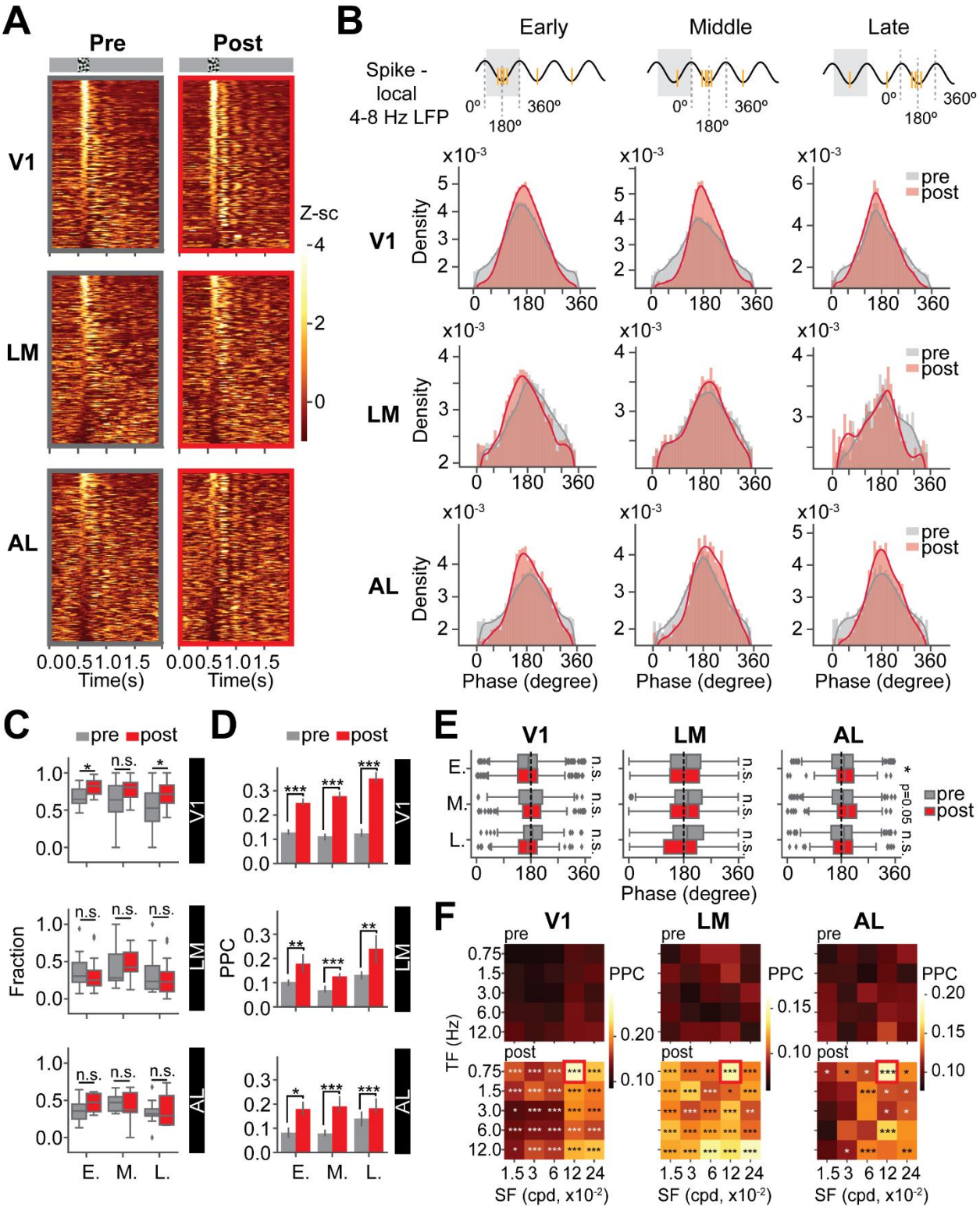

Figure 2.6. Visually locked and post-stimulus units in V1, LM, and AL spiked at more consistent 4-8 Hz local phases after entrainment of SF and TF that matched with AL's functional preference. (A) Units' firing rate z-scores over time were plotted in heatmaps. V1: N_{pre}: 921 units, 15 mice, N_{post}: 916 units, 14 mice; LM: N_{pre}: 666 units, 9 mice, N_{post}: 778 units, 11 mice; AL: N_{pre}: 711 mice, 11 mice, N_{post}: 657 units, 9 mice. (B) Units were grouped into early-, middle-, and late- firing units based on their peak firing rate z-score time windows. 4-8 Hz phases of all spikes in relation to local LFPs were plotted in density plots. (C) Percentages of 4-8 Hz phase selective units from each mouse were plotted in boxplots. V1: N_{pre}: 18 mice, N_{post}: 14 mice; LM: N_{pre}: 14 mice, N_{post}: 9 mice; AL: N_{pre}: 12 mice, N_{post}: 9 mice. V1: early: CLES=0.778, p=0.025, middle: CLES=0.513, p=0.920, late: CLES=0.598, p=0.549; LM: early: CLES=0.675, p=0.263, middle: CLES=0.631, p=0.313, late: CLES=0.793, p=0.089; AL: early: CLES=0.462, p=0.803, middle: CLES=0.620, p=0.682, late: CLES=0.602, p=0.682, Mann-Whitney U test with FDR-BH correction. (D) Pairwise phase consistency values (PPC, calculated using spike phases within 700 ms post stimulus onset) of 4-8 Hz phase-selective units were plotted in bar plots. V1: Pre: N_{early}: 391 units, N_{middle}: 258 units, N_{late}: 127 units, 18 mice, Post: N_{early}: 439 units, N_{middle}: 141 units, N_{late}: 75 units, 14 mice; LM: Pre: N_{early}: 92 units, N_{middle}: 140 units, N_{late}: 39 units, 14 mice, Post: N_{early}: 117 units, N_{middle}: 96 units, N_{late}: 49 units, 9 mice; AL: Pre: N_{early}: 134 units, N_{middle}: 120 units, N_{late}: 69 units, 12 mice, Post: N_{early}: 102 units, N_{middle}: 105 units, N_{late}: 62 units, 9 mice. Data are represented as median ± SEM. V1: early: CLES=0.674, p=1.5x10-17, middle: CLES=0.705, $p=1.79x10^{-11}$, late: CLES=0.701, $p=1.77x10^{-6}$; LM: early: CLES=0.581, p=0.067, middle: CLES=0.632, $p=1.68x10^{-3}$, late: CLES=0.508, p=0.899; AL: early: CLES=0.701, $p=3.87x10^{-7}$, middle: CLES=0.658, $p=6.29x10^{-5}$, late: CLES=0.510, p=0.848, Mann-Whitney U test with FDR-BH correction. (E) Phase preferences of phase-selective units were plotted in boxplots. V1: early: D=0.061, p=0.722, middle: D=0.108, p=0.714, late: D=0.207, p=0.091; LM: early: D=0.192, $p=1.31x10^{-3}$, middle: D=0.245, $p=4.90x10^{-6}$, late: D=0.196, p=0.054; AL: early: D=0.116, p=0.669, middle: D=0.110, p=0.669, late: CLES=0.109, p=0.689. Kuiper tests with FDR-BH correction. (F) Median PPCs of phase-selective units in relation to 5 SFs and 5 TFs were plotted in heatmaps. Statistically significant differences between post- and pre- experience for each visual stimulus were labeled. See extended table 6-1 for detailed statistics. *-p<0.05, **-p<0.01, ***-p<0.001, n.s.-p>0.05.

Figure 2.6 continued

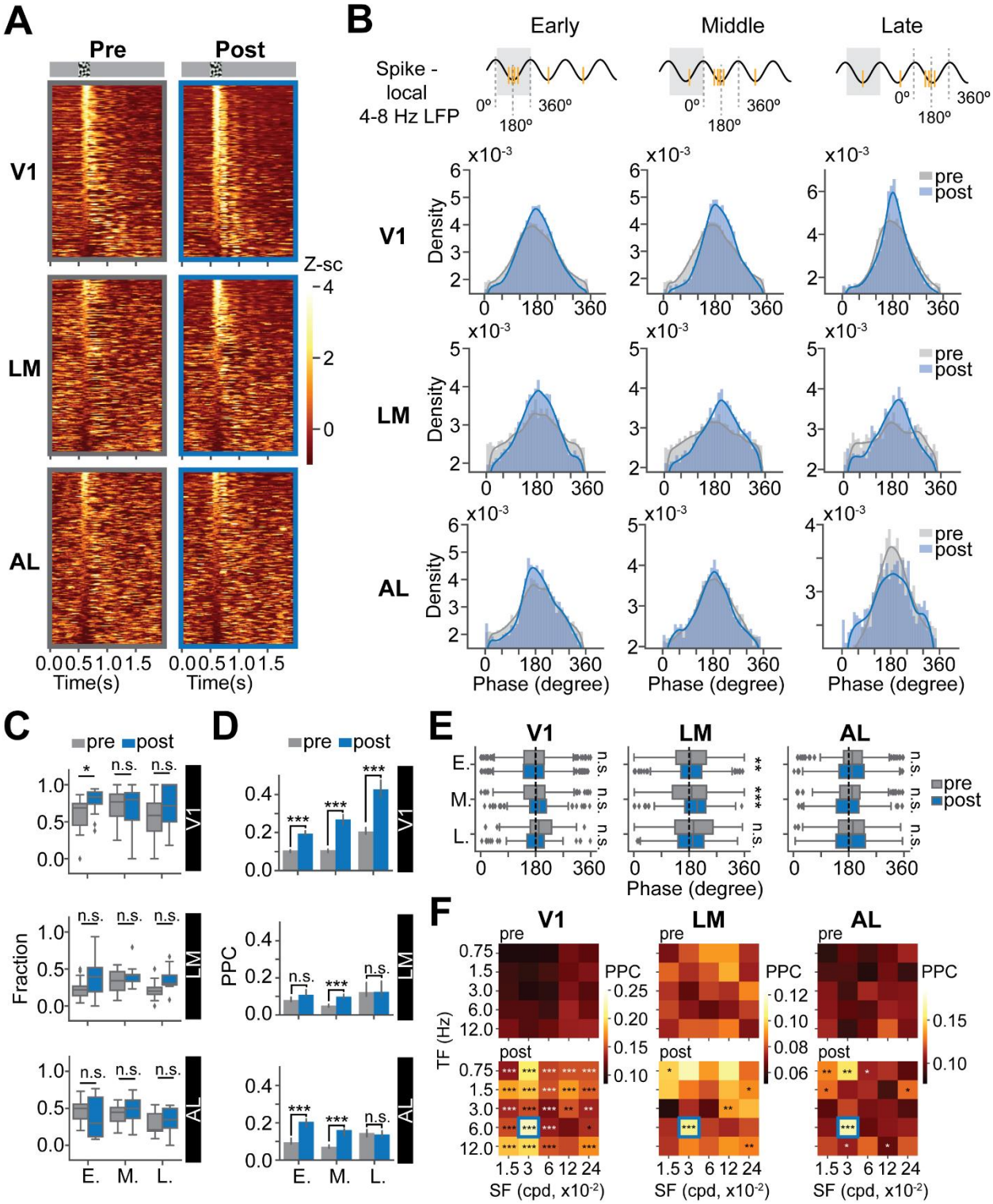

2.4.4 Units in V1 and HVAs became more phase-locked inter-areally in 4-8 Hz

To inspect whether there was inter-areal 4-8 Hz temporal binding between V1 and HVAs, we analyzed inter-areal spike phase locking as well. We first looked at the distribution of spike 4-8 Hz phases of inter-areal phase-selective units in LM or AL, in relation to V1 superficial layer LFPs (**Figure 2.7**A). After entrainment of SF and TF that matched with LM's functional preference, the percentages of inter-areal phase-selective units out of visually locked (early-firing) units or post-stimulus (middle- and late- firing) units did not change significantly, in either LM or AL (**Figure 2.7**B). When we quantified the phase-locking using PPCs, the visually-locked (early-firing) units and post-stimulus middle- firing units in LM showed significantly increased PPCs (**Figure 2.7**C left), and the visually-locked (early-firing) units and post-stimulus (middle- and late-firing) units in AL showed significantly increased PPCs as well (**Figure 2.7**C right). When we looked at the distributions of inter-areal 4-8 Hz spike phases after entrainment of SF and TF that matched LM's functional preference, there were more visually-locked (early-firing) units in LM spiking closer to the troughs of V1 LFPs (180 degrees) (**Figure 2.7**D left, F left), and there were also more post-stimulus late-firing units in LM spiking closer to the troughs of V1 LFPs (**Figure 2.7**D right, F right). For the distributions of AL units' 4-8 Hz phases in relation to V1 LFPs, there were more visually-locked (early-firing) units spiking closer to the troughs of V1 LFPs (180 degrees) after entrainment of SF and TF that matched with LM's functional preference (**Figure 2.7**E left, G left), while there were more post-stimulus middle-firing units' spiking following the troughs of V1 LFPs (180 degrees) (**Figure 2.7**E middle, G middle).

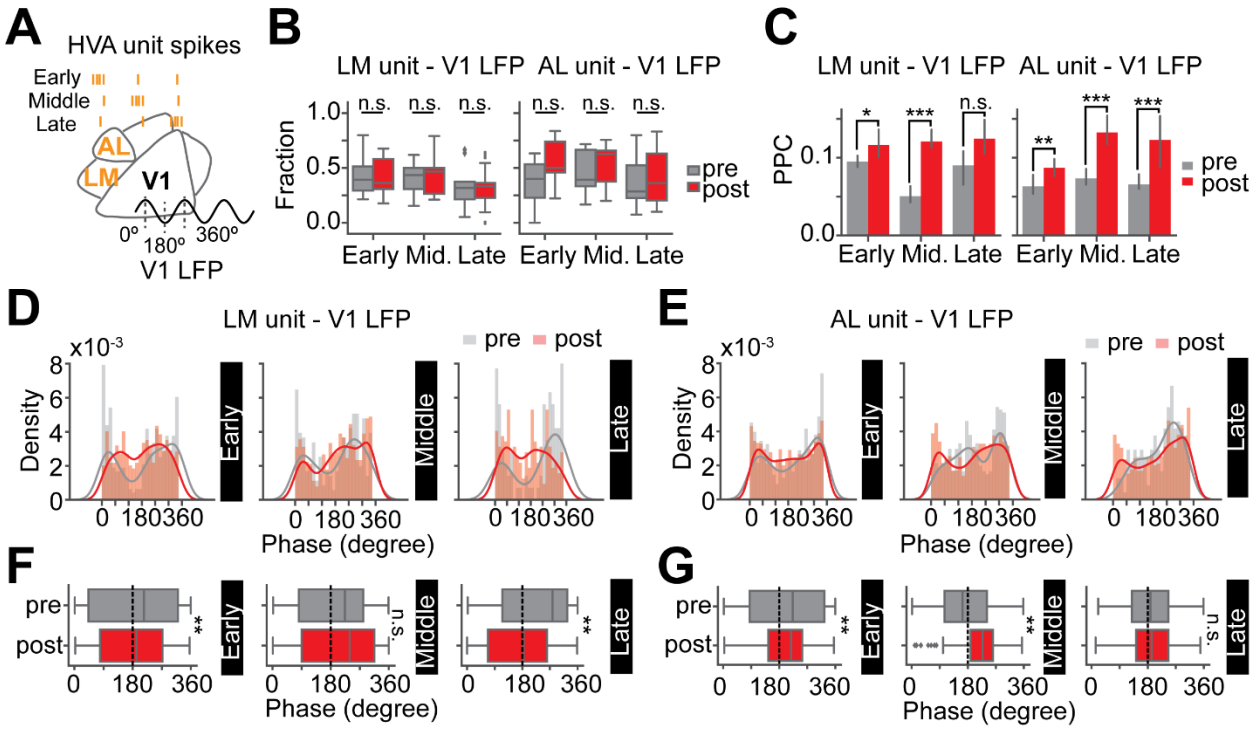

Figure 2.7. Visually locked and post-stimulus units in LM and AL became more phase locked to V1 superficial layer LFPs in 4-8 Hz after entrainment of SF and TF that matched LM's functional preference. (A) The spike 4-8 Hz phases of units in LM or AL in relation to V1 superficial layer LFPs were analyzed. (B) Percentages of inter-areal phase-selective units in LM or AL from each mouse were plotted in boxplots. LM: N_{pre}: 9 mice, N_{post}: 13 mice; AL: N_{pre}: 9 mice, N_{post}: 6 mice. LM: early: CLES=0.487, p=1, middle: CLES=0.547, p=1, late: CLES=0.504, p=1; AL: early: CLES=0.667, p=0.906, middle: CLES=0.528, p=0.906, late: CLES=0.574, p=0.906, Mann-Whitney U test with FDR-BH correction. (C) PPCs of inter-areal phase selective units were plotted in bar plots. LM units – V1 LFPs: Pre: N_{early}: 120 units, N_{middle}: 84 units, N_{late}: 37 units, 9 mice, Post: N_{early}: 136 units, N_{middle}: 213 units, N_{late}: 74 units, 13 mice; AL units – V1 LFPs: Pre: N_{early}: 84 units, N_{middle}: 111 units, N_{late}: 51 units, 9 mice, Post: N_{early}: 100 units, N_{middle}: 97 units, N_{late}: 57 units, 6 mice. Data are represented as median ± 68% CI. LM: early: CLES=0.559, p=0.016, middle: CLES=0.681, $p=4.09\times10^{-12}$, late: CLES=0.577, p=0.056; AL: early: CLES=0.572, $p=2.28\times10^{-3}$, middle: CLES=0.673, $p=1.49\times10^{-14}$, late: CLES=0.640, $p=2.86\times10^{-5}$, Mann-Whitney U test with FDR-BH correction. (D) Spike 4-8 Hz phases of inter-areal phase-selective units in LM in relation to V1 superficial layer LFPs were plotted in density plots. (E) Spike 4-8 Hz phases of inter-areal phase-selective units in AL in relation to V1 superficial layer LFPs were plotted in density plots. (F) Spike 4-8 Hz phases of inter-areal phase-selective units in LM in relation to V1 superficial layer LFPs were plotted in boxplots. Early: D=0.279, p= 0.001, middle: D=0.181, p=0.226, late: D=0.394, p=0.009. Kuiper tests with FDR-BH correction. (G) Spike 4-8 Hz phases of inter-areal phase-selective units in AL in relation to V1 superficial layer LFPs were plotted in boxplots. Early: D=0.440, $p=6.23\times10^{-7}$, middle: D=0.438, $p=7.85\times10^{-8}$, late: D=0.175, p=0.861. Kuiper tests with FDR-BH correction. *-p<0.05, **-p<0.01, ***-p<0.001, n.s.-p>0.05.

Then we looked at V1 units' inter-areal spike 4-8 Hz phases in relation to LM or AL superficial layer LFPs after entrainment of SF and TF that matched LM's functional preference (**Figure 2.8**A). The percentages of inter-areal phase-selective units out of the visually-locked (early-firing) units in either LM or AL did not change significantly after entrainment of SF and TF that matched LM's functional preference (**Figure 2.8**B left). The percentages of inter-areal phase-selective units out of the post-stimulus middle-firing units were also not changed significantly in either LM or AL (**Figure 2.8**B middle), while the percentage of inter-areal phase-selective units out of the post-stimulus late-firing units in AL, but not in LM significantly increased (**Figure 2.8**C right). When we quantified the inter-areal phase-locking of the phase-selective units using PPCs, visually-locked (early-firing) and post-stimulus (middle- and late- firing) units in V1 showed significantly higher PPCs in relation to both LM LFPs and AL LFPs (**Figure 2.8**C). When we looked at the distributions of the spike 4-8 Hz phases of V1 units in relation to LM LFPs or AL LFPs, there were more units in V1 that preferred to spike following the LM LFP troughs after entrainment of SF and TF that matched LM's functional preference, for both visually-locked (early-firing) and post-stimulus (middle- and late- firing) units (**Figure 2.8**D, F). The spike phases of V1 visually-locked (early-firing) and post-stimulus (middle- and late- firing) units in relation to AL LFPs were more widely spread after the entrainment, with more visually-locked (early-firing) and post-stimulus (middle-firing) units spiking before the troughs of AL LFPs (**Figure 2.8**E, G).

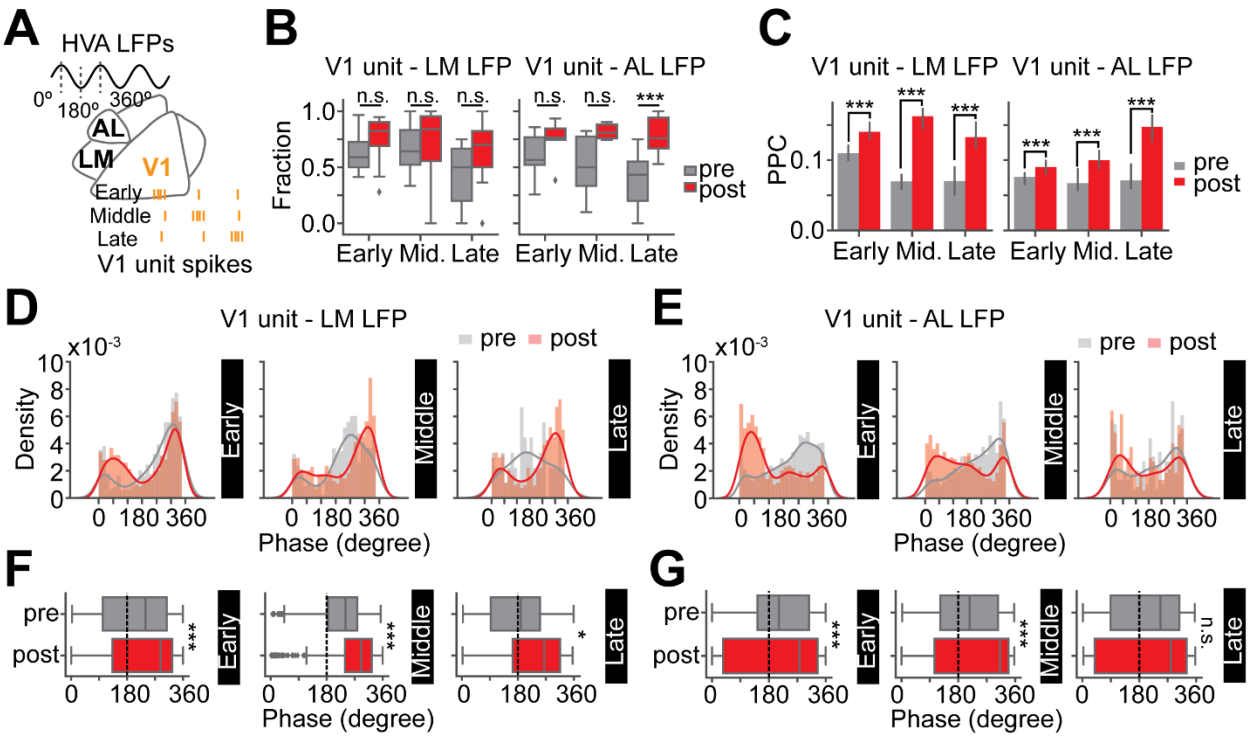

Figure 2.8. Visually locked and post-stimulus units in V1 became more phase-locked to LM and AL superficial layer LFPs in 4-8 Hz, but with different phase preferences, after entrainment of SF and TF that matched LM's functional preference. (A) The spike 4-8 Hz phases of units in V1 in relation to superficial layer LFPs in LM or AL were analyzed. (B) Percentages of inter-areal phase-selective units in V1 from each mouse were plotted in boxplots. LM: N_{pre}: 9 mice, N_{post}: 13 mice; AL: N_{pre}: 9 mice, N_{post}: 6 mice. LM: early: CLES=0.688, p=0.226, middle: CLES=0.606, p=0.447, late: CLES=0.709, p=0.226; AL: early: CLES=0.722, p=0.175, middle: CLES=0.806, p=0.089, late: CLES=0.917, p=0.028, Mann-Whitney U test with FDR-BH correction. (C) PPCs of inter-areal phase selective units were plotted in bar plots. V1 units – LM LFPs: Pre: N_{early}: 176 units, N_{middle}: 108 units, N_{late}: 21 units, 9 mice, Post: N_{early}: 504 units, N_{middle}: 186 units, N_{late}: 89 units, 13 mice; V1 units – AL LFPs: Pre: N_{early}: 266 units, N_{middle}: 74 units, N_{late}: 50 units, 9 mice, Post: N_{early}: 235 units, N_{middle}: 130 units, N_{late}: 50 units, 6 mice. Data are represented as median ± 68% CI. LM: early: CLES=0.585, p=6.27×10^{-8}, middle: CLES=0.707, p=5.64×10^{-20}, late: CLES=0.688, p=3.66×10^{-5}; AL: early: CLES=0.550, p=4.49×10^{-4}, middle: CLES=0.590, p=4.49×10^{-4}, late: CLES=0.663, p=2.95×10^{-5}, Mann-Whitney U test with FDR-BH correction. (D) Spike 4-8 Hz phases of inter-areal phase-selective units in V1 in relation to LM superficial layer LFPs were plotted in density plots. (E) Spike 4-8 Hz phases of inter-areal phase-selective units in V1 in relation to AL superficial layer LFPs were plotted in density plots. (F) Spike 4-8 Hz phases of inter-areal phase-selective units in V1 in relation to LM superficial layer LFPs in 4-8 Hz were plotted in boxplots. Early: D=0.189, p=3.06×10^{-5}, middle: D=0.378, p=4.45×10^{-11}, late: D=0.335, p=0.017. Kuiper tests with FDR-BH correction. (G) Inter-areal spike phase preferences of phase-selective units in V1 in relation to AL superficial layer LFPs in 4-8 Hz were plotted in boxplots. Early: D=0.407, p= 4.99×10^{-24}, middle: D=0.385, p=2.53×10^{-9}, late: D=0.251, p=0.055. Kuiper tests with FDR-BH correction. *-p<0.05, **-p<0.01, ***-p<0.001, n.s.-p>0.05.

To examine whether inter-areal 4-8 Hz temporal relationship would also establish when other SFs and TFs were used in the visual experience, we examined inter-areal spike phase-locking and spike phase distributions after entrainment of SF and TF that matched AL's functional preference (**Figure 2.9**A). The percentages of inter-areal phase-selective units in LM or AL did not change significantly after the entrainment, for either visually-locked (early-firing) units or post-stimulus (middle-firing and late-firing) units (**Figure 2.9**B). Then, when we quantified the inter-areal phase-locking using PPCs, the visually locked (early-firing) units in both LM and AL showed significantly increased PPCs (**Figure 2.9**C). The post-stimulus middle-firing units in LM, but not in AL, showed significantly increased PPCs, and the post-stimulus late-firing units did not show significant changes in PPCs in either LM or AL (**Figure 2.9**C). When we examined the distributions of units' spike 4-8 Hz inter-areal phases in relation to V1 LFPs, neither visually-locked units (early-firing) nor post-stimulus (middle- and late- firing) units in LM showed significantly changed phase distributions after the entrainment (**Figure 2.9**D, F). As for the units in AL, there were more visually-locked (early-firing) units in AL spiking before the troughs of V1 LFPs (**Figure 2.9**E, G), while the post-stimulus units in AL did not show significantly changed inter-areal spike phase distributions.

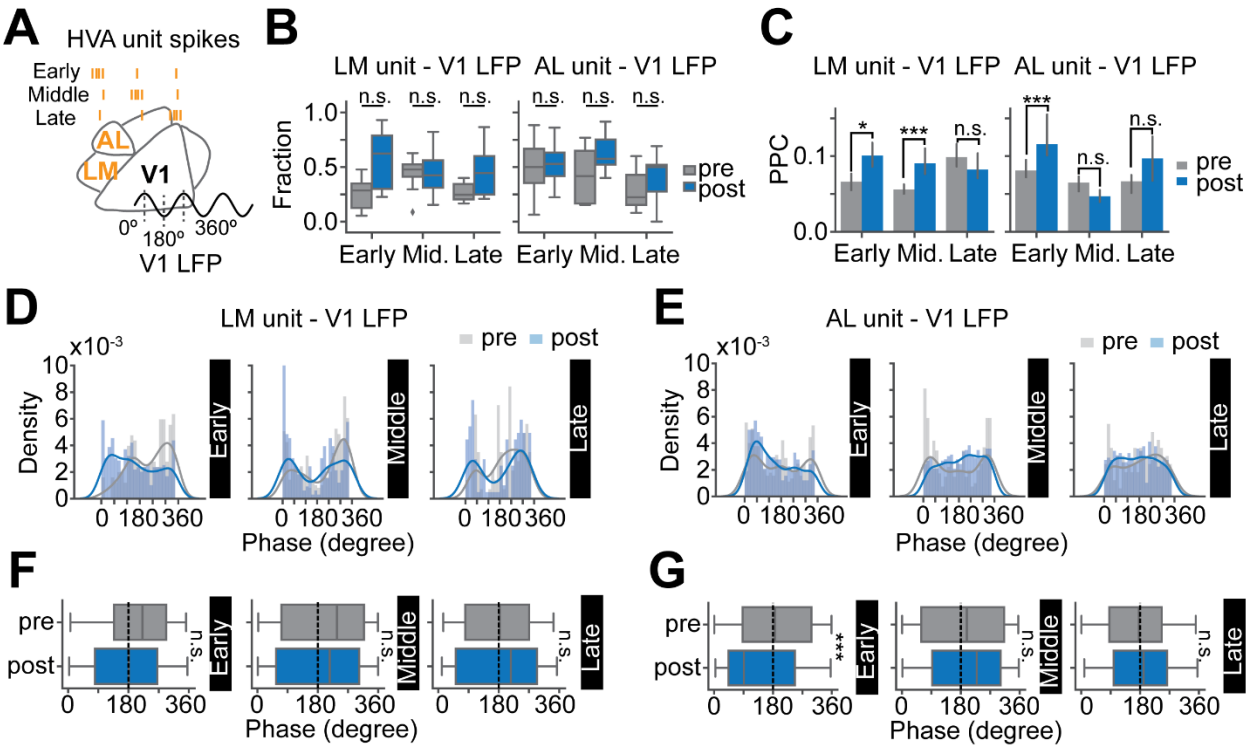

Figure 2.9. Visually locked and post-stimulus units in LM and AL became more phase locked to V1 superficial layer LFPs in 4-8 Hz after entrainment of SF and TF that matched AL's functional preference. (A) The spike 4-8 Hz phases of units in LM or AL in relation to superficial layer LFPs in V1 were analyzed. (B) Percentages of inter-areal phase-selective units in LM or AL from each mouse were plotted in boxplots. LM: N_{pre}: 9 mice, N_{post}: 7 mice; AL: N_{pre}: 9 mice, N_{post}: 7 mice. LM: early: CLES=0.762, p=0.262, middle: CLES=0.460, p=0.832, late: CLES=0.729, p=0.262; AL: early: CLES=0.571, p=0.671, middle: CLES=0.698, p=0.435, late: CLES=0.667, p=0.435. Mann-Whitney U test with FDR-BH correction. (C) PPCs of inter-areal phase selective units were plotted in bar plots. LM units – V1 LFPs: Pre: N_{early}: 60 units, N_{middle}: 124 units, N_{late}: 32 units, 9 mice, Post: N_{early}: 137 units, N_{middle}: 82 units, N_{late}: 46 units, 7 mice; AL units – V1 LFPs: Pre: N_{early}: 109 units, N_{middle}: 98 units, N_{late}: 39 units, 9 mice, Post: N_{early}: 96 units, N_{middle}: 104 units, N_{late}: 59 units, 7 mice. Data were represented as median ± 68% CI. LM: early: CLES=0.571, p=0.035; AL: early: CLES=0.602, $p=2.3\times10^{-4}$. LM: middle: CLES=0.626, $p=8.93\times10^{-6}$; AL: middle: CLES=0.446, p=0.054. LM: late: CLES=0.509, p=0.847; AL: late: CLES=0.520, p=0.606, Mann-Whitney U test with FDR-BH correction. (D) Inter-areal spike phase preferences of LM phase-selective units in relation to V1 superficial layer LFPs in 4-8 Hz were plotted in density plots. (E) Inter-areal spike phase preferences of AL phase-selective units in relation to V1 superficial layer LFPs in 4-8 Hz were plotted in density plots. (F) Inter-areal spike phase preferences of phase-selective units in V1 in relation to LM superficial layer LFPs in 4-8 Hz were plotted in boxplots. Early: D=0.208, p=0.267, middle: D=0.228, p=0.083, late: D=0.349, p=0.107. Kuiper tests with FDR-BH correction. (G) Inter-areal spike phase preferences of phase-selective units in V1 in relation to AL superficial layer LFPs in 4-8 Hz were plotted in boxplots. Early: D=0.317, $p=8.35\times10^{-4}$, middle: D=0.216, p=0.117, late: D=0.181, p=0.895. Kuiper tests with FDR-BH correction. *-p<0.05, **-p<0.01, ***-p<0.001, n.s.-p>0.05.

Then we looked at the inter-areal spike phases after entrainment of SF and TF that matched AL's functional preference (**Figure 2.10**A). For the visually-locked (early-firing) units, the percentage of AL phase-selective units in V1 significantly increased, but the percentage of LM phase-selective units in V1 did not (**Figure 2.10**B left). The percentages of LM phase selective or AL phase selective post-stimulus units in V1 did not change significantly (**Figure 2.10**B right). When we quantified the inter-areal phase-locking using PPCs, the visually-locked (early-firing) units in V1 showed significantly increased PPCs in relation to both LM LFPs and AL LFPs after the entrainment (**Figure 2.10**C). The post-stimulus middle-firing units in V1 showed significantly increased PPCs in relation to LM LFPs, but not to AL LFPs (**Figure 2.10**C). The post-stimulus late-firing units in V1 did not show significant changes in PPCs in relation to LM LFPs but showed significantly decreased PPCs in relation to AL LFPs (**Figure 2.10**C). Then we looked at the distributions of the inter-areal spike phases, the visually-locked (early-firing) and post-stimulus (middle- and late- firing) units in V1 showed more widespread distributions of spike 4-8 Hz phases in relation to LM LFPs, with more units spiking before the troughs of LM LFPs, after entrainment of SF and TF that matched AL's functional preference (**Figure 2.10**D, F). As for V1 units' spike phases in relation to AL LFPs, the visually-locked units in V1 showed more widespread spike 4-8 Hz phases, with more units spiking before the troughs of AL LFPs (**Figure 2.10**E left, G left). The post-stimulus middle-firing units in V1 also showed more widespread spike 4-8 Hz phases in relation to AL LFPs, with more units spiking before the troughs of AL LFPs (**Figure 2.10**E middle, G middle). The post-stimulus late-firing units in V1 spiked at more concentrated 4-8 Hz phases, with more units spiking after the troughs of AL LFPs (**Figure 2.10**E right, G right).

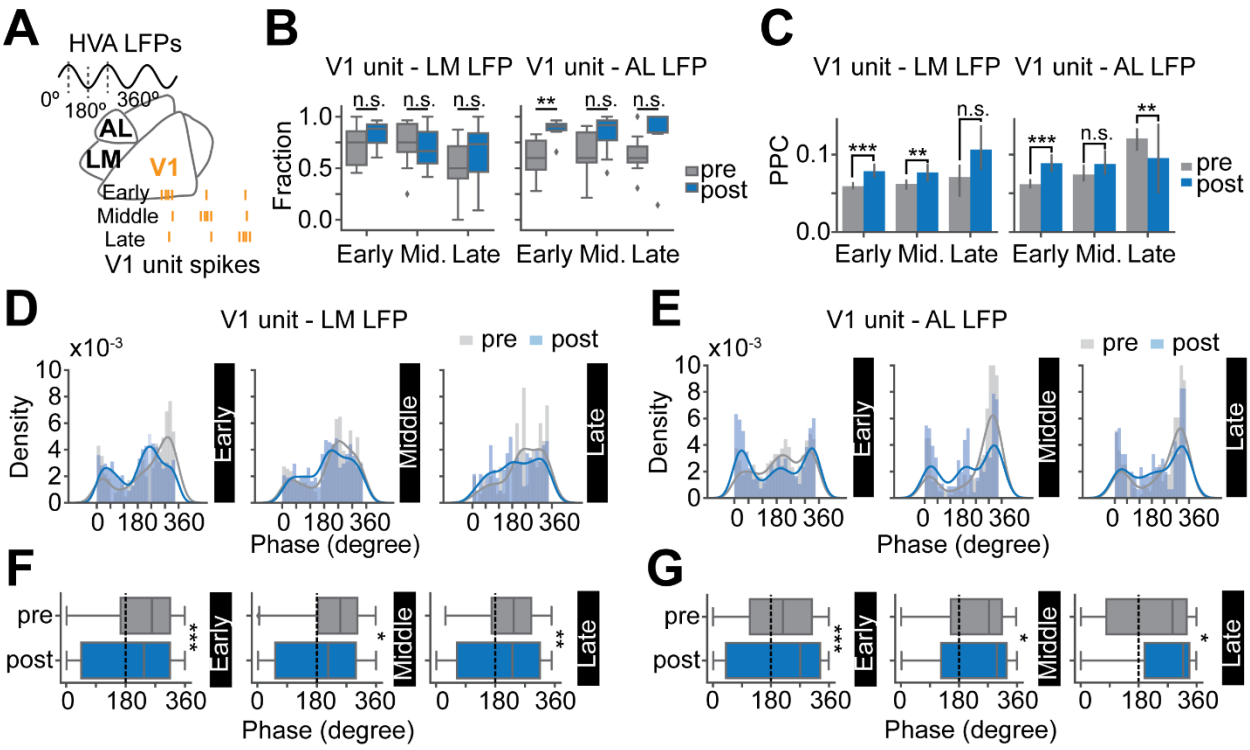

Figure 2.10. Visually locked and post-stimulus units in V1 became more phase-locked to LM and AL superficial layer LFPs in 4-8 Hz, after entrainment of SF and TF that matched AL's functional preference. (A) The spike 4-8 Hz phases of units in LM or AL in relation to superficial layer LFPs in V1 were analyzed. (B) Percentages of inter-areal phase-selective units in V1 from each mouse were plotted in boxplots. LM: N_{pre}: 9 mice, N_{post}: 7 mice; AL: N_{pre}: 9 mice, N_{post}: 7 mice. LM: early: CLES=0.722, p=0.407, middle: CLES=0.437, p=0.711, late: CLES=0.653, p=0.466; AL: early: CLES=0.944, p=$7.27\text{x}10^{-3}$, middle: CLES=0.778, p=0.060, late: CLES=0.794, p=0.060, Mann-Whitney U test with FDR-BH correction. (C) PPCs of inter-areal phase selective units were plotted in bar plots. V1 units – LM LFPs: Pre: N_{early}: 157 units, N_{middle}: 137 units, N_{late}: 35 units, 9 mice, Post: N_{early}: 260 units, N_{middle}: 74 units, N_{late}: 31 units, 7 mice; V1 units – AL LFPs: Pre: N_{early}: 237 units, N_{middle}: 101 units, N_{late}: 96 units, 9 mice, Post: N_{early}: 285 units, N_{middle}: 93 units, N_{late}: 50 units, 7 mice. Data were represented as median ± 68% CI. LM: early: CLES=0.590, p=$2.93\text{x}10^{-7}$; AL: early: CLES=0.589, p=$6.63\text{x}10^{-10}$. LM: middle: CLES=0.570, p=$2.88\text{x}10^{-3}$; AL: middle: CLES=0.534, p=0.116. LM: late: CLES=0.563, p=0.144; AL: late: CLES=0.425, p=$5.55\text{x}10^{-3}$, Mann-Whitney U test with FDR-BH correction. (D) Inter-areal spike phase preferences of LM phase-selective units in relation to V1 superficial layer LFPs in 4-8 Hz were plotted in density plots. (E) Inter-areal spike phase preferences of phase-selective units in V1 in relation to LM superficial layer LFPs in 4-8 Hz were plotted in boxplots. Early: D=0.249, p=$1.43\text{x}10^{-6}$, middle: D=0.235, p=0.015, late: D=0.366, p=$5.11\text{x}10^{-3}$. Kuiper tests with FDR-BH correction. (F) Inter-areal spike phase preferences of phase-selective units in V1 in relation to AL superficial layer LFPs in 4-8 Hz were plotted in boxplots. Early: D=0.354, p= $5.35\text{x}10^{-17}$, middle: D=0.226, p=0.031, late: D=0.261, p=0.040. Kuiper tests with FDR-BH correction. *-p<0.05, **-p<0.01, ***-p<0.001, n.s.-p>0.05.

2.4.5 V1 and HVA units were more likely to spike in synchrony after visual experience

Spike train synchrony with short time delay may infer functional connection strength between units. To infer the functional connectivity between units, jitter-corrected cross-correlations were calculated between all possible unit pairs from simultaneously recorded units (**Figure 2.11**A, details see Methods). A representative jitter-corrected cross-correlation between a unit in V1 and a unit in LM showed peak correlation within ±5 ms from the zero time lag (**Figure 2.11**B, C). To quantify spiking synchrony between each unit pair, the area under the cross-correlation curve within ±5 ms was used as the synchrony index. Then we selected unit pairs whose cross-correlation showed a larger than two standard deviations (of correlations within ±100 ms from the zero time lag) peak within ±5 ms in response to at least one stimulus as highly correlated unit pairs for further analyses. We first looked at the synchrony indices of all highly correlated unit pairs in response to the entrained SF and TF after entrainment of SF and TF that matched LM's functional preference, visually-locked (early-firing) units in V1 had significantly higher spiking synchrony with visually-locked (early-firing) units in LM, as well as with visually-locked (early-firing) units in AL (**Figure 2.11**D). The post-stimulus middle-firing unit pairs between V1 and LM, or between V1 and AL, also had significantly higher spiking synchrony (**Figure 2.11**D). Interestingly, the post-stimulus late-firing unit pairs between V1 and LM had lower spiking synchrony, and those between V1 and AL did not show significant changes (**Figure 2.11**D). However, there was no significant change in the percentages of highly correlated unit pairs between V1 and LM, or between V1 and AL (**Figure 2.11**E). As different functional connections may be recruited in responses to different SFs and TFs, we separated highly correlated unit pairs into 25 groups, at which SF/TF they showed highest synchrony index, and plotted mean synchrony indices of each group in heatmaps. After entrainment of SF and TF that matched LM's functional preference, both visually-locked and post-stimulus unit pairs in the entrained SF/TF group showed a trend for synchrony increase, though not significant. Interestingly, visually-locked unit pairs between V1 and LM in other SF/TF groups showed significantly decreased spiking synchrony (**Figure 2.11**F left), and the post-stimulus (middle- and late- firing) units in other SF/TF showed significantly increased synchrony indices (**Figure 2.11**F right). As for unit pairs between V1 and AL, the unit pairs in the entrained SF/TF group did not show significantly changed spiking synchrony, for either visually-locked or post-stimulus unit pairs (**Figure 2.11**G). However, the visually-locked unit pairs in other SF/TF groups showed significantly increased spiking synchrony

(**Figure 2.11**G left), and the post-stimulus (middle- and late- firing) unit pairs in other SF/TF groups also showed significantly increased spiking synchrony, but in fewer SF/TF groups compared the visually-locked unit pairs (**Figure 2.11**G right).

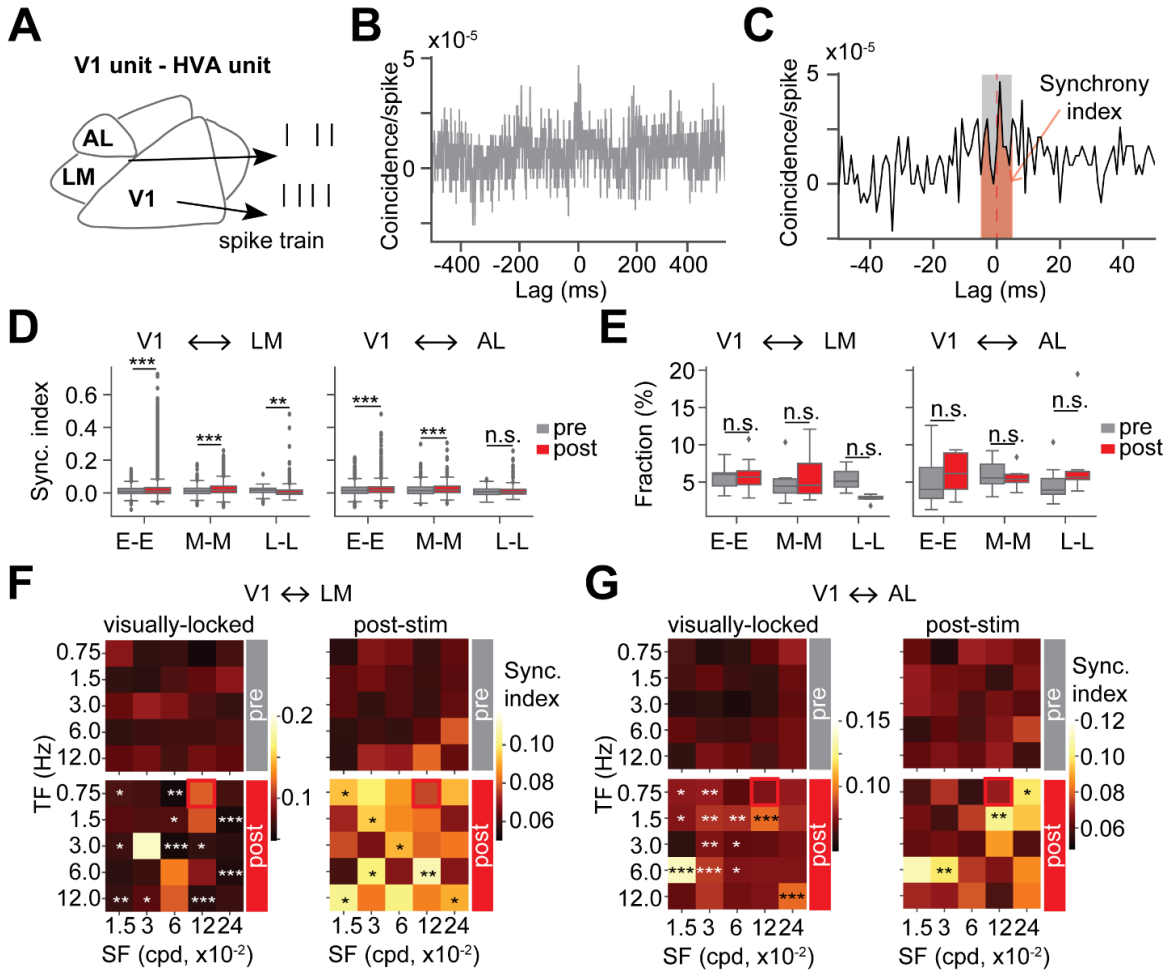

Figure 2.11. Inter-areal spiking synchrony increased after entrainment of SF and TF that matched LM's functional preference, especially for post-stimulus responding units. (A) Jitter corrected spike train cross-correlations were calculated for units that were simultaneously recorded in V1 and LM, or in V1 and AL. (B) A representative spike train cross-correlation (after firing rate correction and jitter correction) of a V1-LM unit pair. (C) The cross-correlation of the unit pair in (B) showed a high correlation peak (>2 std. of ±100 ms from 0 ms) within ±5 ms time lag. The area under the curve within the ±5 ms from 0 ms was quantified as the synchrony index for a unit pair. Unit pairs that showed such peak in response to at least one visual stimulus were selected for further analyses. (D) Synchrony indices of highly correlated unit pairs in response to the entrained SF and TF were plotted in boxplots. Synchrony indices of early-early (E-E), middle-middle (M-M), late-late (L-L) unit pairs were analyzed. V1-LM: Pre: $N_{E\text{-}E}$: 2597 unit pairs, $N_{M\text{-}M}$: 1076 unit pairs, $N_{L\text{-}L}$: 91 unit pairs, 9 mice; Post: $N_{E\text{-}E}$: 5131 unit pairs, $N_{M\text{-}M}$: 2308 unit pairs, $N_{L\text{-}L}$: 309 unit pairs, 13 mice. V1-AL: Pre: $N_{E\text{-}E}$: 4283 unit pairs, $N_{M\text{-}M}$: 1330 unit pairs, $N_{L\text{-}L}$: 434 unit pairs, 9 mice; Post: $N_{E\text{-}E}$: 2278 unit pairs, $N_{M\text{-}M}$: 1210 unit pairs, $N_{L\text{-}L}$: 304 unit pairs, 6 mice. V1-LM: early: CLES=0.537, $p=2.06\times10^{-7}$, middle: CLES=0.584, $p=8.19\times10^{-15}$, late: CLES=0.399, $p=3.37\times10^{-3}$; V1-AL: early: CLES=0.540, $p=3.93\times10^{-7}$, middle: CLES=0.554, $p=3.04\times10^{-6}$, late: CLES=0.504, p=0.869, Mann-Whitney U test with FDR-BH correction. (E) Percentages of highly correlated unit pairs within each mouse were plotted in boxplots. V1-LM: N_{pre}= 9 mice, N_{post}= 13 mice; V1-AL: N_{pre}= 9 mice, N_{post}= 6 mice. V1-LM: early: CLES=0.462, p=0.790, middle: CLES=0.55, p=0.790, late: CLES=0, p=0.068; V1-AL: early: CLES=0.630, p=0.665, middle: CLES=0.509, p=1, late: CLES=0.726, p=0.594, Mann-Whitney U test with FDR-BH correction. (F) V1-LM unit pairs were grouped into 25 groups based on their peak synchrony index in responses to 25 visual stimuli. Mean synchrony indices of each group were plotted in heatmaps. Statistically significant differences between post- and pre- experience for each group were labeled. See extended table 7-1 for sample sizes and detailed statistics. (G) Mean synchrony indices of each group for V1-AL unit pairs were plotted in heatmaps. Statistically significant differences between post- and pre- experience for each group were labeled. See extended table 7-1 for sample sizes and detailed statistics.

In parallel, we also examined spiking synchrony of unit pairs after entrainment of SF and TF that matched AL's functional preference. When we looked at the synchrony indices of all highly correlated unit pairs in response to the entrained SF and TF, the visually-locked (early-firing) units in V1 had significantly increased spiking synchrony with visually-locked (early-firing) units in LM, as well as with visually-locked (early-firing) units in AL (**Figure 2.12**A). Interestingly, post-stimulus (middle- and late-firing) units in V1 had significantly higher spiking synchrony with post-stimulus (middle- and late- firing) units in AL, but not with post-stimulus (middle- and late- firing) units (**Figure 2.12**A) in LM. However, the percentages of highly correlated unit pairs did not change significantly after the entrainment, for unit pairs either between V1 and LM, or between V1 and AL (**Figure 2.12**B). When we looked at the synchrony indices of unit pairs in each SF/TF group, the visually-locked unit pairs between V1 and LM in the entrained SF/TF group showed significantly increased spiking synchrony after the entrainment, while V1-LM visually-locked unit pairs in other SF/TF groups showed either increased or decreased spiking synchrony (**Figure 2.12**C left). The V1-LM post-stimulus unit pairs within the entrained SF/TF group showed an insignificant trend of increased spiking synchrony, and unit pairs in other SF/TF groups showed unchanged or decreased spiking synchrony (**Figure 2.12**C right). As for unit pairs between V1 and AL, the visually-locked unit pairs in the entrained SF/TF group did not show significant changes in spiking synchrony after the entrainment, but the visually-locked unit pairs in other SF/TF groups showed significantly increased spiking synchrony (**Figure 2.12**D left). The post-stimulus unit pairs between V1 and AL in the entrained SF/TF group showed significantly increased spiking synchrony, and the post-stimulus unit pairs in other SF/TF groups also showed significantly increased spiking synchrony (**Figure 2.12**D right). This result demonstrated that there was an overall increased unit population spiking synchrony between V1 and LM or between V1 and AL, while visually-locked unit pairs and post-stimulus unit pairs may exhibit changes in different directions, and the changes in spike synchrony were dependent on SFs and TFs.

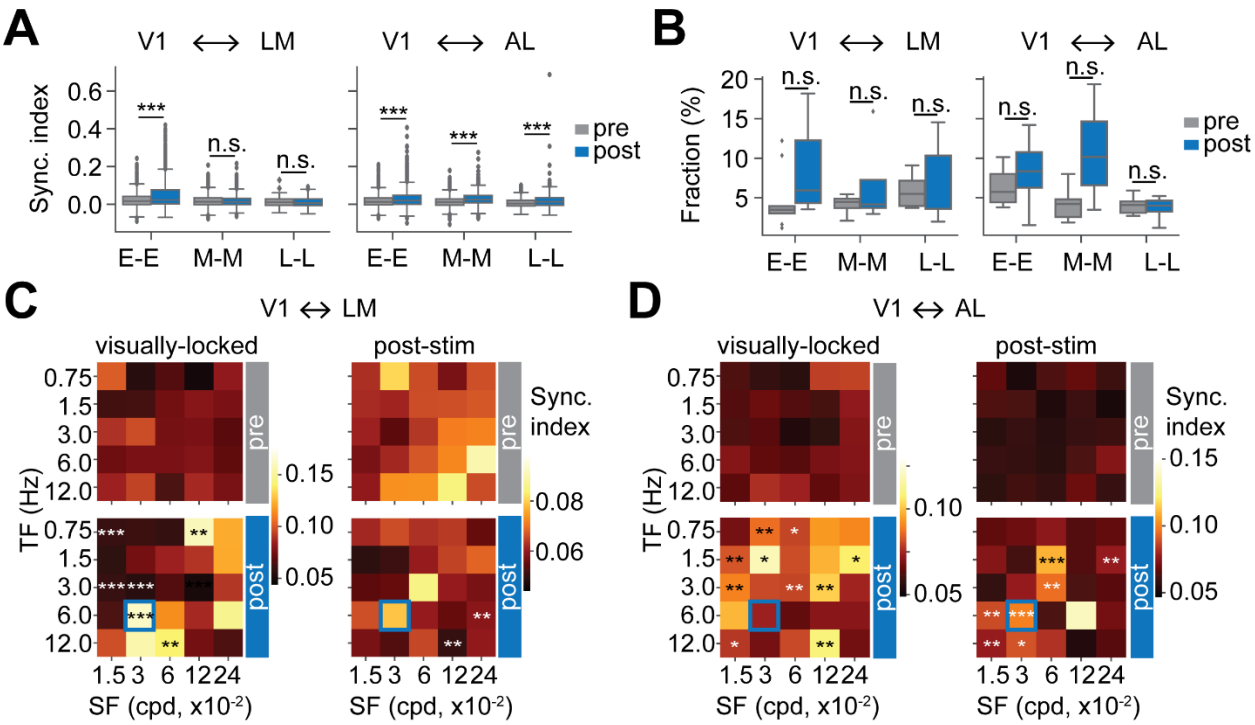

Figure 2.12. Inter-areal spiking synchrony increased after entrainment of SF and TF that matched AL's functional preference, especially for post-stimulus units. (A) Synchrony indices of highly correlated unit pairs in response to the entrained SF and TF were plotted in boxplots. Synchrony indices of early-early (E-E), middle-middle (M-M), late-late (L-L) unit pairs were analyzed. V1-LM: Pre: N_{E-E}: 1958 unit pairs, N_{M-M}: 1833 unit pairs, N_{L-L}: 120 unit pairs, 9 mice; Post: N_{E-E}: 2604 unit pairs, N_{M-M}: 818 unit pairs, N_{L-L}: 221 unit pairs, 6 mice. V1-AL: Pre: N_{E-E}: 3544 unit pairs, N_{M-M}: 1420 unit pairs, N_{L-L}: 363 unit pairs, 9 mice; Post: N_{E-E}: 1428 unit pairs, N_{M-M}: 562 unit pairs, N_{L-L}: 170 unit pairs, 6 mice. V1-LM: early: CLES=0.580, $p=6.93\times10^{-20}$, middle: CLES=0.499, p=0.957, late: CLES=0.499, p=0.957; V1-AL: early: CLES=0.573, $p=1.16\times10^{-15}$, middle: CLES=0.647, $p=7.16\times10^{-24}$, late: CLES=0.595, $p=3.96\times10^{-4}$, Mann-Whitney U test with FDR-BH correction. (B) Percentages of highly correlated unit pairs within each mouse were plotted in boxplots. V1-LM: N_{pre}= 9 mice, N_{post}= 6 mice; V1-AL: N_{pre}= 9 mice, N_{post}= 6 mice. V1-LM: early: CLES=0.815, p=0.155, middle: CLES=0.575, p=0.714, late: CLES=0.4, p=0.714; V1-AL: early: CLES=0.646, p=0.602, middle: CLES=0.870, p=0.065, late: CLES=0.5, p=0.927, Mann-Whitney U test with FDR-BH correction. (C) V1-LM unit pairs were grouped into 25 groups based on their peak synchrony index in responses to 25 visual stimuli. Mean synchrony indices of each group were plotted in heatmaps. Statistically significant differences between post- and pre- experience for each group were labeled. See extended table 8-1 for sample sizes and detailed statistics. (D) Mean synchrony indices of each group for V1-AL unit pairs were plotted in heatmaps. Statistically significant differences between post- and pre- experience for each group were labeled. See extended table 8-1 for sample sizes and detailed statistics.

To explore whether HVA activity contributes to persistent oscillatory activity in V1, we recorded V1 activity when HVA activity was optogenetically inhibited by activating AAV-CAG-ArchT injected outside of V1 (Figure 2.13A). The ArchT expression was confirmed outside of V1 and away from the V1 recording site (Figure 2.13B, top). A representative raster plot showed that a HVA unit was inhibited when laser power was large enough (Figure 2.13B, bottom). To examine post-experience V1 oscillations when HVA was inhibited, firing rate z-scores of V1 unit population were plotted in heatmaps (Figure 2.13C). The population averaged firing rate z-scores were significantly reduced at post-stimulus peaks, but did not show significant changes in the stimulus-locked peak (Figure 2.13D, E). This result suggested that the experience induced V1 post-stimulus responses were modulated by top-down HVA activity.

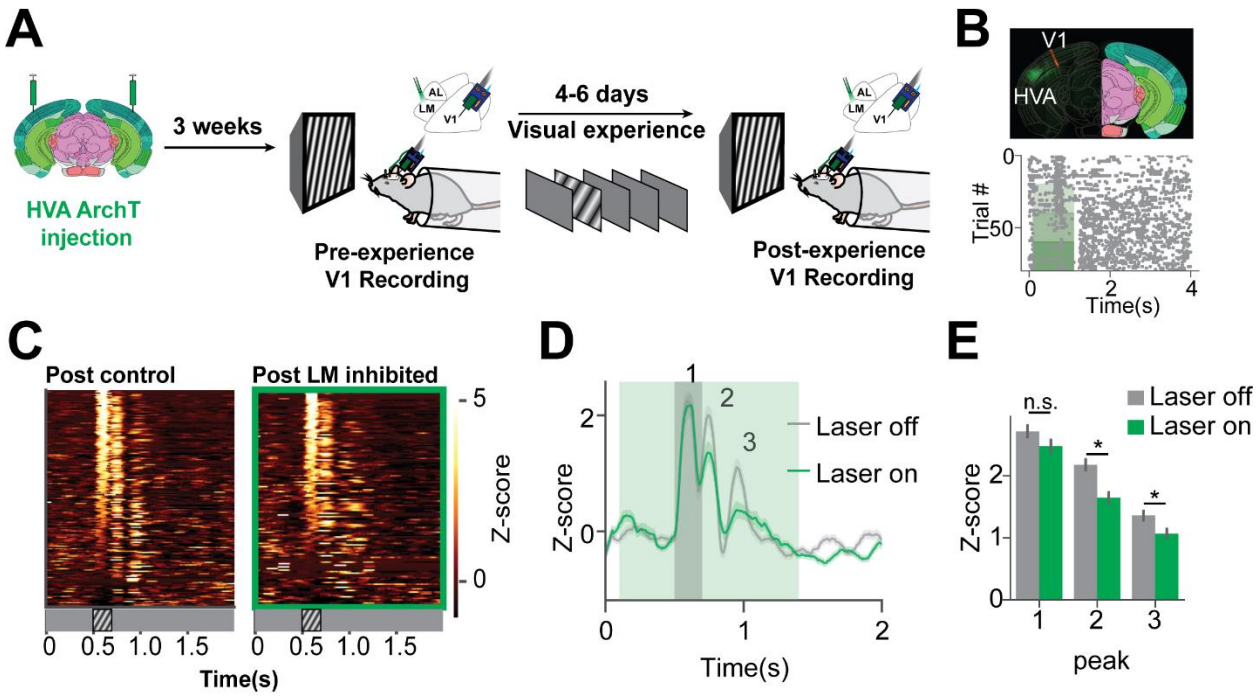

Figure 2.13. Optogenetic inhibition of HVA reduced V1 post-stimulus spiking. (A) AAV-ArchT-eYFP was injected outside V1. 3 weeks after virus injections, V1 was recorded with HVA inhibition pre- and post- visual experience. The stimulus used in the visual experience was drifting gratings (SF=0.04 cpd, TF=2 Hz). (B) Histology (top) showed that ArchT-eYFP (green) was expressed outside V1, and probe track (red) was in V1. The raster plot (bottom) showed a representative visually responsive LM unit that was inhibited when the 532nm laser turned on. The green shaded area represented the laser on duration, and the color intensities represented laser powers (2 mW, 4.5 mW, 10 mW). (C) Post-experience V1 units' firing rate z-scores over time were plotted in heatmaps. (D) Population averaged firing rate z-scores were compared between control and HVA inactivation for post-experience (post: $N_{control}$=$N_{LM\ ArchT}$=134 units, 5 mice). (E) Post-experience firing rate peak z-scores were plotted in bar plots. Data were represented as mean ± SEM. first peak: CLES=0.468, p=0.369, second peak: CLES=0.410, p=0.025, third peak: CLES=0.415, p=0.025, Mann-Whitney U test with FDR-BH correction. n.s.- not significant, *-p<0.05, **-p<0.01, ***-p<0.001.

2.5 Discussion

In this study, we demonstrated that visual experience induced persistent 4-8 Hz LFP oscillations not only in V1, but also in superficial layers of LM and AL. The presence of oscillations was not restricted to one of the HVAs, yet the 4-8 Hz oscillation power increases exhibited specificity to the entrained SF and TF, especially in LM and AL. Interestingly, the 4-8 Hz phase-locking between V1 and LM, but not between V1 and AL, significantly increased after visual experience with the SF and TF matching the functional preference of LM units. In parallel, the 4-8 Hz phase-locking between V1 and AL, but not between V1 and LM, significantly increased after visual experience with the SF and TF matching the functional preference of AL units. Additionally, the 4-8 Hz phase-locking exhibited specificity to the entrained SF and TF. Visually locked and post-stimulus responding units in V1, LM, and AL spiked at more consistent 4-8 Hz phases of local LFPs in response to the entrained SF and TF, regardless of which SF/TF was entrained. Intriguingly, after entrainment of SF/TF that preferentially induced LM response, the distribution of spike 4-8 Hz phases of visually locked and post-stimulus responding units in AL, but not in LM, became more concentrated and centered to be following the 4-8 Hz troughs of local LFPs. Correspondingly, after entrainment of SF and TF that preferentially induced AL response, the distribution of spike 4-8 Hz phases of visually locked and post-stimulus responding units in LM, but not in AL, became more concentrated and centered to be following the 4-8 Hz troughs of local LFPs. Units in V1, LM, and AL also showed stronger 4-8 Hz phase-locking inter-areally after entrainment of SF/TFs that matched either LM's or AL's functional preference, though there were no clear inter-areal phase preferences. When we tried to infer functional connection strength using spiking synchrony between unit pairs, visually locked units in V1 showed either increased or decreased spiking synchrony with visually locked units in LM or AL, dependent on the unit pairs' SF and TF preference. Post-stimulus responding units in V1 showed higher spiking synchrony with post-stimulus responding units in LM, as well as in AL, non-specifically to SF or TF. Optogenetic inhibition of HVAs also validated that V1 post-stimulus responses were modulated by HVAs.

Theta oscillations have been mostly studied in behavioral tasks previously. Theta synchrony between visual cortices can be observed in monkeys when they detected a pattern change in a visual stimulus, both when the stimulus was attended or not attended (Spyropoulos et al., 2018). Theta synchrony between visual and prefrontal cortices can also be detected during sustained

attention (Han et al., 2019), or visual working memory tasks (Liebe et al., 2012). Within the visual cortex alone, single units in theta phase locking are modulated by the visual content (Lee et al., 2005). Additionally, inter-areal activity patterns can report visual working memory information when a visual stimulus is absent (Harrison and Tong, 2009). Intriguingly, such oscillations also emerge in instances where do not require large cognitive demand, such as visual perceptual experience, and are modulated by a number of factors such as saliency (Huang et al., 2020b) and visual feature familiarity (Kissinger et al., 2018). Both experimental and computational data suggests the contribution of intra-cortical connections in producing the learning associated oscillations, which may sharpen response selectivity for visual stimuli (Lim, 2019; Gao et al., 2021). In our exploration of V1 and HVA activity, we found stronger 4-8 Hz LFP oscillations in superficial layers of V1, LM, and AL after visual experience. The 4-8 Hz power increase was not restrictedly present in one HVA when the entrained SF/TF matched one HVA's functional preference but not the other HVA's. However, the 4-8 Hz power increases showed specificity to the familiar SF/TF. The region non-specific increased 4-8 Hz oscillations suggested that there could be plastic changes in circuit activity in all of three regions, but uniform plastic changes across regions could not be assumed. Inter-areal 4-8 Hz phase-locking between superficial layer LFPs exhibited region specificity, where LM, but not AL, became more phase-locked to V1 in 4-8 Hz if the entrained SF/TF matched LM units' functional preference. Correspondingly, AL, but not LM, became more phase locked to V1 in 4-8 Hz if the entrained SF/TF matched AL units' functional preference. This 4-8 Hz synchrony between V1 and selective HVAs may indicate selective functional communication mediated by 4-8 Hz rhythm, as the inter-areal excitability coherence may influence efficacy of inter-areal communications (Fries, 2005; Bastos et al., 2015a; Kohn et al., 2020). Additionally, the inter-areal phase-locking exhibited specificity for the entrained SF and TF, suggesting its role in processing familiar visual content. We noticed that in pre-experience, neither area-selectivity, nor visual feature selectivity, of the 4-8 Hz phase locking was as strong as in post-experience, suggesting the experience was necessary for the expression of selective 4-8 Hz phase-locking.

Units' spikes became more modulated by local 4-8 Hz rhythm and clustered into visually locked units and post-stimulus responding units, especially in V1, after visual experience of SF/TFs that matched either LM's or AL's functional preferences. Unit population in both LM and AL exhibited increased 4-8 Hz phase-locking (PPCs), regardless which SF and TF were entrained,

but the distributions of spike phases in LM and AL showed some differences. After entrainment of SF/TF that matched LM's functional preference, post-stimulus middle-firing units in AL instead of LM tended to spike more following 4-8 Hz troughs of local LFPs, while after entrainment of SF/TF that matched AL's functional preference, post-stimulus middle-firing units in LM instead of AL tended to spike more following 4-8 Hz troughs of local LFPs. The suprathreshold spiking activity appeared not to reconcile with LFP data, yet it might suggest that the 4-8 Hz oscillations was not primarily attributed to rhythmic population spiking but subthreshold 4-8 Hz rhythm. Nevertheless, this plausible explanation does not exclude the possibility that a subset of functional excitatory connections would strengthen under influence of coherent excitability change in 4-8 Hz. Temporally synchronized activity is likely to induce functional connectivity change, and we explored this possibility in our data by calculating jitter corrected cross-correlations between spike trains from simultaneously recorded unit pairs. Despite that extracellular activity fails to capture subthreshold change, the spiking synchrony may still suggest functional connection strength for the connections formed with units with suprathreshold spiking. After entrainment of SF and TF that matched either LM's or AL's functional preferences, there were more visually locked unit pairs that showed high spiking synchrony, both between V1 and LM and between V1 and AL. For the post-stimulus responsive units, there were more post-stimulus responding unit pairs between V1 and AL that showed high spiking synchrony after either SF/TF entrainment, while the post-stimulus responding unit pairs between V1 and LM had higher spiking synchrony only when the entrained SF/TF matched LM's functional preference. The fractions of highly correlated unit pairs did not show significant changes for either visually-locked unit pairs or post-stimulus unit pairs, after either SF/TF entrainment, but it did not exclude the possibility of changed number of functional connections, as subthreshold change could not be captured well by extracellular recordings, especially in the depression direction, which could be better assessed using future patch clamp experiments. Additionally, when we separated highly correlated unit pairs based on where they showed highest synchrony, we found that the inter-areal spiking synchrony between visually locked units was dependent on their functional preferences for SF and TF, though clear association was not obvious. The inter-areal spiking synchrony between post-stimulus units in V1 and LM increased nonspecifically to the entrained SF and TF after entrainment of SF and TF that matched LM's functional preference, but unchanged overall after entrainment of SF and TF that matched AL's functional preference. Meanwhile, the inter-areal spiking synchrony between post-stimulus

units in V1 and AL showed increase nonspecifically to the entrained SF and TF after entrainment of SF and TF that matched LM's functional preference, and showed increase in more SF/TF groups after entrainment of SF and TF that matched AL's functional preference. The unclear specificity of inter-areal spiking synchrony change could be attributed to the fact that LM and AL shared some functional similarities as they were at low hierarchy of the visual cortices.

The persistent phase-locking between V1 and a selective HVA provided a way for communication in selective circuitry, but it remains unknown what functional role of the persistent 4-8 Hz modulated activity would play. One plausible explanation is to keep visual information online through resonating circuit components for visual feature processing, so that the visual cortex is primed to integrate other information if the visual information became associated with cognitive demand. It would be interesting to assess the inter-areal functional connections in behavior relevant tasks between visual cortices or between visual cortex and other regions. The 4-8 Hz synchronization between V1 and other brain regions, such as the prefrontal cortex and retrosplenial cortex, would be interesting to look at, as other studies suggested that top-down projections might alter local gain by affecting local interneurons (Zhang et al., 2014b), that are known to regulate oscillation frequencies (Chen et al., 2017).

In summary, we demonstrated persistent 4-8 Hz LFP phase locking between V1 and a selective HVA that had functional preference matched the entrained SF and TF, after visual experience, as well as 4-8 Hz modulated unit spiking universally in V1 and HVAs. These results provided evidence, for the first time, that experience induced 4-8 Hz activity modulated functional interactions between visual cortical areas, which may serve to route selective communications between visual cortices.

2.6 Contribution statement

Yu Tang (Y.T.) and Alexander A. Chubykin (A.A.C.) conceptualized and designed the *in vivo* electrophysiology experiments. Y.T. conducted animal surgeries, extracellular recordings, post-recording histology, confocal microscopy imaging, neural signal and image data analysis. Y.T. wrote the original draft. Y.T. and A.A.C. reviewed and edited the final draft. A.A.C. acquired funding.

2.7 Acknowledgement

We thank the Chubykin lab members for discussions during the development of the project, especially Michael P. Zimmerman and Mang Gao for comments on the original draft. We thank Dr. Scott Pluta for critical comments during the development of the project. We also thank Dr. Sotiris Masmanidis for providing silicon probes. This work was funded by the National Institute of Mental Health (R01 571 MH116500) to A.A.C..

2.8 Work in progress and future directions

The persistent 4-8 Hz synchrony between visual cortices suggested functional interactions between areas even after the visual stimulus was absent, yet the behaviorally relevant role of such delayed activity is still not explored. To assess the role of the delayed visual cortical activity in a behavioral context, we developed a "Go/No-go" touchscreen behavior paradigm (Figure 2.14A). In this task, a "Go" stimulus (pink noise with SF=0.12 cpd, TF=0.75 Hz, which matched LM's functional preference, displayed for 5 s) and a "No-go" stimulus (pink noise with SF=0.03 cpd, TF=6 Hz, which matched AL's functional preference, displayed for 5 s) were presented to mice, followed by a 5.5 s gray screen. The mice had to touch the gray screen following the "Go" stimulus (0.5 s after its onset) to receive a sucrose (1/12 v/v) water reward (40 µl), but not the "No-go" stimulus, to avoid a time-out punishment. To train the mice to learn the task, mice were water-restricted (body weight kept >80% of the body weight on the day before water restriction) and multiple pre-training stages were used similarly in other studies (Stirman et al., 2016; Pak et al., 2020). The mice first underwent a "Free reward" stage, during which mice learned where the reward was delivered (100% reward consumption for at least two consecutive days), and then they underwent a "Must touch" stage, during which mice learned to touch the screen (a gray screen) to receive a reward (>60% touches for at least two consecutive days) (Figure 2.14B). Later, the two pink noise stimuli were introduced, and the mice learned to touch the "Go" stimulus to receive a reward, but not to touch the "No-go" stimulus to avoid a punishment (>60% touches for the "Go" stimulus, and <40% touches for the "No-go" stimulus) (Figure 2.14C). Finally, the gray screen following the stimulus was introduced, and the mice learned to touch the gray screen following the "Go" stimulus but not the gray screen following the "No-go" stimulus (>60% touches for the "Go" stimulus, and <40% touches for the "No-go" stimulus) (Figure 2.14D). After mice

successfully learned the task or their performance hit plateau, optogenetic manipulation was applied in a test stage. To test the necessity of the delayed activity in the visual cortex, we utilized the PV-Cre and Ai32 (carried DIO-ChR2) cross-bred mouse line (PV-Cre x Ai32) to inactivate V1 (±1.0 mm anterior, ±4.0 mm lateral to the lambda) by activating PV+ interneurons through their ChR2 expression (Figure 2.14E). Optic ferrules were implanted on top of visual cortices before experiments, and at least three days were allowed for mice to recover from surgeries before water restriction. For experiments to test the necessity of LM delayed activity, we injected AAV-CAG-ArchT locally in LM (±1.0 mm anterior, ±4.0 mm lateral to the lambda, 25-30 nl at 300 μm and 600 μm below the brain surface) before implanting optic ferrules on LM, and 3 weeks were allowed for ArchT expression before behavioral training (Figure 2.14F). Before the test stage, mice first habituated to the connected cables for at least one day, and then during the test stage, blue light (473 nm, laser power 3-4.5 mW measured at the exposed tip of the cable) was delivered through the cables to V1 for experiments on PV-Cre x Ai32 mice, and green light (532 nm, laser power 3-4.5 mW measured at the exposed tip of the cable) was delivered to LM for experiments on mice injected with ArchT.

For experiments on PV-Cre x Ai32 mice, the percentage of touches following "Go" stimulus decreased when V1 was inactivated for at least one mouse, while the percentage of touches following "No-go" stimulus did not change much (Figure 2.14E). For experiments on mice with ArchT injected in LM, the percentage of touches following "Go" stimulus also decreased for most of mice, and intriguingly the percentage of touches following "No-go" stimulus of some mice increased while most of the mice kept low percentage of touches when LM was either inhibited or not (Figure 2.14F).

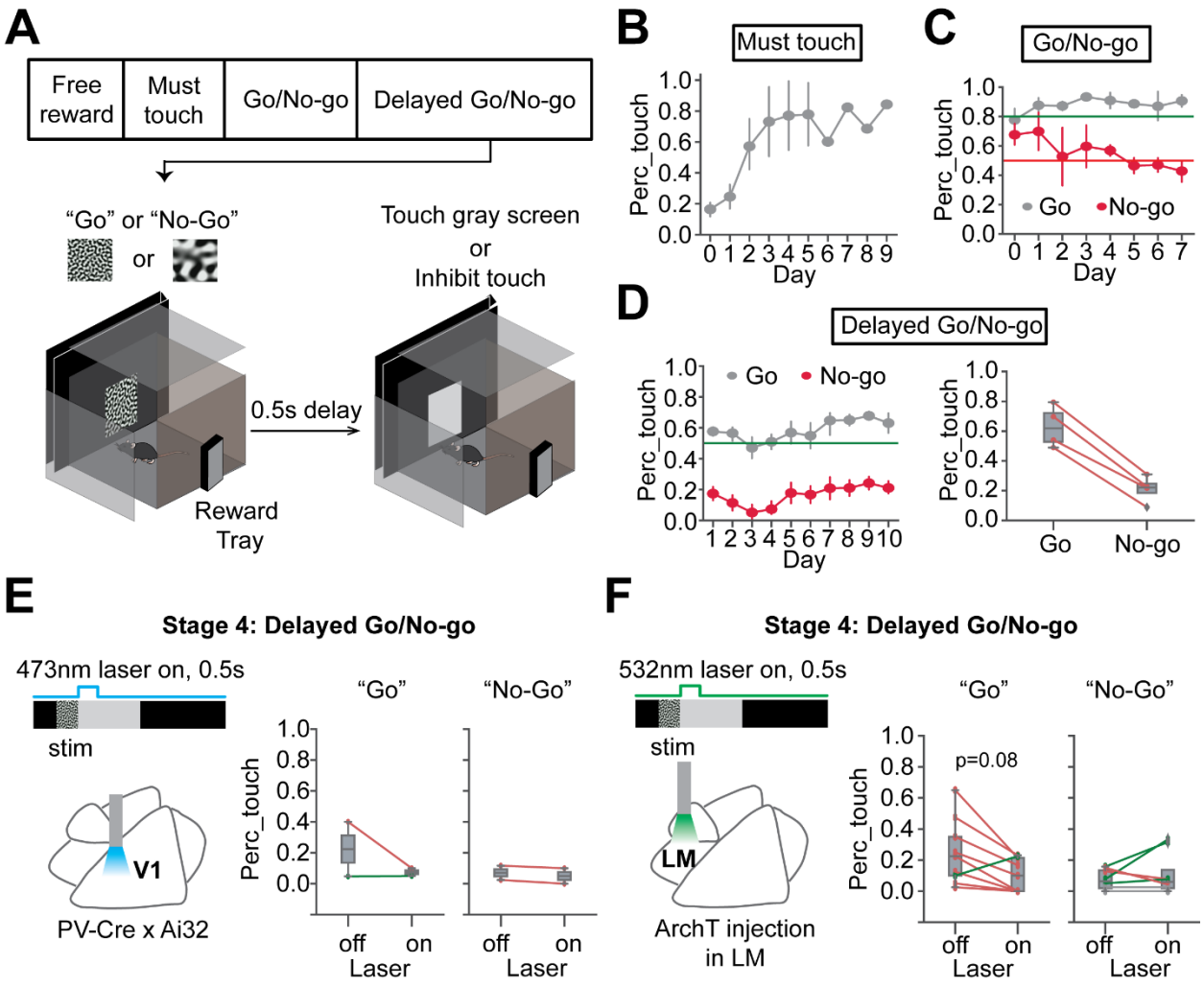

Figure 2.14. The role of V1 activities during and after visual stimulation in a visually cued delayed Go/No-go task. (A) Visually cued delayed Go/No-go task in operant conditioning chambers. Behavioral training consists of four stages, including the free reward stage, the must touch stage, the Go/No-go stage, and the delayed Go/No-go stage. The schematics demonstrates the detailed schedule for the delayed Go/No-go stage. Pink noise stimuli filtered at two spatial frequencies were used as visual cues. (B) Percentages of touches in the must touch stage. N=4 mice. (C) Percentages of touches in the Go/No-go stage. N=4 mice. (D) Percentages of touches following Go and No-go stimuli in the delayed Go/No-go stage over days (left), and on the last day (right). N=4 mice. (E) V1 was inhibited by activating PV interneurons using the PV-Cre x Ai32 mouse line. Laser was turned on after the visual stimulation time window and during the delay period. The box plots (right) showed the percentages of touches. N=2 mice. (F) LM was inhibited by activating ArchT injected in LM. Laser was turned on after the visual stimulation time window and during the delay period. The box plots (right) showed the percentages of touches. N=9 mice.

2.9 Contribution statement of the behavior experiments

YT and AAC conceptualized the experiments. YT designed the behavior experiment protocol. Catherine Gervais (CG) and YT conducted virus injections and ferrule implantation. YT, CG, and Rylann Moffitt (RM) executed behavior training. YT analyzed and summarized data. YT wrote the experiment description.

CHAPTER 3. RESTORATION OF VISUAL FUNCTION AND CORTICAL CONNECTIVITY AFTER ISCHEMIC INJURY THROUGH NEUROD1-MEDIATED GENE THERAPY

Adopted from: Tang Y, Wu Q, Gao M, Ryu E, Pei Z, Kissinger ST, Chen Y, Rao AK, Xiang Z, Wang T, Li W, Chen G, Chubykin AA (2021) Restoration of Visual Function and Cortical Connectivity After Ischemic Injury Through NeuroD1-Mediated Gene Therapy. Front Cell Dev Biol 9:720078.

3.1 Abstract

Neural circuits underlying brain functions are vulnerable to damage, including ischemic injury, leading to neuronal loss and gliosis. Recent technology of direct conversion of endogenous astrocytes into neurons *in situ* can simultaneously replenish the neuronal population and reverse the glial scar. However, whether these newly reprogrammed neurons undergo normal development, integrate into the existing neuronal circuit, and acquire functional properties specific for this circuit is not known. We investigated the effect of NeuroD1-mediated *in vivo* direct reprogramming on visual cortical circuit integration and functional recovery in a mouse model of ischemic injury. After performing electrophysiological extracellular recordings and two-photon calcium imaging of reprogrammed cells *in vivo* and mapping the synaptic connections formed onto these cells *ex vivo*, we discovered that NeuroD1 reprogrammed neurons were integrated into the cortical microcircuit and acquired direct visual responses. Furthermore, following visual experience, the reprogrammed neurons demonstrated maturation of orientation selectivity and functional connectivity. Our results show that NeuroD1-reprogrammed neurons can successfully develop and integrate into the visual cortical circuit leading to vision recovery after ischemic injury.

3.2 Background on NeuroD1 mediated astrocyte to neuron conversion for neuron replenishment after CNS injuries

Central nervous system (CNS) injuries, such as ischemic stroke, cause neuronal loss and impair brain functions. Such conditions are hard to treat due to adults' limited capability in neuroregeneration. In focal ischemic injury, local blood vessel occlusion induces neuronal loss and astrocyte reactivation/proliferation at the damage core and periphery, respectively. The glial scar formed with reactive astrocytes is beneficial in containing the tissue damage, but also is a

barrier for neuroregeneration (Silver and Miller, 2004). Several treatment strategies have been developed to replenish neurons after CNS injuries, including transplanting differentiated neurons or neuronal progenitor cells into the CNS, inducing adult neurogenesis *in vivo*, as well as converting endogenous non-neuronal cells directly into neurons *in vivo* (Li and Chen, 2016). Among these strategies, direct *in vivo* cell conversion has gained a lot of research interests because it circumvents the potential tumorigenesis and graft rejection that could happen in stem cell-based therapies (Chen et al., 2020). In many neurological diseases and brain injuries, astrocytes become active and proliferate. A neurogenic transcription factor NeuroD1, has been shown to efficiently convert non-neuronal cells directly into neurons without the pluripotent stage both in vitro and *in vivo* (Vierbuchen et al., 2010; Guo et al., 2014). Lots of efforts have been made in validating its efficiency in converting astrocytes to neurons (Xiang et al., 2021), yet whether the converted neurons integrate into the pre-existing circuit or exhibit appropriate physiological functions need more in-depth research.

Injury can induce cortical circuit reorganization in adults (Nahmani and Turrigiano, 2014). Despite the fact that most circuit plasticity happens during the development, plastic changes in the visual cortex can be induced in the adulthood after injury or monocular deprivation of visual inputs. After focal ischemic stroke, the undamaged neurons may undergo plastic changes if reperfusion happens within a week post-injury. The plastic changes are surprisingly similar to the changes following monocular deprivation during the critical period. The GABAergic neurons become less active initially, which allows increased activity in excitatory neurons and their neurite extension to form new connections. However, such plastic changes are mostly compensatory and rarely restore the cortical circuit functions in case of severe injuries (Grade and Gotz, 2017). The circuitry formed with directly reprogrammed cells *in vivo* is less studied, but recent studies suggested that whether the *in situ* reprogrammed neurons acquire appropriate regional identities is under the influence of local microenvironment of molecular signaling and glial cells' transcriptome (Wang et al., 2021).

Lots of research efforts have been made in studying the circuit integration of cells that are transplanted exogenously. Trans-synaptic tracing studies show that transplanted cells that are differentiated from stem cells can form local and long range synaptic connections with host cells, and optogenetic silencing the transplanted cell confirmed their contribution to the functional recovery (Steinbeck et al., 2012; Michelsen et al., 2015; Tornero et al., 2017). *In vivo*

reprogrammed neurons also showed the ability to form appropriate circuit connections (Mattugini et al., 2019; Wu et al., 2020).

3.3 Introduction

Functional circuit impairment associated with neuronal loss is commonly seen in patients with brain injuries, such as ischemia. Though neural stem cells (NSCs) exist in the subventricular zone (SVZ) in the adult brain, they are found to differentiate mainly into astrocytes when they migrate to injured cortex (Benner et al., 2013; Faiz et al., 2015), and their neurogenesis capacity is too limited to compensate for the neuronal loss. Currently, it remains a challenge to generate neurons in adults and functionally incorporate them into the local circuits. Several strategies have shown the capability to induce neurogenesis and lead to some behavioral recovery. One promising approach is to transplant stem cell-derived neurons or neural progenitor cells (Tornero et al., 2013; Michelsen et al., 2015; Somaa et al., 2017). Yet, there are concerns about graft rejection and tumorigenicity of the transplanted cells (Erdo et al., 2003; Marei et al., 2018). Meanwhile, progress has been made in reprogramming non-neuronal cells, such as fibroblast and glial cells, into neurons directly by expressing transcription factors (Marro et al., 2011; Yang et al., 2011; Grande et al., 2013; Niu et al., 2013; Blanchard et al., 2014; Heinrich et al., 2014; Torper et al., 2015; Mattugini et al., 2019; Nolbrant et al., 2020). Brain injuries, including ischemic injury, trigger re-activation and proliferation of astrocytes around the injury site. Although the initial stage of gliosis may be beneficial to confining the injury, glial scarring in the later stage is detrimental to axonal regeneration, neural circuit rewiring, and functional recovery (Fitch and Silver, 2008; Kawano et al., 2012). One transcription factor NeuroD1, which has been demonstrated to convert human ESCs and iPSCs into neurons *in vitro* (Zhang et al., 2013), also showed great efficacy in converting astrocytes to neurons *in situ*, bypassing the pluripotent and proliferating stem cell stage (Guo et al., 2014; Chen et al., 2015; Li and Chen, 2016; Brulet et al., 2017; Chen et al., 2020), and a recent study confirmed that the converted cells originated from astrocytes using lineage tracing labeling (Xiang et al., 2021). It is possible that a small number of astrocytes that were converted originated from NSCs, but the limited number of NSCs-originated astrocytes alone in adult brains might not be able to compensate for the neuronal loss in ischemic injury. It has been shown that NeuroD1-mediated astrocyte-to-neuron conversion supported behavioral function recovery following ischemic injury in the motor cortex and the converted neurons form structural connections with

thalamic neurons (Chen et al., 2020; Ge et al., 2020). Despite the demonstration of the behavior recovery, whether the newly transformed neurons integrate into the local circuits and perform appropriate functions is less clear.

Several questions remain unanswered: do the reprogrammed cells become integrated into the functional circuit in brain regions that have complex circuit structures, like cortices? Do they gain the functional properties of a typical neuron and become part of the specific circuit? Do the reprogrammed cells undergo a classical developmental path of regular neurons, or is their developmental trajectory different? Finally, how safe is this process of converting a non-neuronal cell into a neuron? Do these cells stay neurons, or do they gain other potentially aberrant cellular properties?

Answering these questions is critical for the development of new regenerative therapies for brain injuries. We have decided to answer some of these questions using the mouse primary visual cortex, which provides unique advantages as a model system. It is easily accessible for *in vivo* electrophysiological recordings and calcium imaging in awake mice. It is responsive to visual stimulation, providing an opportunity to characterize cortical cells' functional properties using quantitative visual tests and various stimuli.

To examine the functional recovery of the visual cortex after ischemic injury, we directly measured neuronal activity and response selectivity in the NeuroD1-treated visual cortex in awake mice and mapped the connectivity of the individual newly reprogrammed neurons in *ex vivo* brain slices. Visual response and circuit connectivity strength were characterized longitudinally after reprogramming, revealing local circuitry remodeling and visual response recovery. Furthermore, the reprogrammed cells' orientation selectivity improved over time as assayed by two-photon calcium imaging and extracellular recordings at different developmental stages following reprogramming. These findings suggest that NeuroD1-mediated reprogramming of astrocytes into neurons leads to neuronal regeneration and functional recovery of vision after ischemic injury.

3.4 Materials and methods

3.4.1 Animals

Wild type male and female C57BL/6 mice (Jackson Laboratory and Purdue University Transgenic Mouse Core Facility, postnatal day 34-90) were used for *in vivo* extracellular recording

experiments. Thy1-ChR2-YFP line 18 [B6.Cg-Tg(Thy1-COP4/EYFP)18Gfng/J, JAX stock #007612] was used for *ex vivo* cortical slices preparation and whole cell patch-clamp experiments. All animals were housed in 12-h light/dark cycle with *ad libitum* access to rodent chow food and water. All experimental animal use was approved by the Purdue University Animal Care and Use Committee and followed guidance issued by the National Institutes of Health.

3.4.2 Surgery, ischemic injury induction, and virus injections

Mice were anesthetized during all surgical procedures with inhaled isoflurane (5% for initial induction and 1.5% for maintaining anesthesia, carrier gas was room air, SomnoSuite system). Deep anesthesia was confirmed by no response to toe/tail pinch. The skin over the skull was removed, and the skull over the cortices was exposed. The craniotomy was made first by thinning a small area of the skull about 0.5 mm diameter at the injection site with a drill. Then, a tiny gap at the center of the hole for inserting the micro-injection pipette was opened using a sterile needle. To induce focal ischemia, a total volume of 1 μl of 4 μg/μl endothelin-1 (ET-1, Sigma) was injected into V1. ET-1 was dissolved in filter-sterilized pure water to make a stock solution which was stored at −80°C and diluted to the final concentration with filter-sterilized artificial cerebral spinal fluid (ACSF) before each injection. ET-1 solution was injected at two depths, 700 μm and 300 μm below the brain surface, 500 nl per depth at 100 nl/min rate using a microinjector (NanoJect II or NanoJect III, Drummond Scientific). For sham injections, 1 μl of ACSF was injected at the same speed and depths. For mice used in extracellular recording experiments, a head post (or head plate for 2 photon imaging) was adhered to the skull at 4 mm anterior to bregma, and a gold-plated grounding pin (Parkell) was installed 1 mm anterior to bregma by inserting the sharp end through the skull into the midline space (but not in the brain tissue). Following the procedures, acrylic dental cement (Metabond, C&B) was applied to the exposed skull to create a protective hard cap and to secure the head post and the grounding pin. Ground pin installation were omitted for animals for *ex vivo* brain slice preparation and 2 photon calcium imaging. 8-10 days after ET-1 injections, two adeno-associated viruses (AAV9), one carrying FLEX-NeuroD1-mCherry and the second carrying GFAP::Cre were injected together (10:1 ratio, 1ul total volume, injected at the same depths and speed as ET-1 injection) through the same craniotomy. Coordinates used for primary visual cortices injections were (relative to lambda): 0.8 mm anterior, ±3.0 mm lateral for animals used in extracellular recordings; or 0.8 mm anterior, ±2.8 mm lateral for animals used

in *ex vivo* slice recordings. For the 2-photon calcium imaging and optotagging experiments, ET-1 was injected in both hemispheres as described earlier. 8-10 days after ET-1 injection, AAV9-CAG::GFAP-Cre, AAV9-CAG::FLEX-NeuroD1-mCherry, and AAV9-CAG::FLEX-GCaMP6s (for 2 photon calcium imaging, Addgene, 100842) or AAV5-DIO-ChR2-eYFP (for optotagging, Addgene, 20298) were injected together (2:10:10 ratio) into both hemispheres at 700µm and 300µm below the brain surface (500 nl per depth, speed 1 nl/s).

3.4.3 *In vivo* extracellular recording preparation

Mice were habituated to the head-fixed recording setup for at least 4 days, 90 min per day, prior to recordings. Mice were head-fixed, and their bodies were loosely restrained in a tube on a platform. A monitor (21.5″ ViewSonic VX2252MH, or 25″ Alienware AW2518Hf) was positioned 16.5 cm in front of the platform showing a gray screen during habituation sessions. On recording days, small cranial windows (~1 mm^2) were made at the injection sites while mice were anesthetized by isoflurane inhalation. Mice were placed on the head-fixed setup after craniotomies, and a silicon probe was inserted into the cranial window. For optotagging experiments, an optical fiber (Thorlabs, 0.39NA TECS hard-clad, multimode, step-index fibers, FT200EMT) connected to a blue light laser (OEM laser, 100 mW 473 nm DPSS laser system) was positioned right above the brain surface as adjacent to the recording probe insertion site as possible. Recordings started 30 min after probe insertion to allow for recovery from anesthesia and tissue settling. Filter-sterilized ACSF was added on top of the exposed brain surface to prevent desiccation from dehydration.

3.4.4 Visual stimulation and *in vivo* optogenetics stimulation

All visual stimuli were generated using PsychoPy (Peirce, 2007). The full-field gray screen was used for habituation (mean luminance 73 cd/m^2). In one stimulus recordings, sinusoidal drifting gratings (0.04 cycles per degree, drifting at 2 Hz, oriented 30 degrees to the vertical direction) were presented for 20 trials. In each trial, the stimulus was presented for 0.2s, preceded by 0.5 s gray screen, followed by 5-6 s gray screen inter-trial interval (**Figure 3.2**A). For direction tuning recordings, sinusoidal drifting gratings (0.04 cycles per degree, drifting at 1 Hz, oriented 0, 30, 60, 90, 120, and 150 degrees) were pseudo-randomly presented for 60 trials. Within each trial,

the stimulus was presented for 1 s, preceded by 0.5 s gray screen, followed by 5-6 s inter-trial interval (**Figure 3.2**A). For optogenetics experiments, light stimulation was applied after all visual stimulation experiments to identify cells that co-express NeuroD1 and ChR2. 500 ms light pulses (5-10 mW measured at the fiber tip) were applied for 20 trials.

3.4.5 Extracellular recording data acquisition and analysis

64-channel silicon probes (Shobe et al., 2015) were used for all recordings. Raw data were digitized at 30kHz and acquired through an OpenEphys acquisition board (Siegle et al., 2017). Local field potentials were obtained by band-pass filtering the raw data between 0 and 300Hz with an additional 60-Hz notch filter to attenuate electrical noise. The channels within the depth range of layer 4 (300 to 500 μm below the brain surface) that showed the first strongest negative response to visual stimulation were used for visually evoked potential (VEP) analysis. The most negative value within the visual stimulation time window was used as the VEP amplitude. Time-frequency analysis of LFP was performed by using a series of complex wavelets to extract power and phase at each sample point. Band powers were calculated by averaging powers within 500ms after the visual stimulation onset.

Spikes were clustered into units using Kilosort (Pachitariu et al., 2016). Units were then manually inspected in Phy (Rossant et al., 2016) template graphical user interface (GUI) to remove units that have noise-like waveforms (artifact-like or have no clear refractory period). Single units were classified as regular-spiking (RS), fast-spiking (FS), and unclassified (UN) units, based on their averaged template waveforms. Units that have averaged template waveform with trough-to-peak duration less than 0.45ms and spike width less than 1ms were classified as putative FS units. Units that had template waveform with trough-to-peak duration more than 0.45 ms and spike width more than 1ms were classified as RS units. Units that did not satisfy either criterion were classified as UN units. Spike width was calculated by inverse peak frequency of the spike spectrum (Stark et al., 2013). Peri-stimulus time histograms (PSTHs) of single unit activities were computed using 10ms bins and smoothed with a Gaussian Kernel (width=100 ms). Z-scores of single unit firing rate (FR) were calculated by normalizing FR to the mean FR across the duration of each trial (z = (FR-mean FR)/standard deviation of FR). Mean FR within the visual stimulation time window was used as the response to each direction. FR at each orientation was obtained by averaging the FR at the same orientation of two directions. Tuning curves for each group were obtained by fitting unit

averaged FR at 6 orientations to Gaussian functions or by interpolating a cubic function. One minus direction circular variance (1-DCV) was calculated using $\left|\frac{\sum_k R(\theta_k)\exp(i\theta_k)}{\sum_k R(\theta_k)}\right|$, and one minus orientation circular variance (1-CV) was calculated using $\left|\frac{\sum_k R(\theta_k)\exp(2i\theta_k)}{\sum_k R(\theta_k)}\right|$, where θ_k was the direction k (0-2π) or orientation k (0-π) in radians, and $R(\theta_k)$ was the mean firing rate within the stimulus time window (Mazurek et al., 2014).

3.4.6 Histology and immunohistochemistry (IHC)

Mice were anesthetized with 100 mg/kg ketamine and 16 mg/kg xylazine through IP injection before trans-cardiac perfusion. Deep anesthesia was confirmed with no reflex to toe/tail pinch. The thorax and abdomen were opened. A needle was inserted into the left ventricle of the heart, and a small incision was made in the right atrium. Mice were first perfused with 1x phosphate-buffered saline (PBS, 15 to 20 ml) until the liver cleared, then with 4% paraformaldehyde (PFA, 10 to 15 ml) for fixation. Mouse brains were post-fixed in 4% PFA for an additional 12-36 hr before histology. Fixed brain tissue was sliced using a vibrating microtome (1000 Plus, TPI Vibratome) at 50 μm thickness. When IHC staining was unnecessary, slides were made directly by mounting the slices with anti-fade mounting medium containing 0.2% n-propyl gallate. When IHC is necessary, the 50μm slices were stained free-floating in 24-well tissue culture plates. They were first blocked and membrane permeabilized in 5% bovine serum albumin (BSA) and 0.1%-2% Triton X 100 (TX 100, Sigma) in PBS at room temperature for 0.5-1 hour. Then, the slices were incubated with the primary antibody in 0.1% TX 100 for 36 to 48h at 4°C followed by the secondary antibody for 1 to 2h at room temperature. Slices are washed in PBS in between antibody incubations. Slices were counterstained with DAPI when necessary. For Ctip2 and Satb2 staining, slices were treated in 80°C sodium citritate buffer for 20 minutes before blocking. The slices were mounted using the same method described above. Antibodies used are: Anti-Glial Fibrillary Acidic Protein Antibody (AB5541, Millipore Sigma), Anti-NeuN Antibody (ABN78, Millipore Sigma), Anti-Satb2 Antibody (ab51502, abcam), Anti-GABA Antibody (A2052, Sigma), Anti-Cux1 Antibody (11733-1-AP, proteintech), Anti-Ctip2 Antibody (ab18465, Abcam), Anti-Tbr1 (AB10554, Millipore Sigma), Alexa Fluor® 488 AffiniPure Donkey Anti-Rabbit IgG (H+L) (Code: 711-545-152, Jackson ImmunoResearch), Alexa Fluor® 647 AffiniPure Donkey Anti-Rat IgG (H+L) (Code: 712-605-150, Jackson ImmunoResearch), and Alexa Fluor® 647

AffiniPure Goat Anti-Chicken IgY (IgG) (H+L) (Code: 103-605-155, Jackson ImmunoResearch). Brain slices were imaged under a confocal microscope (Zeiss LSM710). Neurite tracing and reconstruction was conducted using Fiji/ImageJ. For quantification of marker positive reprogrammed cells, ROIs were identified on the mCherry channel, and the intensities of the markers were measured within ROI. Normalized intensity above threshold (1.5 times of median intensity of each slice for) is considered as positive marker cell.

3.4.7 Experimental design and statistical analysis

Experimental groups and controls are described in detail with the results. Data were analyzed using custom-written scripts in Python. Data normality was tested using the Shapiro-Wilk normality test and statistically tested using the SciPy, Statsmodels, or Pingouin (Vallat, 2018b) statistical packages. For normally distributed data, a Student's t-test was used for pair-wise comparisons, or ANOVA was used for comparison among multiple groups. For non-normally distributed data, non-parametric tests were used. Mann-Whitney U test was used for comparing two distributions with similar shape; Kruskal-Wallis H-test was used for comparing multiple distributions with similar shape, and the Kolmogorov-Smirnov test was used for comparing two distributions with different shapes. Group distributions of VEP amplitudes, LFP frequency band powers, unit firing rate z-scores, EPSCs amplitude were compared using non-parametric Mann-Whitney U test with effect size reported. Unit counts were compared using Kruskal-Wallis H-test. 1-DCV and 1-CV cumulative distributions were compared using the two-sample Kolmogorov-Smirnov test. See the results section for the specific test used in each case and the test statistic values.

3.5 Results

3.5.1 NeuroD1 efficiently converted astrocytes into neurons that acquired cortical neuron identity in the visual cortex

To demonstrate the effects of *in vivo* direct reprogramming on visual function following cortical ischemic injury, we assessed visual responses using *in vivo* extracellular recordings in awake mice. To measure how newly converted neurons integrated into the local cortical circuits, we used *ex vivo* channelrhodopsin-assisted circuit mapping (CRACM) in acute brain slices

(**Figure 3.1A**). At nine days after endothelin-1 (ET-1) injection, robust gliosis and neuronal loss were confirmed by astrocyte marker GFAP and neuronal marker NeuN staining, which showed a significant increase in astrocyte/neuron ratio (**Figure 3.1B, C**). The induced glial scar did not resolve if no treatment was applied (**Figure 3.2A** middle). After the glial scar was formed, we delivered the Cre-dependent reprogramming gene NeuroD1 (CAG::FLEX-NeuroD1-mCherry) along with the Cre-recombinase gene under the GFAP promoter (GFAP::Cre) targeting astrocytes using adeno-associated virus (AAV9). The astrocytes underwent a transition to neurons, where they temporarily expressed both GFAP and NeuN (**Figure 3.1D, Figure 3.2B** middle). The fully reprogrammed neurons only expressed NeuN, but not GFAP, which was detected as early as ten days after the viral injection (**Figure 3.1E** yellow arrows). Three weeks after the viral injection, more than 50% of NeuroD1-mCherry positive (NeuroD1-mCherry+) cells expressed only NeuN but not GFAP (**Figure 3.1F** left). The exogenous NeuroD1 expression was significantly higher compared to the endogenous expression (**Figure 3.4**). The majority of NeuroD1-mCherry+ expressed excitatory neuronal marker Satb2, and a small percentage expressed GABAergic cell marker (**Figure 3.1F** right). Furthermore, we tested whether the reprogrammed neurons acquired cortical neuron identity and whether they formed layer structure by immunostaining a cortical neuronal marker Tbr1, a superficial layer marker Cux1, and a deep layer marker Ctip2. At both 3 and 6 weeks after the viral injection, more than 50% of NeuroD1-mCherry+ cells expressed Tbr1 (**Figure 3.3A-C**), indicating their cortical neuron identity. The NeuroD1-mCherry+ cells within the superficial and deep layers were immunopositive for Cux1 and Ctip2, respectively. The percentage of Cux1+/NeuroD1+ cells was higher in the superficial layers, lower in the deep layers, compared to Ctip2+/NeuroD1+ cells (**Figure 3.3D-I**). These results demonstrate that NeuroD1 efficiently converts astrocytes to neurons, which acquire cortical neuron identities and form cortical layer structure, allowing for functional circuit integration.

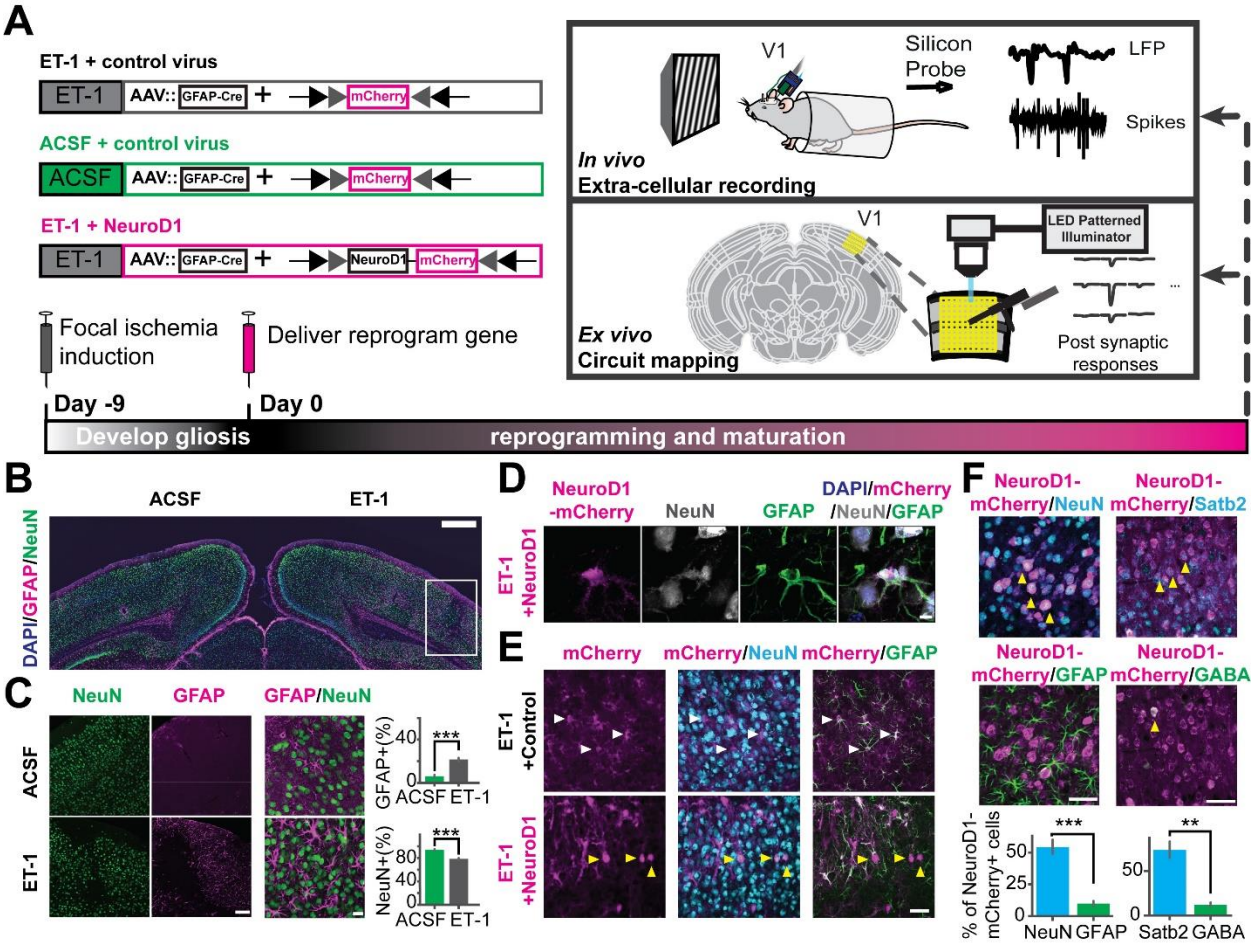

Figure 3.1. Focal ischemic injury model and *in vivo* direct reprogramming in the primary visual cortex. (A) The schedule to induce focal ischemia by endothelin-1 (ET-1) injection and to reprogram astrocytes into neurons by injection of AAV-GFAP::Cre with AAV-FLEX-NeuroD1-mCherry (or with AAV-FLEX-mCherry as control). Following reprogramming, visual responses and local circuit connectivity of the primary visual cortex (V1) were assessed by *in vivo* extracellular recordings and *ex vivo* Channelrhodopsin-Assisted Circuit Mapping (CRACM). (B) Gliosis (GFAP, magenta) and neuronal loss (NeuN, green) at 9 days after 4 ug/ul ET-1 injection in the visual cortex. The box indicates injury site with gliosis and neuronal loss. Scale: 500 μm. (C) Localized neuronal loss and gliosis at 9 days after 4ug/ul ET-1 injection. $Scale_{left}$: 50 μm. $Scale_{right}$: 20 μm. Right: Quantification of the percentages of GFAP-positive cells (top) and NeuN-positive cells (bottom). $N_{ACSF} = N_{ET-1} = 3$ mice, 9 slices. $p = 4.12 \times 10^{-4}$, Mann-Whitney U test. (D) An example of NeuroD1-mCherry-positive cell undergoing a transition stage at 10 days after NeuroD1 delivery, expressing both GFAP and NeuN. Scale: 5 μm. (E) mCherry positive cells co-stained with NeuN and GFAP at 10 days after viral injection. White arrows pointing to GFAP positive and NeuN negative cells. Yellow arrows pointing to GFAP negative and NeuN positive cells. Scale: 50 μm. (F) NeuroD1-positive cells stained with NeuN, GFAP, Satb2, and GABA at 3 weeks after NeuroD1 delivery. Scale: 50 μm. Bottom: Quantification of the ratios of marker positive cells. $N_{NeuN/GFAP} = 3$ mice, 9 slices. $p = 9.01 \times 10^{-4}$, Mann-Whitney *U*-test. $N_{Satb2/GABA} = 2$ mice, 6 slices. $p = 5.08 \times 10^{-3}$, Mann-Whitney *U*-test. $^{**}p < 0.01$ and $^{***}p < 0.001$. Data are represented as mean ± SEM.

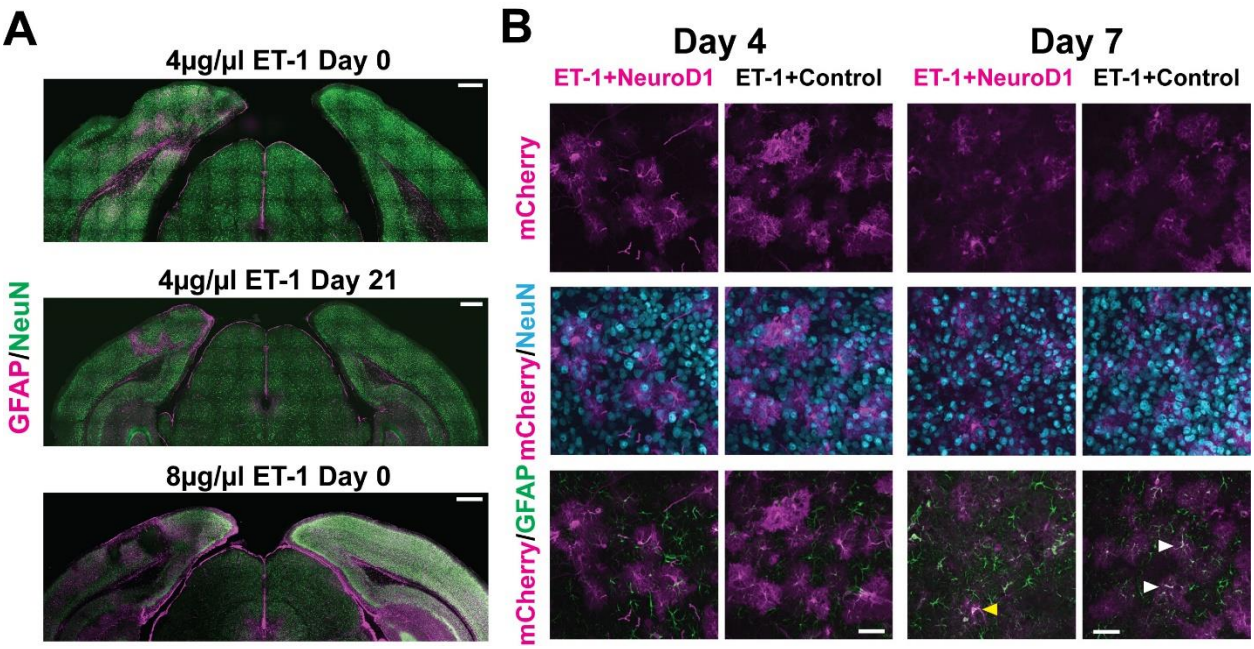

Figure 3.2. Gliosis and neuronal loss in ET-1 injected visual cortex and cell conversion following *in vivo* direct reprogramming in the primary visual cortex. (A) Gliosis (GFAP, magenta) and neuronal loss (NeuN, green) at 9 days after 4ug/ul ET-1 injection (top left hemisphere). Persisted gliosis after 4 weeks (middle left hemisphere). Larger tissue damage induced by 8ug/ul ET-1 (bottom left hemisphere). ACSF injected control (right hemispheres). Scale: 500µm. (B) mCherry positive cells co-stained with NeuN in the reprogrammed group and GFAP in control at 4 and 7 days after viral injection. Arrows pointing to double positive cells. Scale: 50µm.

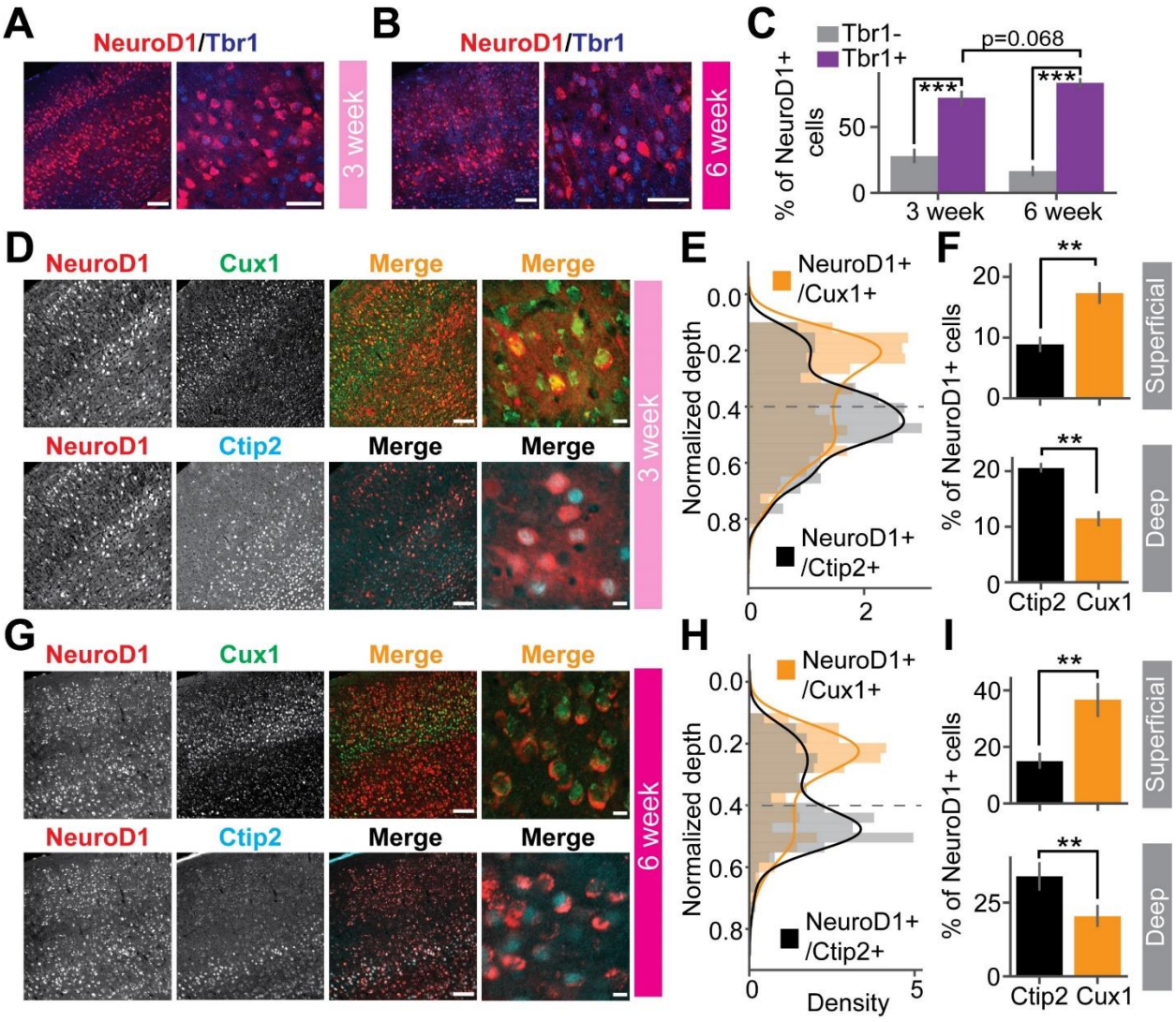

Figure 3.3. Reprogrammed cells acquire superficial and deep cortical layer identities. (A) NeuroD1 positive cells stained with cortical neuron marker Tbr1 at 3 weeks after the viral injection. $Scale_{left}$: 100 μm, $Scale_{right}$: 50 μm. (B) Same as (A) but at 6 weeks after the viral injection. $Scale_{left}$: 100 μm, $Scale_{right}$: 50 μm. (C) Quantification of Tbr1 positive cells out of NeuroD1 positive cells. Tbr1- vs. Tbr1+: $N_{3\ week}$ = 2 mice, 12 slices, $p = 1.23 \times 10^{-4}$; $N_{6\ week}$ = 4 mice, 23 slices, $p = 1.51 \times 10^{-8}$. 3 week vs. 6 week: $p = 0.068$. Mann-Whitney *U*-test with Bonferroni correction. (D) A representative slice showed that NeuroD1 positive cells co-stained with superficial layer marker Cux1 (top row), deep-layer marker Ctip2 (bottom row) at 3 weeks after the viral injection. The NeuroD1 image at the top and bottom row is the same. $Scale_{left}$: 100 μm, $Scale_{right}$: 10 μm. (E) Probability density of counts of NeuroD1+/Cux1+ cells and NeuroD1+/Ctip2+ cells across normalized cortical depths at 3 weeks after the viral injection. 0 indicates the brain surface. The dashed line indicates superficial and deep layer separation. (F) Percentages of Cux1+/NeuroD1+ and Ctip2+/NeuroD1+ cells in the superficial layers (top) and the deep layers (bottom) at 3 weeks after the viral injection. $N_{superficial}$ = 2 mice, 4 slices, $p = 3.06 \times 10^{-3}$. N_{deep} = 2 mice, 4 slices, $p = 2.54 \times 10^{-3}$. Mann-Whitney *U*-test with Bonferroni correction. (G) Same as (D) but at 6 weeks after the viral injection. (H) Same as (E) but at 6 weeks after the viral injection. (I) Same as (F) but at 6 weeks after the viral injection. $N_{superficial}$ = 3 mice, 7 slices, $p = 3.06 \times 10^{-3}$. N_{deep} = 3 mice, 7 slices, $p = 2.33 \times 10^{-3}$. Mann-Whitney *U*-test with Bonferroni correction. $^{**}p < 0.05$ and $^{***}p < 0.001$. Data are represented as mean ± SEM.

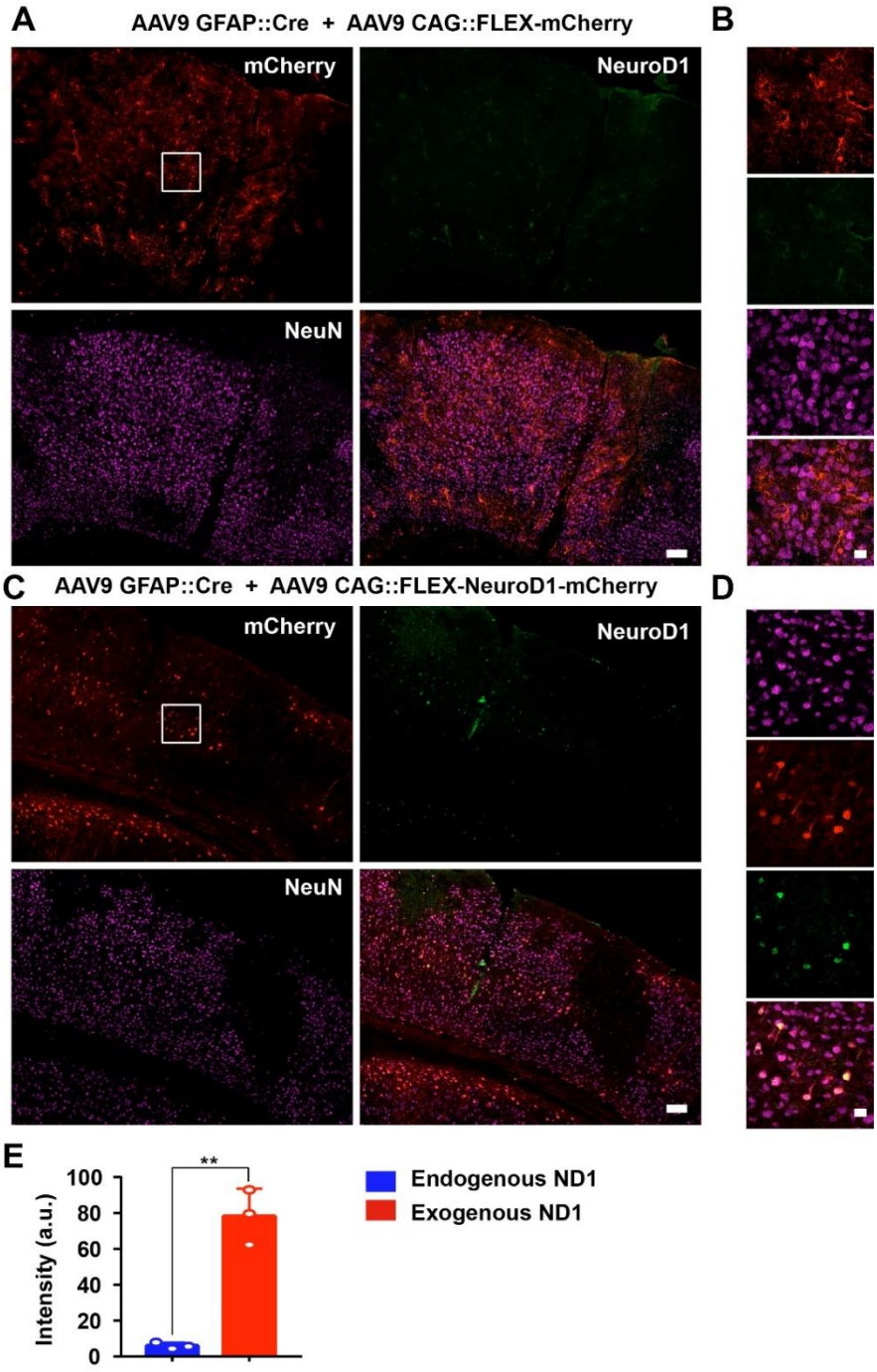

Figure 3.4. Comparison of endogenous NeuroD1 expression level versus AAV overexpressed NeuroD1 after astrocyte-to-neuron conversion. (A-B) Representative images illustrating that in the control mCherry group, the endogenous neurons (labeled by NeuN) rarely showed detectable level of NeuroD1 expression in the mouse cortex. Scale bar for panel A, 100 mm. Panel B shows the enlarged box area in panel A. Scale bar for panel B, 20 mm. (C-D) Representative images showing that in the NeuroD1 group, after astrocyte-to-neuron conversion (30 days post AAV NeuroD1 infection), NeuroD1 immunostaining (green) detected clear NeuroD1 signal in the NeuroD1-mCherry-converted neurons (red). Scale bar for panel C, 100 mm. Panel D shows the enlarged box area in panel C. Scale bar for panel D, 20 mm. (E) Quantitative analysis showing that the exogenous NeuroD1 expression level in NeuroD1-mCherry-converted neurons was significantly higher than the endogenous NeuroD1 expression level. **P < 0.01, Student's t-test (n = 3 animals for each group).

3.5.2 *In vivo* direct reprogramming recovered visually evoked potentials (VEPs) and single-unit responses

To assess functional recovery of V1 after reprogramming, we recorded visually evoked potentials (VEPs) and single-unit spikes in awake head-fixed mice using extracellular recording technique. Mice were separated into two groups (**Figure 3.5A**). In one group, ET-1 ischemia was induced in both hemispheres, followed by reprogramming (FLEX-NeuroD1-mCherry) in one hemisphere and the other hemisphere injected with a control virus (FLEX-mCherry) ("ET-1+NeuroD1 vs. ET-1+Control"). In the other group, ischemia was induced in only one hemisphere followed by reprogramming (FLEX-NeuroD1-mCherry), and the other hemisphere was sham-injected (ACSF) and treated with the control virus ("ET-1+NeuroD1 vs. ACSF+Control"). Mice were habituated to the head-fixation setup prior to experiments. Three weeks after viral injections, visual response to sinusoidal drifting gratings was recorded with a silicon probe (recording site validated with histology, **Figure 3.5B, C**). VEPs were compared between the two hemispheres within the same mouse to control for individual variability across animals. To validate visual function impairment by ET-1 induced ischemia, we added a group of mice, which were given only ET-1/ACSF injection. VEP amplitudes were significantly smaller in the ET-1 injected hemispheres compared to the ACSF injected hemispheres (**Figure 3.5D**). Next, we tested "ET-1+NeuroD1 vs. ET-1+Control" mice. VEP amplitudes were significantly larger in the ET-1+NeuroD1 hemispheres than the ET-1+Control hemispheres (**Figure 3.5E**). In contrast, for the "ET-1+NeuroD1 vs. ACSF+Control" group, VEP amplitudes were not significantly different between the two hemispheres (**Figure 3.5F**). In addition to the synchronized population activity, we also examined the single unit visual responses. Considering the heterogeneity of cortical neurons, we split the units into putative regular-spiking (RS) and fast-spiking (FS) units, based on trough-to-peak latencies and waveform latencies of their averaged template waveforms (**Figure 3.5G**). Based on both intracellular and extracellular studies, excitatory pyramidal neurons show regular-spiking waveforms, while inhibitory interneurons show fast-spiking waveforms (Connors and Gutnick, 1990; Henze et al., 2000; Trainito et al., 2019). To account for different baseline activity across units, we calculated the z-scores of firing rate over time for each unit. Z-scores of the visually evoked responses of all recorded units are shown in heatmaps (**Figure 3.5H**). In the "ET-1+NeuroD1 vs. ET-1+Control" group, RS units in the ET-1+NeuroD1 hemispheres showed significantly higher peak firing rate z-scores compared to the ET-1+Control hemispheres (**Figure**

3.5I left). In the same group, FS units in the ET-1+NeuroD1 hemispheres showed similar peak firing rate z-scores compared to the ET-1+Control hemispheres (**Figure 3.5I** right). In the "ET-1+NeuroD1 vs. ACSF+Control" group, RS units in the ET-1+NeuroD1 hemispheres showed comparable peak firing rate z-scores to the ACSF+Control hemispheres (**Figure 3.5J** left). Interestingly, FS units in the ET-1+NeuroD1 hemispheres showed lower peak firing rate z-scores than the ACSF+Control hemispheres (**Figure 3.5J** right). These results demonstrate that ET-1 induced ischemia significantly impairs visual response in V1, and *in vivo* direct reprogramming restores the visual responses, to a comparable level as in the sham condition. The single-unit activity suggests that there may be a differential recovery of visual responses in RS and FS cells. At 3 weeks post-infection, RS cells have regained normal levels of visual responsiveness, while FS cells have not.

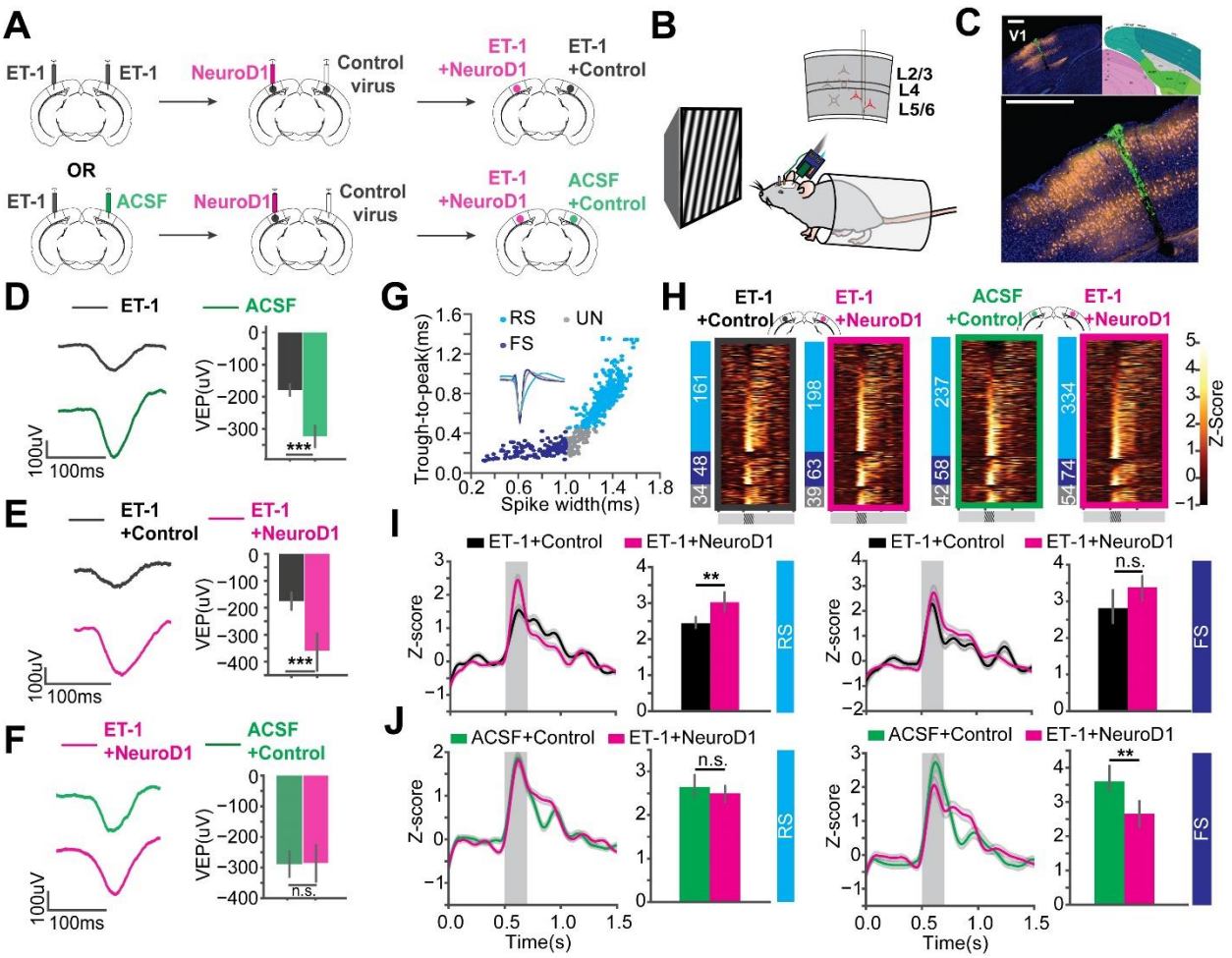

Figure 3.5. *In vivo* direct reprogramming recovers visually evoked potentials (VEPs) and single unit visual responses. (A) The injection scheme for *in vivo* experiments. (B) The *in vivo* awake extracellular recording setup. (C) Histology showing the probe track (green) within the reprogramming site. NeuroD1: orange, DAPI: blue. *The brain atlas is adapted from ©Allen Institute for Brain Science. Allen Adult Mouse Atlas. Available from: atlas.brain-map.org. Scale: 500 μm (top and botom). (D) Averaged VEPs of ET-1 and ACSF hemispheres. Quantification of VEP amplitudes on the right in each panel. $N_1 = N_2 = 27$ recording sites, 9 mice, $p = 3.07 \times 10^{-4}$, Mann-Whitney *U*-test. (E) Same as (D) but for ET-1+Control and ET-1+NeuroD1 hemispheres. $N_1 = N_2 = 33$ recording sites, 11 mice, $p = 1.30 \times 10^{-5}$, Mann-Whitney *U*-test. (F) Same as (D) but for ACSF+Control and ET-1+NeuroD1 hemispheres. $N_1 = N_2 = 30$ recording sites, 10 mice, $p = 0.559$, Mann-Whitney *U*-test. (G) Units classified into regular-spiking (RS), fast-spiking (FS), and unclassified (UN) units. Scatter plot showing trough-to-peak latency and waveform width of the units. The averaged template waveforms shown in the inset. (H) Firing rate z-scores of all units in heatmaps for "ET-1+Control vs. ET-1+NeuroD1" and "ACSF+Control vs. ET-1+NeuroD1" groups. The numbers of RS, FS, and UN units are shown on the left for each heatmap. (I) Left: Firing rate z-scores of RS units in the "ET-1+Control vs. ET-1+NeuroD1" group. The shaded area: visual stimulation. Bar graph showing peak z-scores within the visual stimulation window. $N_{ET-1+Control} = 161$ units, 11 mice, $N_{ET-1+NeuroD1} = 198$ units, 11 mice, $p = 1.56 \times 10^{-3}$, Mann-Whitney *U*-test. Right: Same as the left but for FS units. $N_{ET-1+Control} = 48$ units, 11 mice, $N_{ET-1+NeuroD1} = 63$ units, 11 mice, $p = 0.084$, Mann-Whitney *U*-test. (J) Left: Firing rate z-scores of RS units in the "ACSF+Control vs. ET-1+NeuroD1" group. The shaded area: visual stimulation. Bar graph showing peak z-scores within the visual stimulation window. $N_{ACSF+Control} = 237$ units, 10 mice, $N_{ET-1+NeuroD1} = 334$ units, 10 mice, $p = 0.238$, Mann-Whitney *U*-test. Right: Same as the left but for FS units. $N_{ACSF+Control} = 58$ units, 10 mice, $N_{ET-1+NeuroD1} = 74$ units, 10 mice, $p = 0.0058$, Mann-Whitney *U*-test. *$p < 0.05$, **$p < 0.01$, and ***$p < 0.001$, n.s., not significant. Data are represented as mean ± SEM.

At 6 weeks after delivery of NeuroD1, visual responses in the NeuroD1 treated mice showed continued improvement. In the "ET-1+Control vs. ET-1+NeuroD1" group, not only RS unit firing, but also FS unit firing was significantly higher in the ET-1+NeuroD1 hemispheres than the ET-1+Control hemispheres (**Figure 3.6F**). In the "ET-1+NeuroD1 vs. ACSF+Control" group, RS unit firing in the ET-1+NeuroD1 hemispheres was comparable to the ACSF+Control hemispheres (**Figure 3.6H**, left). Interestingly, unlike 3 weeks post-infection, FS unit firing was not significantly different from the ACSF+Control hemispheres (**Figure 3.6H**, right). This suggests that FS cells have delayed development compared to RS units.

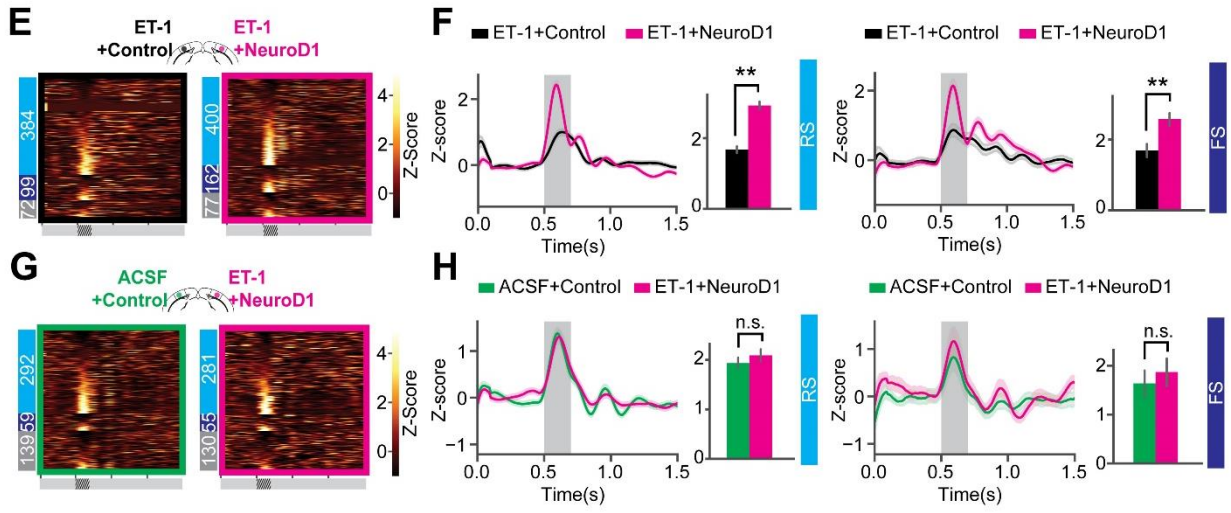

Figure 3.6. Correction of fast-spiking unit responses at 6 weeks after *in vivo* direct reprogramming. (E) Firing rate z-scores of all units in heatmaps for "ET-1+Control vs. ET-1+NeuroD1" group. The numbers of RS, FS, and UN units are shown on the left. (F) Firing rate z-scores of RS (left) and FS (right) units in the "ET-1+Control vs. ET-1+NeuroD1" group. RS units: $N_{ET-1+Control} = 384$ units, $N_{ET-1+NeuroD1} = 400$ units, $p = 4.09 \times 10^{-3}$. FS units: $N_{ET-1+Control} = 99$ units, $N_{ET-1+NeuroD1} = 162$ units, $p = 0.0065$. 14 recordings. Mann-Whitney *U*-test with Bonferroni correction. (G) Same as (E) but for "ACSF+Control vs. ET-1+NeuroD1" group. (H) Same as (F) but for the "ACSF+Control vs. ET-1+NeuroD1" group. The shaded area represents visual stimulation. Peak z-scores within the visual stimulation window were quantified. RS units: $N_{ACSF+Control} = 292$ units, $N_{ET-1+NeuroD1} = 281$ units, $p = 0.499$. FS units: $N_{ACSF+Control} = 59$ units, $N_{ET-1+NeuroD1} = 55$ units, $p = 0.540$. 9 recordings. Mann-Whitney *U*-test with Bonferroni correction. $^{**}p < 0.01$ and n.s., not significant. Data are represented as mean ± SEM.

3.5.3 Visually evoked response recovers in older adults as well

VEP amplitudes of the reprogrammed hemisphere were significantly larger compared to the untreated ischemia hemisphere in the "reprogrammed vs. untreated" mice (**Figure 3.7**C, $n_1=n_2=45$ recording sites, 7 mice, $p < 0.0001$, CL effect size= 0.801, Mann-Whitney U test). VEP amplitudes of the reprogrammed hemisphere were comparable to the sham control hemisphere in the "reprogrammed vs. sham" mice ($n_1=n_2=39$ recording sites, 7 mice, p= 0.201, CL effect size= 0.584, Mann-Whitney U test). Visually evoked firing of RS units from the reprogrammed hemisphere was marginally higher than the untreated ischemia hemisphere (**Figure 3.7**D, $n_{reprogrammed}$= 68 units, $n_{untreated\ ischemia}$= 49 units, p= 0.113, CL effect size= 0.586, Mann-Whitney U test). However, FS units had much higher visually evoked firing in the reprogrammed hemisphere than the untreated ischemia hemisphere ($n_{reprogrammed}$= 36 units, n_{sham}= 35 units, p= 0.015, CL effect size= 0.669, Mann-Whitney U test). In the "reprogrammed vs. sham" group, both RS and FS units showed comparable evoked firing in both hemispheres (RS: $n_{reprogrammed}$= 53 units, n_{sham}= 65 units, p= 0.417, effect size= 0.544, FS: $n_{reprogrammed}$= 12 units, n_{sham}= 17 units, p= 0.912, effect size= 0.515, Mann-Whitney U test). The results here showed that *in vivo* reprogramming is equally effective in older adults in recovering visual responses after ischemic injury.

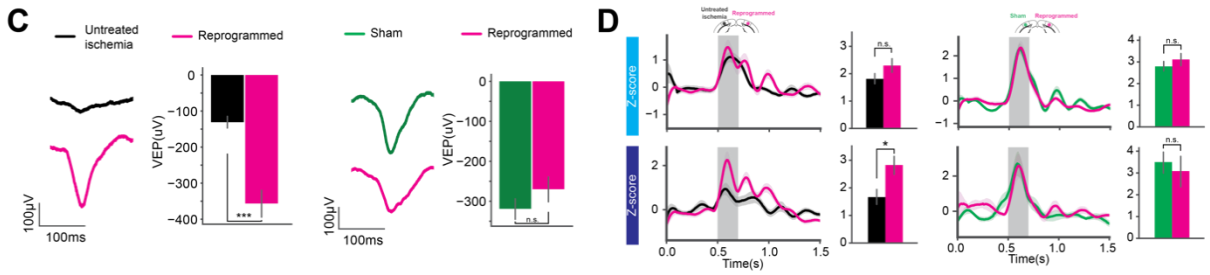

Figure 3.7. Circuit repair and visual function restoration through *in vivo* direct reprogramming after ischemic injury was consistent in adult mice. (C) Averaged VEPs of the reprogrammed and the untreated ischemia hemispheres were shown. Peak amplitudes were compared. Averaged VEPs of the reprogrammed and the sham hemispheres. Peak amplitudes were compared. (D) Firing rate z-scores of RS and FS units in the reprogrammed hemispheres were compared to the untreated ischemia hemispheres, and to the sham hemispheres. Peak z-scores were compared. Mann-Whitney U test. *-p<0.05, ***-p<0.001. Error bar indicates mean ± SEM.

3.5.4 Orientation selectivity of the local neuronal population was sharpened over time

Following postnatal development and visual experience, most V1 neurons acquire preference to a specific orientation (Li et al., 2008; Nauhaus et al., 2008; Ko et al., 2011). To further assess functional recovery following reprogramming, we examined neuronal unit activity in response to sinusoidal gratings of 6 orientations (**Figure 3.8A**). Representative units and population firing rate z-scores to different orientations revealed selective responses of most units in each group (**Figure 3.8A, B**). To quantify population selectivity to orientations, we averaged firing rate across units to 6 orientations and fitted Gaussian functions for each group to estimate "population tuning curves." Three weeks (3wk) post-infection, in the "ET-1+NeuroD1 vs. ET-1+Control" group, tuning curve width (variance (σ) of the fitted function) was 20.957 degrees for the ET-1+NeuroD1 hemisphere, only slightly sharper than 21.322 degrees for the ET-1+Control hemisphere (**Figure 3.8C**, top). At the same time, in the "ET-1+NeuroD1 vs. ACSF+Control" group, the ET-1+NeuroD1 hemisphere tuning curve width was 20.387 degrees, broader than 17.995 degrees of the ACSF+Control hemisphere (**Figure 3.8E** top). However, six weeks (6wk) post-infection, in the "ET-1+NeuroD1 vs. ET-1+Control" group, the tuning curve width was 17.504 degrees for the ET-1+NeuroD1 hemisphere, sharper than 22.880 degrees for the ET-1+Control hemisphere (**Figure 3.8C**, bottom). In the "ET-1+NeuroD1 vs. ACSF+Control" group, the ET-1+NeuroD1 hemisphere tuning curve width was 18.228 degrees, comparable to 17.885 degrees for the ACSF+Control group (**Figure 3.8E**, bottom). To quantitatively compare orientation selectivity distributions between groups, we calculated the orientation selectivity index (one minus the circular variance of firing rates to 6 orientations, 1-CV) for each unit (**Figure 3.8D, F**, see method for details). In the "ET-1+NeuroD1 vs. ET-1+Control" group, the cumulative distribution of 1-CV of the ET-1+NeuroD1 hemisphere showed no difference compared to the ET-1+Control hemisphere at three weeks, and marginal difference at six weeks post-infection. While in the "ET-1+NeuroD1 vs. ACSF+Control" group, the cumulative distribution of 1-CV of the ET-1+NeuroD1 hemisphere was left-shifted compared to the ACSF+Control hemisphere at three weeks but was not different at six weeks post-infection. These results revealed that the orientation tuning of the cortical population was not completely recovered three weeks post-reprogramming but was comparable to the sham condition six weeks post-reprogramming. However, the orientation selectivity of the NeuroD1 group could be the result of either improvement in the reprogrammed neurons or pre-existing neurons, or both. To answer this question, we used

optotagging to examine orientation selectivity of the reprogrammed neurons by injecting AAV-DIO-ChR2-eYFP together with AAV-GFAP::Cre and AAV-FLEX-NeuroD1-mCherry (**Figure 3.9A**). We identified 22 cells that reliably responded both to optogenetic and visual stimulation and found most of them were selective to orientations (**Figure 3.9A-H**). Both *in vivo* 2-photon calcium imaging at two developmental times and optotagging results suggest that the reprogrammed cells acquire orientation- and direction-selective responses over time and indicate their functional integration into the local visual cortical circuits.

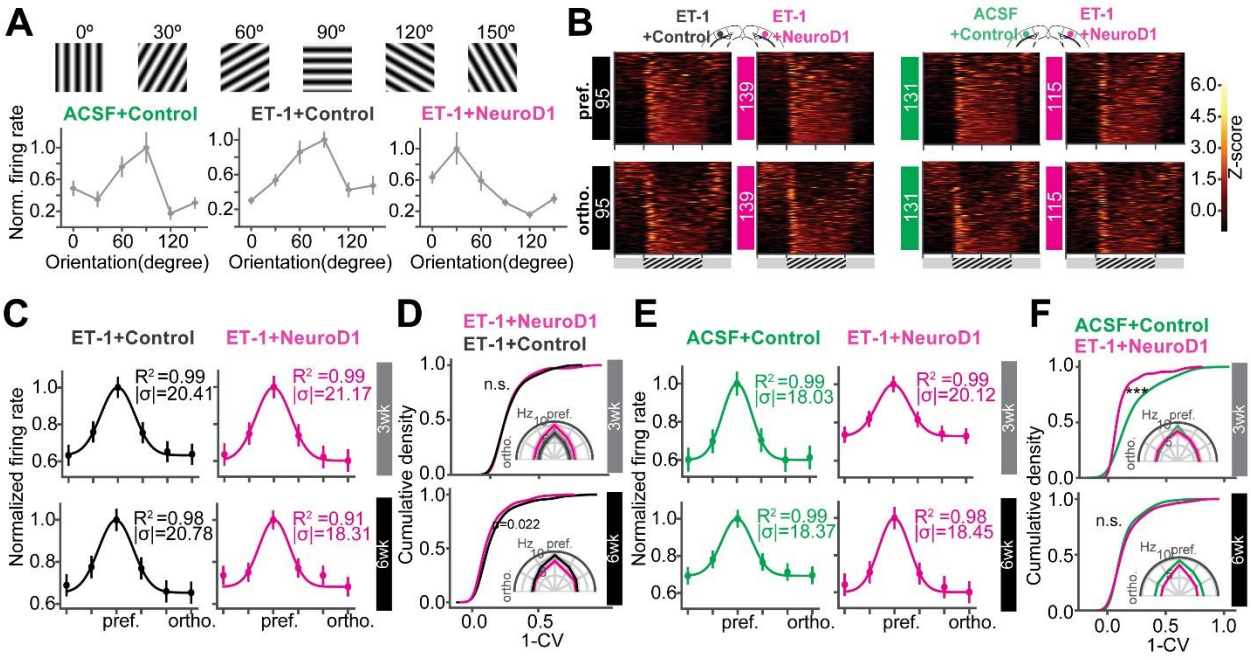

Figure 3.8. Orientation selectivity of the local neuronal population is improved over time. (A) Gratings of 6 orientations used to measure orientation selectivity. Bottom: normalized firing rate of representative units for each group. (B) Heatmaps of firing rate z-scores of all units in response to the preferred (pref., top) and the orthogonal (ortho., bottom) orientations for each group. (C) The curves showing unit averaged firing rates to 6 orientations normalized and fitted with Gaussian functions of the "ET-1+NeuroD1 vs. ET-1+Control" group at 3 weeks and 6 weeks post-infection. The insets showing the coefficient of determination (R^2) and sigma of fitted functions. (D) Cumulative distributions of 1-CV of units in panel (C). Inset, unit averaged firing rates to 6 orientations. 3 weeks: $N_{ET-1+Control}$ = 95 units, $N_{ET-1+NeuroD1}$ = 139 units, from 6 mice, p = 0.954; 6 weeks: $N_{ET-1+Control}$ = 93 units, $N_{ET-1+NeuroD1}$ = 142 units, from 4 mice, p = 0.022. 2-sample Kolmogorov-Smirnov test. (E) Same as (C) but for "ET-1+NeuroD1 vs. ACSF+Control" group. (F) Same as (D) but for "ET-1+NeuroD1 vs. ACSF+Control" group. 3 week: $N_{ACSF+Control}$ = 131 units, $N_{ET-1+NeuroD1}$ = 115 units, from 4 mice, $p = 1.659 \times 10^{-7}$; 6 week: $N_{ACSF+Control}$ = 183 units, $N_{ET-1+NeuroD1}$ = 172 units, from 8 mice, p = 0.652, 2 sample Kolmogorov-Smirnov test. ***$p < 0.001$ and n.s., not significant. Data are represented as mean ± SEM. See also Supplementary Figure 5.

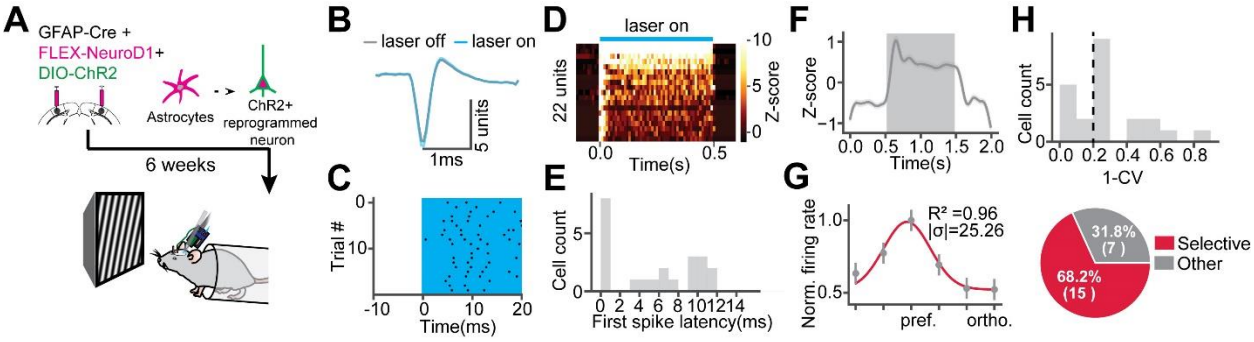

Figure 3.9. Optogenetically tagged reprogrammed cells are visually responsive and orientation selective. (A) AAV-DIO-ChR2 was injected together with AAV-GFAP::Cre and AAV-FLEX-NeuroD1 to express ChR2 in the reprogrammed cells. 6 weeks after reprogramming, visual cortical activities were measured by extracellular recordings with optogenetic stimulation. (B) Mean template waveforms of a representative unit during laser off and laser on. (C) Raster plot of the cell in (B) during optogenetic stimulation. The cyan shade indicates optogenetic stimulation. (D) Firing rate z-scores of units in response to optogenetic stimulation. 22 units that have first spike latencies shorter than 15ms and mean firing rate z-scores within the optogenetic time window are defined as optotagged units. (E) The distribution of first spike latencies of units in (D). (F) Average firing rate z-scores of optotagged units in response to visual stimulation. The shaded area represents visual stimulus time window. (G) Average firing rates of optotagged units in response to 6 orientations are normalized and fitted with a Gaussian function. The inset showing the coefficient of determination (R^2) and sigma of fitted functions. Data are represented as mean ± SEM.

3.6 Discussion

3.6.1 Characterization of neuronal circuit functions is a critical assessment of the therapy

We demonstrated that NeuroD1-mediated *in vivo* direct reprogramming of astrocytes into neurons promoted their neural circuit integration and led to the visual functional recovery after ischemic injury. Our work bridged the knowledge gap between individual cellular response recovery and animal behavioral recovery, where we characterized the functional synapses formed from specific projections and assessed neuronal response to stimuli in awake mice, which are critical functional characterization at the intermediate neural circuit level. The mouse primary visual cortex is a unique model system providing an opportunity to quantify projection specific functional connectivity and the direct visual responsiveness of the reprogrammed cells. Furthermore, the ability to record responses to different visual features such as orientation and direction provides a unique ability to quantify how well the cells mature and whether the synapses they receive are functional.

3.6.2 Visual response recovers and selectivity to orientations sharpens following the therapy

In our model system, the visual responses were drastically reduced following ischemic injury, yet they recovered following the NeuroD1 delivery. The putative excitatory neurons started to regain their visual responses three weeks after reprogramming, while the putative inhibitory neurons progressively integrated circuit inputs and refined their activity over a longer period. This delayed recovery of inhibition after reprogramming is similar to the absence of matured inhibition at an early age during postnatal V1 development (Minlebaev et al., 2011; Shen and Colonnese, 2016). Furthermore, these visual responses became more specific with time, based on our two-photon calcium imaging and extracellular recording results. The NeuroD1 converted cells gradually developed to be selective to the orientations and directions of visual stimuli, which is a typical feature of the mature visual cortical neurons. Interestingly, the reprogrammed cells at 6 weeks post-infection demonstrated higher selectivity compared to the healthy controls, which could be potentially explained by the more functionally developed synaptic inputs received by the reprogrammed cells compared to the healthy controls.

3.6.3 Visual experience might play a role in activity refinement following the therapy

Visual experience in the housing cages may have led to the pruning of excess synapses, activity refinement, and cell maturation. Slower development of inhibitory responses is consistent with the delayed maturation of inhibition following visual experience in the normal developing cortex. Improved orientation selectivity of the reprogrammed neurons with additional time and visual experience may result from their integration into the local circuits and maturation of the local inhibition (Liu et al., 2011).

In our work, the demonstration of visual response and selectivity recovery provides a novel cellular and circuit characterization consistent with the previous work (Chen et al., 2020). CRACM experiments provided the quantification of the functional synaptic connectivity recovery extending the prior report of non-specific spontaneous synaptic currents developing in reprogrammed cells (Guo et al., 2014; Chen et al., 2020). We discovered, for the first time to our knowledge, that the functional maturation of the reprogrammed neurons shares similarities with the typical postnatal cortical circuit development. This finding suggests the importance of experience in the development of the reprogrammed cells and functional brain recovery after injury.

3.6.4 Conversion efficiency and functional recovery are similar to other therapies

Compared to other studies, the functional recovery achieved by NeuroD1-mediated astrocyte-to-neuron conversion *in vivo* was similarly efficient. The reprogrammed neurons in the visual cortex acquired the cortical layer structure, similarly to Ngn2- and Nurr1-mediated reprogramming (Mattugini et al., 2019). The local functional circuit and visual response recovery were also similar to embryonic neuronal transplantation results (Falkner et al., 2016). However, other methods such as cell transplantation may have side effects, such as immune response, which limit their therapeutic potential. Direct *in vivo* conversion of astrocytes into neurons removes the possibility of graft rejection and provides a viable solution for this problem.

Our findings suggest that the NeuroD1-based *in vivo* direct reprogramming technology may be a promising gene therapy treatment of brain injury by replenishing the lost neurons and successfully integrating them into the existing neural circuit.

3.7 Contribution statement

QW, YT, MG, GC, and AC designed the experiments. ZP produced the viruses. YT (>80%), QW, YC, AR, ZX, TW, and WL performed the IHC experiments. YT (80%) and SK performed the extracellular recordings. QW performed the CRACM experiments. MG performed 2 photon calcium imaging. YT (>60%), QW, and ER performed the injections. YT (>50%), QW, MG, ZX, TW, and WL analyzed the data and drafted the manuscript. YT, QW, MG, GC, and AC edited and revised the manuscript. All authors contributed to the article and approved the submitted version.

3.8 Acknowledgement

We thank the Chubykin lab members for discussions during the development of the project. We thank Renee C. Tower for help with brain slicing for the optogenetics experiment. We thank our collaborator Dr. Gong Chen's team for assisting on some IHC experiments. We also thank Dr. Sotiris Masmanidis for providing silicon probes. We are grateful for financial support from the NIMH grant RF1 MH123401 to AC and Charles H. Smith Endowment Fund to GC.

CHAPTER 4. FUNCTIONAL CHARACTERIZATION OF VISUAL CORTICAL IMPAIRMENT IN AUXILIN KNOCKOUT MICE

4.1 Introduction

Synaptic transmission and plasticity play critical roles in neuronal circuit functions, such as sensory information processing and learning. These functions are supported by synaptic co-chaperone activities. Alternations in one synaptic co-chaperone protein, Auxilin, has been shown associated with early onset of Parkinsonism (Olgiati et al., 2016). Auxilin is involved in vesicle endocytosis and recycling (Yim et al., 2010; Gorenberg and Chandra, 2017), a crucial process to replenish the readily releasing pool of vesicles especially in the case of high frequency firing. Evidence has shown that cortical neurons showed deficits in synaptic ultrastructure in vitro in Auxilin knockout (Aux-KO) mice, but it remains unclear whether cortical functions are affected by altered synaptic transmission or plasticity. To address the question, we investigated cortical circuit functions in Auxilin knockout (Aux-KO) mice using in vivo extracellular recordings and found a wide spectrum of visual cortical dysfunctions including reduced orientation selectivity, lack of visual adaptation and mismatch responses, along with delayed and reduced oscillatory responses of the unit population.

4.2 Material and methods

4.2.1 Animals

Male and female mice (transgenic, C57BL/6, from Dr. Sreeganga Chandra) at the age of 3.5-5 months were used for experiments. Mice were housed in 12-hour light/dark cycle with full access to water and chow food. All animal use were approved by Purdue IACUC and followed NIH guidelines.

4.2.2 Headpost implantation surgery

The mouse was first anesthetized using 5% isoflurane in oxygen or in room air (SomnoSuite system) in an induction chamber. After deep anesthesia was confirmed (no reflex after a foot pinch), the mouse was transferred to a stereotaxic frame (Kopf or NeuroStar) and

maintained anesthetized using 1.5-2% isoflurane delivered through a nose cone while the body temperature was monitored and kept at 37°C. Eye ointment was applied to prevent dryness. The skin over the mouse skull was removed using sterile scissors, and 3% hydrogen peroxide was applied to the skull to remove connective tissues. V1 was labeled using a permanent marker using stereotaxic coordinates (relative to lambda: V1: ±3.0 mm lateral, 0.8 mm anterior). A nail (headpost) was adhered to the mouse skull using superglue at 0.7 mm anterior to the bregma, and a gold-plated reference pin (WPI 5482) was inserted through the skull and above brain surface (0.5 mm anterior to the bregma). The skull, the reference pin, and the headpost were covered with Metabond (Parkell S380) in the end. Mice were allowed for 3 days to recover before experiments.

4.2.3 Head-fixation setup and visual stimulation

After the mice recovered from the surgeries, we let the mice habituate to the head-fixation setup first. During the habituation, the mouse was head-fixed by the headpost, and was loosely restrained by a customized tube. A visual stimulation monitor was placed at 17 cm in front of the mouse. While the mouse was head-fixed, a gray screen was shown to the mouse for 1.5 hours per day for at least 4 days before electrophysiology recordings. Extracellular recordings were taken after mice habituated to the setup.

For the visual adaptation and mismatch negativity experiment, two static gratings (50% contrast, 15) of 90-degree difference in their orientations were used as either deviant or redundant stimuli. In 300 presentations of visual stimuli, the deviant stimulus was presented in 10% of trials (with linearly increased appearance probability in the sequence), and the redundant stimulus was presented in the other 90% trials. To counterbalance potential preferences for the two stimuli, two sequences were presented, with one sequence using 45° as the redundant stimulus and the other sequence using 135° as the redundant stimulus. An additional control sequence with equal appearance probability was presented at the beginning of the recording, where static gratings in six orientations (including the two selected for measurements of visual adaptation and mismatch negativity) were pseudorandomly presented, with 50 presentations for each stimulus. In all sequences, each stimulus was presented for 0.5 s, separated by the 1.2-1.8 s intervals in between presentations.

For the visual perceptual experience, drifting gratings (oriented 30 degrees from the vertical direction, 0.04 cycles/degree, 2 Hz) were presented to the mouse for 200 trials per day for

four days. Extracellular activities in V1 were taken before and after the visual perceptual experience when the same stimulus was presented for 20 trials.

4.2.4 Extracellular recording preparation

After habituation or visual experience, extracellular activities in V1 were recorded using a 64-channel silicon probe (Shobe et al., 2015) in head-fixed mice. The skull over the pre-labeled V1 position was removed when the mouse was anesthetized on the stereotaxic frame, and then the mouse was transferred to the head-fixation setup. The probe was first positioned above the craniotomy and then was inserted into the brain perpendicularly to the brain surface using a Scientifica manipulator. Sterile artificial cerebrospinal fluid (ACSF) was added on top of the brain surface before recordings. Thirty minutes after probe insertions, data acquisition started.

4.2.5 Data acquisition and analysis

Data are acquired at 30 kHz, with Intan headstages, and OpenEphys (Siegle et al., 2017) acquisition system. Each trial recording was triggered using a TTL signal. Raw data were 300 Hz low pass filtered for LFP analysis, and were band-pass filtered between 300-6000 Hz for spike clustering using Kilosort. Clusters were manually inspected in Phy to remove noisy units. LFP and clustered spike data were then analyzed using Python.

For LFP analysis, the LFP with the largest amplitude within 50-150 ms post- visual stimulation onset between 300 to 500 μm below the brain surface was identified as the layer 4 LFP for each channel column within each recording. For single unit analyses, trial averaged firing rates (FR) was first calculated using gaussian kernel (5 ms as one standard deviation) smoothed spike histogram for each unit, then the z-scores of the unit firing rates over time were calculated.

Statistical tests were performed using statistical packages including SciPy, Pingouin (Vallat, 2018a). Data normality was tested using Shapiro-Wilk test first. For normally distributed data, student's t tests were used. For non-normally distributed data, Mann–Whitney U tests or Kolmogorov–Smirnov 2 sample tests were used. P values of multiple comparisons were corrected using FDR-BH method.

4.3 Results

To investigate whether visual cortical functions were impaired in Auxilin-KO mice, we recorded extracellular activities in awake mouse V1 using a silicon probe (**Figure 4.1**A), in responses to a battery of visual stimulation paradigms. One of the most prominent functional features of neurons in mouse V1 is their selective responses to orientation or directions, so we first assessed the orientation selectivity of single unit responses, by presenting static gratings in six orientations (**Figure 4.1**B top). Both Aux-KO and WT mice showed visually evoked responses when we looked at the unit population averaged firing rates, but the Aux-KO mice showed smaller responses to most orientations, compared to WT (**Figure 4.1**B bottom). Then, we looked at the distributions of units' preferred orientations, and found that units' preferred orientations were uniformly distributed across six orientations in both groups (**Figure 4.1**C). Considering the differences in orientation preferences, we defined the preferred orientation for each unit as the orientation at which it showed largest visually evoked firing rate, and defined the other orientations as how far they were away from the preferred orientation. We then quantified units' visually-locked firing rates in relation to their preferred orientations and others, and found that the visually-locked firing rate in response to the preferred orientation were significantly smaller in Aux-KO mice, compared to WT (**Figure 4.1**D, Orientation -2: p=0.560, common language effect size (CLES)=0.525, Orientation -1: p=0.376, CLES=0.541, Orientation 0: p=0.008, CLES=0.573, Orientation 1: p=0.560, CLES=0.530, Orientation 2: p=0.560, CLES=0.526, Orientation 3: p=0.391, CLES=0.538, Mann–Whitney U test with FDR-BH correction). Furthermore, when we compared the cumulative density of units' orientation selectivity indices (1-circular variance, 1-CV), we found that the units in Aux-KO mice showed lower selectivity indices compared to WT (**Figure 4.1**E, p=0.026, statistic=0.115, Kolmogorov–Smirnov 2 sample test). This result demonstrated that orientation selectivity was impaired in Aux-KO V1.

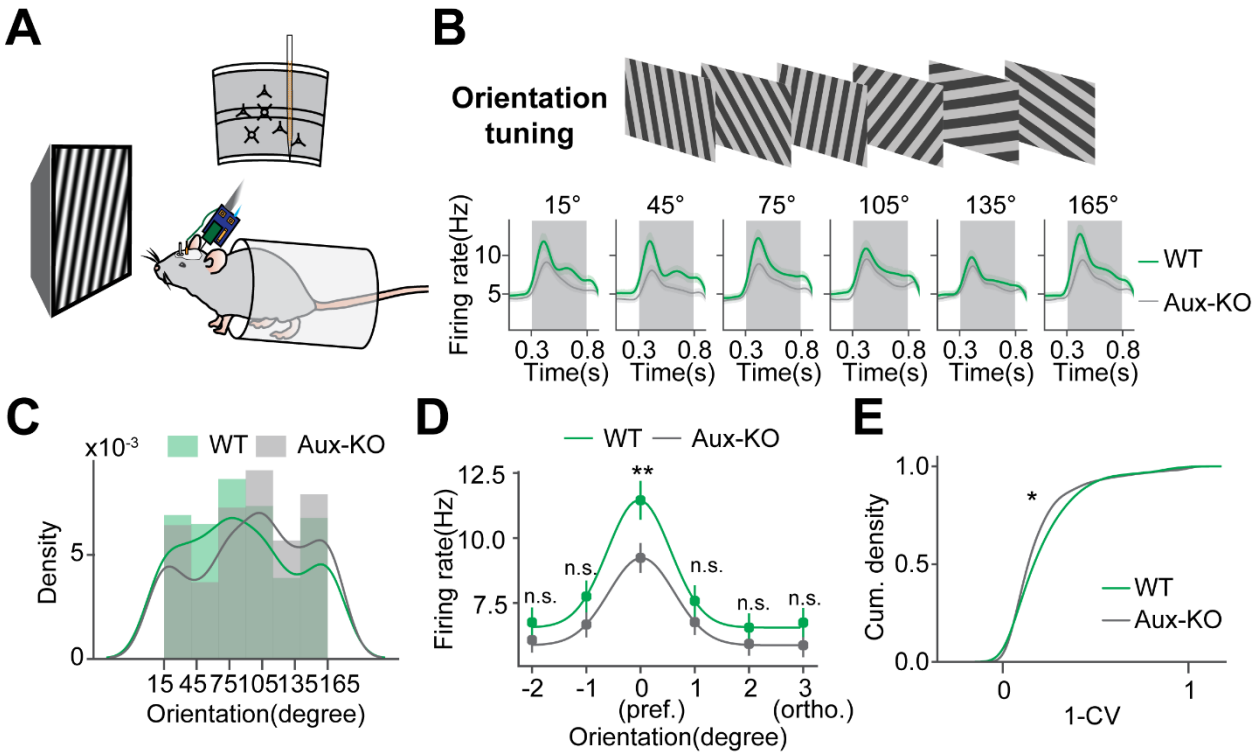

Figure 4.1. Visually evoked firing rates and orientation selectivity were reduced in Auxilin KO mice. (A) In vivo extracellular recording of V1 activities were performed in head-fixed mice using 64 channel silicon probes spanning the whole cortical depths. Visual stimulation was presented in the front. (B) Static gratings at six orientations were presented to the mice. Unit population averaged firing rates in response to six orientations were shown below. The gray shaded area represented visual stimulation time window. (C) Density plot of unit preferred orientations. (D) Unit population averaged firing rates in response to their preferred orientations and others. WT: N=276 units, 7 mice; Aux-KO: N=375 units, 10 mice. Mann–Whitney U test with FDR-BH correction. (E) Cumulative density plot of orientation selectivity indices (1-CV). Kolmogorov–Smirnov 2 sample test. Data were presented as mean ± SEM. *-p<0.05, **-p<0.01, ***-p<0.001, n.s.-not significant.

Next, we investigated sensory adaptation and visual mismatch responses using an oddball paradigm (Pak et al., 2021). In this paradigm, two orientations (45° and 135°) were presented in one sequence, where one orientation was presented in 10% of trials as the deviant stimulus, and the other was presented in 90% of trials as the redundant stimulus. To counterbalance potential preferences for the two stimuli, two sequences were presented, with one sequence using 45° as the redundant stimulus and the other sequence using 135° as the redundant stimulus. Units' firing rates in the oddball sequence were compared to those in the orientation tuning sequence, where the two stimuli were presented with equal appearance probability (**Figure 4.2**A). We first separated units based on their orientation preferences using their responses in the orientation tuning sequence. In WT mice, the units that preferred the deviant orientation showed significantly greater firing rates in response to the deviant stimulus, compared to the redundant stimulus (**Figure 4.2**B, WT: Ctr. vs. Dev.: p=0.480, CLES=0.458, Ctr. vs. Red.: p=0.009, CLES=0.658, Dev. vs. Red.: p=0.003, CLES=0.693; Aux-KO: Ctr. vs. Dev.: p=0.487, CLES=0.531, Ctr. vs. Red.: p=0.140, CLES=0.588, Dev. vs. Red.: p=0.487, CLES=0.542, Mann–Whitney U test with FDR-BH correction). At the same time, they showed significantly smaller firing rates in response to the redundant stimulus, compared to the control stimulus. Interestingly, neither the difference between the deviant stimulus and the redundant stimulus nor the difference between the redundant stimulus and the control stimulus were present in Aux-KO mice. The units that preferred the redundant orientation or other orientations showed comparable firing rates in response to the deviant, redundant, and control stimuli (**Figure 4.2**C,D, Redundant preferring units: WT: Ctr. vs. Dev.: p=0.102, CLES=0.594, Ctr. vs. Red.: p=0.689, CLES=0.479, Dev. vs. Red.: p=0.102, CLES=0.404; Aux-KO: Ctr. vs. Dev.: p=0.667, CLES=0.549, Ctr. vs. Red.: p=0.667, CLES=0.519, Dev. vs. Red.: p=0.667, CLES=0.467; Other preferring units: WT: Ctr. vs. Dev.: p=0.940, CLES=0.502, Ctr. vs. Red.: p=0.476, CLES=0.532, Dev. vs. Red.: p=0.476, CLES=0.529; Aux-KO: Ctr. vs. Dev.: p=0.372, CLES=0.472, Ctr. vs. Red.: p=0.572, CLES=0.514, Dev. vs. Red.: p=0.206, CLES=0.544, Mann–Whitney U test with FDR-BH correction). We also quantified the visual adaptation and mismatch responses in local field potentials. The visually evoked negativities within the visual stimulation time window (adaptation response) in response to the redundant stimulus were significantly smaller than those to the control stimulus, in both WT and Aux-KO mice. We then measured mismatch response by comparing the mean potentials within 0.2-0.5 s after visual stimulation onset between responses to the deviant and redundant stimuli. The responses to the deviant stimulus

were significantly different from those to the redundant stimulus in WT mice, but not in Aux-KO mice. This result demonstrated that sensory adaptation and mismatch responses were impaired in Aux-KO mice, suggesting that the short-term plasticity or circuits for computing the redundant or deviant stimuli might have gone awry.

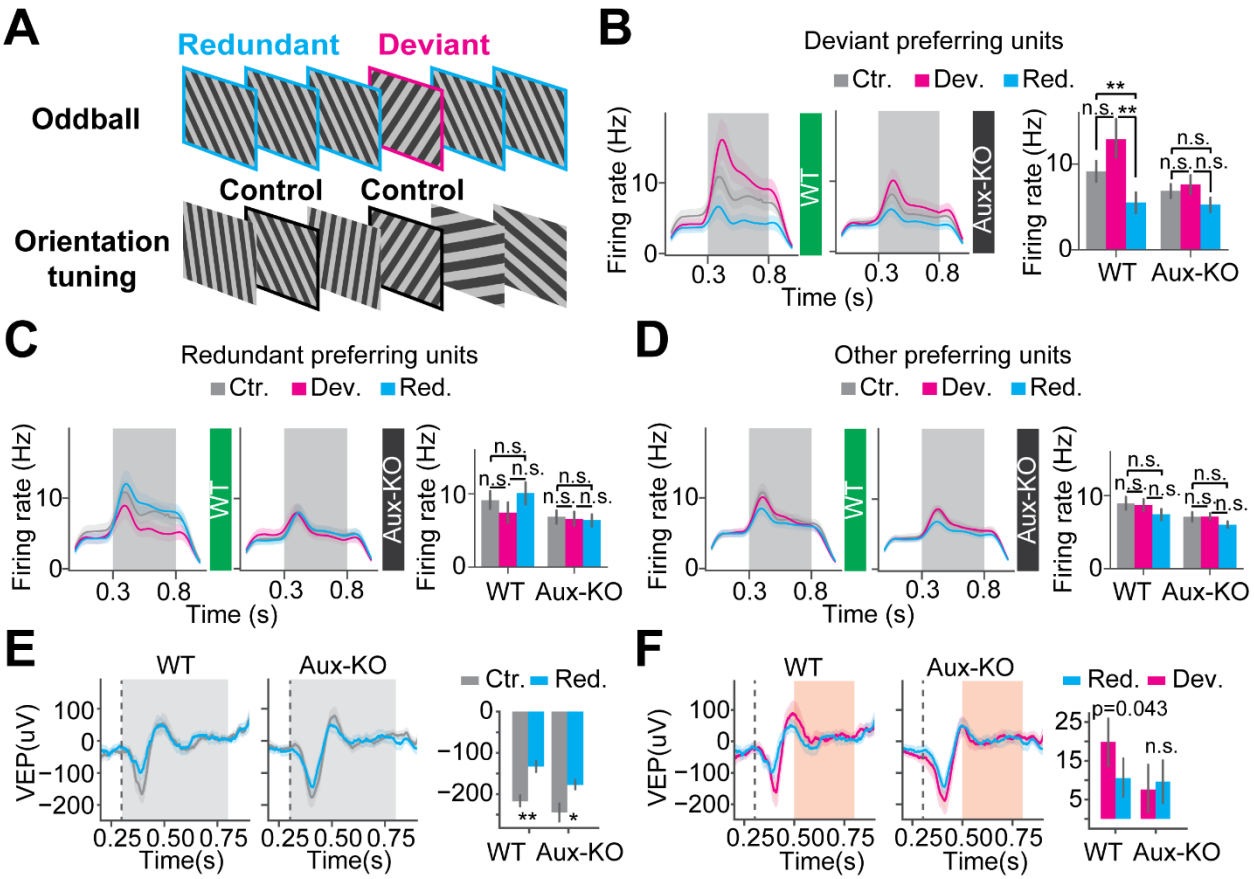

Figure 4.2. Stimulus-specific adaptation and mismatch response were present in mismatch stimulus preferring units, and were impaired in Auxilin KO mice. (A) The oddball paradigm. Two orientations were presented in a visual stimulation sequence. The redundant orientation was presented in 90% of the trials, and the deviant orientation was presented in 10% of the trials. The same two orientations were presented in another sequence of orientations with equal appearance frequency as controls. (B) Unit population averaged firing rates of the deviant orientation preferring units in response to the redundant, deviant, and control orientations. The gray shaded area represented the visual stimulation time window. The bar plot (right) showed visually locked mean firing rates (averaged within the visual stimulation time window). WT: N=50 units, 7 mice; Aux-KO: N=85 units, 10 mice. Mann–Whitney U test with FDR-BH correction. (C) Same as (B), but for redundant orientation preferring units. WT: N=63 units, 7 mice; Aux-KO: N=83 units, 10 mice. (D) Same as (B), but for other orientation preferring units. WT: N=203 units, 7 mice; Aux-KO: N=290 units, 10 mice. (E) Visually evoked potential in V1 layer 4 in responses to the control and redundant stimuli. The largest negativity within the visual stimulation time window of each recording was quantified. WT: N=18 recording sites, 6 mice; Aux-KO: N=30 recording sites, 10 mice. (F) Visually evoked potential in V1 layer 4 in responses to the deviant and redundant stimuli. The mean potential within 0.2-0.5s after the visual stimulation onset of each recording was quantified. WT: N=18 recording sites, 6 mice; Aux-KO: N=30 recording sites, 10 mice. Data were presented as mean ± SEM. *-p<0.05, **-p<0.01, ***-p<0.001, n.s.-not significant.

We also investigated whether visual experience dependent long-term plasticity would be impaired in Aux-KO mice, using a visual perceptual experience paradigm (Kissinger et al., 2020). Awake mice were head-fixed and viewed a drifting grating stimulus (30° oriented, 0.04 cycles per degree, drifting at 2 Hz, 200 ms presentation duration) for 200 repeats per day for four days. Extracellular activities in V1 were recorded both before and after the visual experience (**Figure 4.3**A). Unit firing rate z-scores were plotted in heatmaps, and the population responses showed multiple peaks after the visual experience in WT and Aux-KO mice (**Figure 4.3**B). The unit population averaged z-scores of Aux-KO mice showed delayed peak compared that of WT mice in pre-experience (**Figure 4.3**C top). At the same time, the unit population averaged z-scores of the Aux-KO mice showed smaller peak responses compare to those of WT mice in post-experience (**Figure 4.3**C bottom). To quantify whether there were differences in the response temporal dynamics between Aux-KO and WT mice, we looked at the z-score peak times of each unit in each group and compared their cumulative densities (**Figure 4.3**D). The units in Aux-KO mice showed slower response peaks compared to those in WT in pre-experience ($p=0.006$, statistic=0.145, Kolmogorov–Smirnov 2 sample test), and the delayed peak responses in Aux-KO mice became more obvious in post-experience ($p=1.81\text{x}10^{-6}$, statistic=0.190, Kolmogorov–Smirnov 2 sample test). To quantify the amplitudes of the peak response, we defined three time windows (0.53-0.63 s, 0.7-0.8 s, 0.9-1.0 s) and calculated the time-averaged z-scores within each time window as the response amplitudes for each unit (**Figure 4.3**E). In pre-experience, the visually locked responses were significantly smaller in Aux-KO mice, while the response amplitudes of the second and third time windows were significantly higher in Aux-KO mice (**Figure 4.3**E left, time window 1: $p=4.67\text{x}10^{-4}$, CLES=0.592, time window 2: $p=6.97\text{x}10^{-4}$, CLES=0.413, time window 3: $p=4.67\text{x}10^{-4}$, CLES=0.390, Mann–Whitney U test with FDR-BH correction). In post-experience, Aux-KO mice showed comparable first peak responses, but smaller second and the third peak responses compared to those of the WT mice (**Figure 4.3**E right, time window 1: $p=0.156$, CLES=0.532, time window 2: $p=0.068$, CLES=0.546, time window 3: $p=5.50\text{x}10^{-6}$, CLES=0.608, Mann–Whitney U test with FDR-BH correction). This result demonstrated that visual cortical neurons in Aux-KO mice showed delayed visual evoked responses to a brief presentation of visual stimulus, and the amplitudes of experience induced oscillatory peaks were reduced as well, suggesting delayed local circuit functional connections and impaired long-term plasticity of the functional circuits for the oscillations.

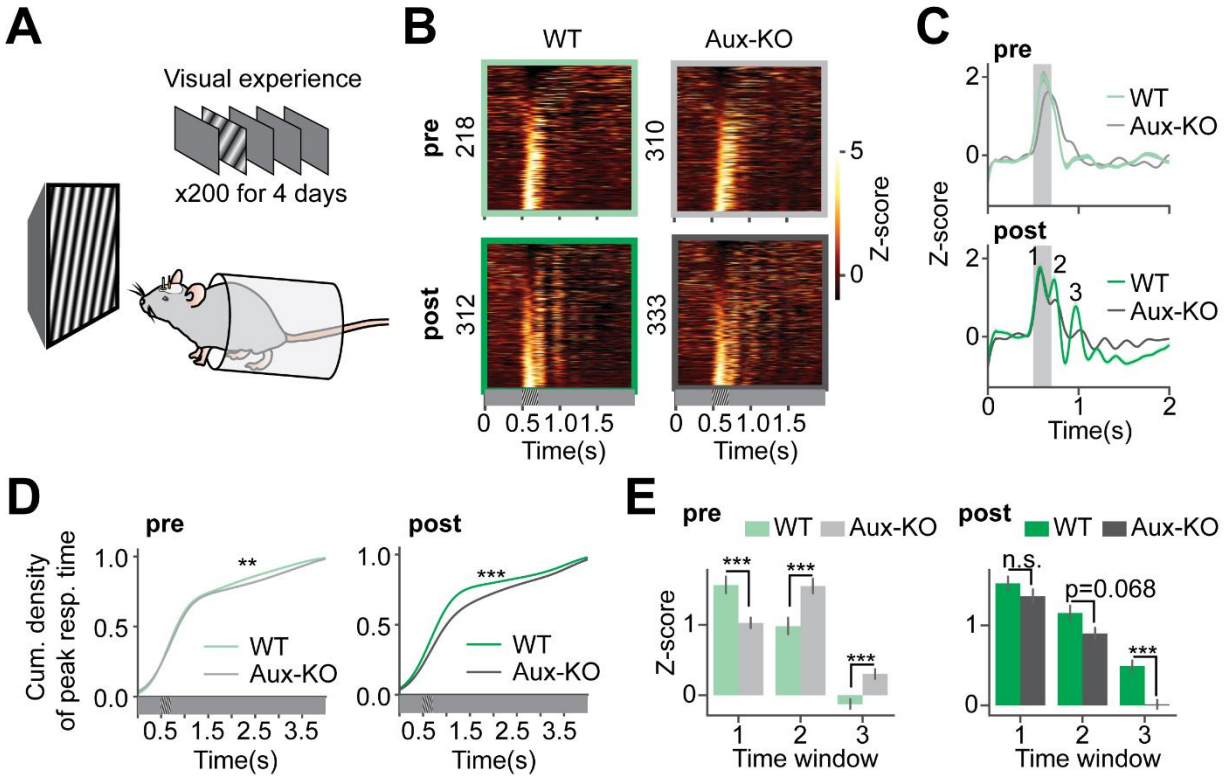

Figure 4.3. Visually evoked responses were reduced and delayed in Auxilin KO mice, in both pre-visual experience responses and post-visual experience oscillations. (A) Visual perceptual experience in head-fixed awake mice. Drifting gratings were presented to mice over four days, with 200 presentations per day. (B) Firing rate z-scores of all units were plotted in heatmaps. The numbers on the left denoted the number of units for each group. (C) Unit population averaged z-scores in pre-experience (top) and post-experience (bottom). The gray shaded area represented the visual stimulation time window. The numbers in the post-experience plot denoted three time windows of response peaks (0.53-0.63s,0.7-0.8s,0.9-1.0s). (D) Cumulative density plots of unit peak z-score times in pre-experience (left) and post-experience (right). Pre: WT: N=218 units, 7 mice, Aux-KO: N=310 units, 9 mice; Post: WT: N=312 units, 7 mice, Aux-KO: N=333 units, 8 mice. Kolmogorov–Smirnov 2 sample test. (E) Time-window averaged z-scores in pre-experience (left) and post-experience (right). Mann–Whitney U test with FDR-BH correction. WT: N=50 units, 7 mice; Aux-KO: N=85 units, 10 mice. Data were presented as mean ± SEM. *-p<0.05, **-p<0.01, ***-p<0.001, n.s.-not significant.

4.4 Discussion

In this study, we assessed visual cortical activities in sensory processing and learning in Aux-KO mice, and demonstrated functional impairments in visual orientation selectivity, visual adaptation and mismatch responses, as well as experience-dependent oscillations.

The visually evoked firing rates in V1 units were reduced in Aux-KO mice compared to WT mice, especially in their response to their preferred orientation. The overall reduced cortical activities are likely attributed to weaker thalamocortical innervation due to lack of readily releasing pool of vesicles, yet the V1 units still showed visual responses suggesting a compensatory mechanism for synaptic transmission might have been involved. In addition, the units in Aux-KO mice were less selective for orientations compared to WT mice, suggesting circuit computation for orientation selectivity might have gone awry, either in the thalamic circuits or local cortical circuits. The decreased selectivity is likely to lead to impaired visual recognition.

Visual adaptation and mismatch responses were also altered in Aux-KO mice. The units that preferred the deviant orientation did not respond in different amplitudes when the appearance frequencies of the visual stimulus changed. Lack of synaptic depression likely contributed to the impaired sensory adaptation and mismatch responses. Another possibility could be the functional circuits for the sensory adaptation and mismatch responses were not formed appropriately during development due to altered synaptic transmission.

Visual experience dependent oscillations were also altered in the Aux-KO mice. The visual experience induced oscillatory population responses were reduced, especially in the later peaks after the visual stimulation. Interestingly, the temporal dynamics of the oscillations were also different from WT mice, where the response peak of the unit population were significantly delayed. The delayed response peak was also seen in pre-experience, suggesting that the response delay could be largely resulted from altered synaptic transmission. On the other hand, altered long-term synaptic plasticity might have played a larger role in the smaller later peak responses in post-experience. It is also likely that the visual experience induced functional connectivity change amplified the difference in synaptic strength between Aux-KO and WT mice. Nevertheless, we demonstrated that visual learning was also impaired in Aux-KO mice.

4.5 Contribution statement

YT and AAC designed the extracellular recording experiments, SC provided transgenic mice, YT conducted extracellular recordings, YT analyzed extracellular recording data, YT wrote the raw draft for extracellular recording experiments.

4.6 Acknowledgement

We thank Alexandr Pak for suggestions on visual stimulus design.

CHAPTER 5. DISCUSSION AND FUTURE DIRECTIONS

My thesis revolves around neuronal circuit dynamics in health and disease. The first part of the thesis characterized cross-regional synchrony within the visual cortical network following visual perceptual experience in healthy mice. This work for the first time described inter-areal 4-8 Hz superficial layer LFP synchrony across mouse visual cortical regions persisting beyond visual stimulation time window, and revealed that the synchrony was expressed specifically between V1 and the higher-order visual area (HVA) with functional preference matching the entrained spatial frequency (SF) and temporal frequency (TF) content, in mice. The discovery of visual familiarity induced inter-areal 4-8 Hz synchrony extends the previous discovery of the 4-8 Hz oscillation in V1 after visual experience from our lab (Kissinger et al., 2018; Kissinger et al., 2020; Gao et al., 2021), and provided the first pivotal evidence supporting the role of 4-8 Hz oscillation in mediating cross-regional communication. Furthermore, the discovery also revealed that the visual familiarity induced 4-8 Hz synchrony was between V1 and a selective HVA that has functional preference matched with the familiar visual stimulus, suggesting that visual experience induced 4-8 Hz activity selectively mediated communications between visual cortical areas, similarly to what being proposed in the communication through coherence theory (Fries, 2005), where regions with synchronized excitability change would communicate more reliably and efficiently than the regions with not synchronized excitability change. Such 4-8 Hz visual cortical network synchrony has been mostly reported in primate studies in contexts of visual attention and working memory (Liebe et al., 2012; Spyropoulos et al., 2018), while our study extended the visual cortical network synchrony research scope to mouse models and in a new context of visual familiarity. The work is a key step for starting cortical network studies in mice, and for starting predictive coding theory study in the context of oscillations in mouse cortical network in the future. Interestingly, units in V1 showed higher spiking synchrony not only with units in the HVA that has functional preference matched the entrained SF and TF, but also with units in the other HVA, which was not easily relate to the LFP synchrony, but revealed the possibility that the subthreshold activity might primarily contribute to the 4-8 Hz synchrony between selective visual cortices. It is also possible that the unit population represents a heterogenous population with their inter-areal functional connectivity changes in different directions, and visual experience induced changes might be present in only a

subset of connections. Future studies could utilize mouse lines with genetically labeled projections of interest to study functional changes in subpopulations of neurons after visual familiarization.

The other parts of my thesis looked at V1 activity in disease and following a novel CNS therapy. One project looked at recovery of visually evoked response in mouse V1 after ischemia through NeuroD1 mediated astrocyte-to-neuron conversion, where we characterized the formation of cortical laminated structure from the converted neurons, longitudinal recovery of visually evoked responses of unit populations in V1, and units' selective responses to orientations. Another project looked at altered visual cortical activity in an Auxilin knockout mouse model, which demonstrated overall reduced visually evoked responses, less selective responses to orientations, impaired visual adaptive responses and mismatch responses, as well as slower visual experience induced oscillations. These projects utilized the high-density silicon probe recording technique to 1) characterize visual cortical function recovery following a therapy, which provided evidence for its high efficacy for recovering physiological functions, and to 2) phenotype visual cortical functional impairments in a mouse disease model, which provided more basic understanding of Auxilin related disease.

In sum, my thesis took advantage of the high-density silicon probe recording technique to probe neuronal circuits in health and disease. The discovery of visual experience induced inter-areal 4-8 Hz synchrony paves the way for studying 4-8 Hz activity in relation to stream-dependent visual processing and predictive coding in health and disease.

APPENDIX

Extended Table 1-1. Statistics for 4-8 Hz power comparisons for each stimulus between post- and pre- entrainment of SF and TF that matched LM's functional preference.

Extended Table 1-1, statistics for 4-8 Hz power comparisons between post- and pre- experience						
	TF (Hz)	SF (cpd)	CLES	U-val	p-val	p-corr
V1	0.75	0.015	0.718881	1721	0.00021	0.000526
	0.75	0.03	0.644946	1544	0.014159	0.018631
	0.75	0.06	0.697995	1671	0.000801	0.001541
	0.75	0.12	0.704313	1927	0.000327	0.000744
	0.75	0.24	0.808688	1936	1.71E-07	2.14E-06
	1.5	0.015	0.796575	1907	5.08E-07	4.23E-06
	1.5	0.03	0.604845	1448	0.076142	0.090646
	1.5	0.06	0.668338	1600	0.004376	0.007294
	1.5	0.12	0.755221	1808	1.54E-05	6.43E-05
	1.5	0.24	0.727235	1741	0.000119	0.000331
	3	0.015	0.516291	1236	0.785178	0.785178
	3	0.03	0.580201	1389	0.175161	0.190393
	3	0.06	0.578112	1384	0.1867	0.194479
	3	0.12	0.733083	1755	7.91E-05	0.000247
	3	0.24	0.748538	1792	2.56E-05	9.16E-05
	6	0.015	0.657059	1573	0.007849	0.010901
	6	0.03	0.665831	1594	0.004998	0.007809
	6	0.06	0.599415	1435	0.092669	0.105306
	6	0.12	0.681704	1632	0.002096	0.003744
	6	0.24	0.703425	1684	0.000572	0.001192
	12	0.015	0.657895	1575	0.007525	0.010901
	12	0.03	0.776525	1859	2.82E-06	1.76E-05
	12	0.06	0.639515	1531	0.018218	0.022773
	12	0.12	0.756475	1811	1.40E-05	6.43E-05
	12	0.24	0.832916	1994	1.71E-08	4.27E-07
LM	TF (Hz)	SF (cpd)	CLES	U-val	p-val	p-corr
	0.75	0.015	0.636111	687	0.064932	0.0773
	0.75	0.03	0.697222	753	0.007423	0.018557
	0.75	0.06	0.778704	841	0.000153	0.000957
	0.75	0.12	0.69037	932	0.005537	0.015382
	0.75	0.24	0.758333	819	0.00045	0.002251
	1.5	0.015	0.637037	688	0.063123	0.0773
	1.5	0.03	0.639815	691	0.057944	0.0773
	1.5	0.06	0.661111	714	0.028823	0.048039
	1.5	0.12	0.655556	708	0.034832	0.054426
	1.5	0.24	0.596296	644	0.192241	0.208958
	3	0.015	0.525	567	0.738479	0.738479

	3	0.03	0.661111	714	0.028823	0.048039
	3	0.06	0.612037	661	0.128975	0.146562
	3	0.12	0.706481	763	0.005059	0.015382
	3	0.24	0.687037	742	0.011128	0.024907
	6	0.015	0.637963	689	0.061356	0.0773
	6	0.03	0.680556	735	0.014267	0.027437
	6	0.06	0.573148	619	0.32266	0.336104
	6	0.12	0.728704	787	0.001899	0.006782
	6	0.24	0.652778	705	0.038218	0.056203
	12	0.015	0.685185	740	0.011955	0.024907
	12	0.03	0.749074	809	0.000718	0.00299
	12	0.06	0.812037	877	2.24E-05	0.000187
	12	0.12	0.863889	933	7.61E-07	9.52E-06
	12	0.24	0.921296	995	1.03E-08	2.57E-07
AL	TF (Hz)	SF (cpd)	CLES	U-val	p-val	p-corr
	0.75	0.015	0.530864	344	0.720483	0.834387
	0.75	0.03	0.695988	451	0.020276	0.168968
	0.75	0.06	0.49537	321	0.963411	0.978042
	0.75	0.12	0.640212	484	0.080934	0.224817
	0.75	0.24	0.658951	427	0.059997	0.223349
	1.5	0.015	0.662037	429	0.055173	0.223349
	1.5	0.03	0.657407	426	0.062538	0.223349
	1.5	0.06	0.530864	344	0.720483	0.834387
	1.5	0.12	0.458333	297	0.626784	0.834387
	1.5	0.24	0.628086	407	0.13007	0.295614
	3	0.015	0.291667	189	0.013587	0.168968
	3	0.03	0.533951	346	0.693203	0.834387
	3	0.06	0.503086	326	0.978042	0.978042
	3	0.12	0.529321	343	0.73426	0.834387
	3	0.24	0.617284	400	0.165936	0.330031
	6	0.015	0.506173	328	0.948793	0.978042
	6	0.03	0.467593	303	0.706796	0.834387
	6	0.06	0.410494	266	0.291384	0.520329
	6	0.12	0.615741	399	0.171616	0.330031
	6	0.24	0.708333	459	0.013587	0.168968
	12	0.015	0.584877	379	0.31729	0.528817
	12	0.03	0.62963	408	0.125479	0.295614
	12	0.06	0.665123	431	0.050676	0.223349
	12	0.12	0.648148	420	0.079711	0.224817
	12	0.24	0.564815	366	0.446359	0.697435

Extended Table 2-1. Statistics for 4-8 Hz power comparisons for each stimulus between post- and pre- entrainment of SF and TF that matched AL's functional preference.

Extended Table 2-1, statistics for 4-8 Hz power comparisons between post- and pre- experience						
	TF (Hz)	SF (cpd)	CLES	U-val	p-val	p-corr
V1	0.75	0.015	0.616922	1451	0.048771	0.121926
	0.75	0.03	0.659439	1551	0.007178	0.044862
	0.75	0.06	0.548895	1291	0.41109	0.489393
	0.75	0.12	0.517857	1218	0.765763	0.765763
	0.75	0.24	0.571429	1344	0.229187	0.330048
	1.5	0.015	0.71301	1677	0.000327	0.004086
	1.5	0.03	0.624575	1469	0.035745	0.121926
	1.5	0.06	0.647109	1522	0.013128	0.065638
	1.5	0.12	0.60034	1412	0.09091	0.169824
	1.5	0.24	0.590986	1390	0.125354	0.208923
	3	0.015	0.566752	1333	0.26123	0.334217
	3	0.03	0.599065	1409	0.095101	0.169824
	3	0.06	0.629677	1481	0.028819	0.120078
	3	0.12	0.565901	1331	0.267374	0.334217
	3	0.24	0.617772	1453	0.04715	0.121926
	6	0.015	0.622024	1463	0.039711	0.121926
	6	0.03	0.781463	1838	2.05E-06	5.12E-05
	6	0.06	0.535289	1259	0.55368	0.601826
	6	0.12	0.578231	1360	0.187732	0.293332
	6	0.24	0.542517	1276	0.475045	0.539824
	12	0.015	0.606718	1427	0.07213	0.163931
	12	0.03	0.701105	1649	0.000694	0.005782
	12	0.06	0.570153	1341	0.237635	0.330048
	12	0.12	0.474915	1117	0.674513	0.702618
	12	0.24	0.603741	1420	0.080456	0.167616
LM	TF (Hz)	SF (cpd)	CLES	U-val	p-val	p-corr
	0.75	0.015	0.546032	516	0.553865	0.602027
	0.75	0.03	0.708995	670	0.006686	0.041788
	0.75	0.06	0.555556	525	0.474065	0.574534
	0.75	0.12	0.520635	492	0.793652	0.793652
	0.75	0.24	0.586243	554	0.264798	0.442036
	1.5	0.015	0.638095	603	0.073502	0.183755
	1.5	0.03	0.597884	565	0.205313	0.427736
	1.5	0.06	0.548148	518	0.535579	0.602027
	1.5	0.12	0.584127	552	0.276777	0.442036
	1.5	0.24	0.561905	531	0.424591	0.574534
	3	0.015	0.421164	398	0.30832	0.453412
	3	0.03	0.583069	551	0.282903	0.442036
	3	0.06	0.557672	527	0.457231	0.574534
	3	0.12	0.554497	524	0.482608	0.574534

	3	0.24	0.52381	495	0.761987	0.793652
	6	0.015	0.592593	560	0.231025	0.442036
	6	0.03	0.73545	695	0.002241	0.018676
	6	0.06	0.626455	592	0.32266	0.230378
	6	0.12	0.665608	629	0.001899	0.099194
	6	0.24	0.75873	717	0.038218	0.009773
	12	0.015	0.648677	613	0.011955	0.149815
	12	0.03	0.695238	657	0.000718	0.047106
	12	0.06	0.702646	664	2.24E-05	0.042757
	12	0.12	0.669841	633	7.61E-07	0.098626
	12	0.24	0.814815	770	4.34E-05	0.001084
AL	TF (Hz)	SF (cpd)	CLES	U-val	p-val	p-corr
	0.75	0.015	0.542328	410	0.602293	0.752866
	0.75	0.03	0.691799	523	0.016827	0.080168
	0.75	0.06	0.513228	388	0.87512	0.911583
	0.75	0.12	0.518519	392	0.823278	0.894867
	0.75	0.24	0.62037	469	0.134355	0.351834
	1.5	0.015	0.687831	520	0.01924	0.080168
	1.5	0.03	0.624339	472	0.121917	0.351834
	1.5	0.06	0.506614	383	0.940657	0.940657
	1.5	0.12	0.441799	334	0.471757	0.655218
	1.5	0.24	0.522487	395	0.784884	0.891913
	3	0.015	0.468254	354	0.697452	0.8303
	3	0.03	0.710317	537	0.00874	0.066196
	3	0.06	0.609788	461	0.172315	0.351834
	3	0.12	0.600529	454	0.211665	0.377973
	3	0.24	0.679894	514	0.024988	0.089244
	6	0.015	0.607143	459	0.182954	0.351834
	6	0.03	0.832011	629	3.41E-05	0.000853
	6	0.06	0.548942	415	0.545962	0.718371
	6	0.12	0.607143	459	0.182954	0.351834
	6	0.24	0.568783	430	0.394232	0.615988
	12	0.015	0.705026	533	0.010591	0.066196
	12	0.03	0.780423	590	0.000467	0.005841
	12	0.06	0.611111	462	0.167173	0.351834
	12	0.12	0.587302	444	0.278555	0.464259
	12	0.24	0.563492	426	0.431988	0.635276

Extended Table 3-1. Statistics for comparisons of 4-8 Hz V1-LM PLV for each stimulus between post- and pre- entrainment of SF and TF that matched LM's functional preference.

Extended Table 3-1. Statistics for comparisons of 4-8 Hz V1-LM PLV between post- and pre-experience						
	TF (Hz)	SF (cpd)	CLES	U-val	p-val	p-corr
V1-LM	0.75	0.015	0.616922	1451	0.048771	0.121926
	0.75	0.03	0.659439	1551	0.007178	0.044862
	0.75	0.06	0.548895	1291	0.41109	0.489393
	0.75	0.12	0.517857	1218	0.765763	0.765763
	0.75	0.24	0.571429	1344	0.229187	0.330048
	1.5	0.015	0.71301	1677	0.000327	0.004086
	1.5	0.03	0.624575	1469	0.035745	0.121926
	1.5	0.06	0.647109	1522	0.013128	0.065638
	1.5	0.12	0.60034	1412	0.09091	0.169824
	1.5	0.24	0.590986	1390	0.125354	0.208923
	3	0.015	0.566752	1333	0.26123	0.334217
	3	0.03	0.599065	1409	0.095101	0.169824
	3	0.06	0.629677	1481	0.028819	0.120078
	3	0.12	0.565901	1331	0.267374	0.334217
	3	0.24	0.617772	1453	0.04715	0.121926
	6	0.015	0.622024	1463	0.039711	0.121926
	6	0.03	0.781463	1838	2.05E-06	5.12E-05
	6	0.06	0.535289	1259	0.55368	0.601826
	6	0.12	0.578231	1360	0.187732	0.293332
	6	0.24	0.542517	1276	0.475045	0.539824
	12	0.015	0.606718	1427	0.07213	0.163931
	12	0.03	0.701105	1649	0.000694	0.005782
	12	0.06	0.570153	1341	0.237635	0.330048
	12	0.12	0.474915	1117	0.674513	0.702618
	12	0.24	0.080456	1420	0.603741	0.167616

Extended Table 3-2. Statistics for comparisons of 4-8 Hz V1-AL PLV for each stimulus between post- and pre- entrainment of SF and TF that matched with LM's functional preference.

Extended Table 3-2. Statistics for comparisons of 4-8 Hz V1-AL PLV between post- and pre-experience						
	TF (Hz)	SF (cpd)	CLES	U-val	p-val	p-corr
V1-AL	0.75	0.015	0.544872	2295	0.382972	0.517302
	0.75	0.03	0.585945	2468	0.094302	0.15717
	0.75	0.06	0.72792	3066	8.96E-06	8.86E-05
	0.75	0.12	0.501425	2112	0.979692	0.979692
	0.75	0.24	0.647911	2729	0.003963	0.009907
	1.5	0.015	0.65812	2772	0.002069	0.00739
	1.5	0.03	0.531576	2239	0.539712	0.67464
	1.5	0.06	0.651472	2744	0.003172	0.008812
	1.5	0.12	0.60114	2532	0.048914	0.101905
	1.5	0.24	0.512346	2158	0.811604	0.909517
	3	0.015	0.639601	2694	0.006546	0.014876
	3	0.03	0.666904	2809	0.001148	0.005742
	3	0.06	0.726021	3058	1.06E-05	8.86E-05
	3	0.12	0.655033	2759	0.002528	0.0079
	3	0.24	0.50831	2141	0.873136	0.909517
	6	0.015	0.515907	2173	0.758249	0.902677
	6	0.03	0.65812	2772	0.002069	0.00739
	6	0.06	0.733618	3090	5.32E-06	8.86E-05
	6	0.12	0.599003	2523	0.053895	0.103643
	6	0.24	0.702279	2958	8.11E-05	0.000507
	12	0.015	0.509972	2148	0.847684	0.909517
	12	0.03	0.582384	2453	0.10878	0.169968
	12	0.06	0.543922	2291	0.39315	0.517302
	12	0.12	0.434948	1832	0.205571	0.302311
	12	0.24	0.590218	2486	0.079014	0.141096

Extended Table 4-1. Statistics for comparisons of 4-8 Hz V1-LM PLV for each stimulus between post- and pre- entrainment of SF and TF that matched AL's functional preference.

Extended Table 4-1. Statistics for comparisons of 4-8 Hz V1-LM PLV between post- and pre-experience						
	TF (Hz)	SF (cpd)	CLES	U-val	p-val	p-corr
V1-LM	0.75	0.015	0.375661	2130	0.00901	0.028156
	0.75	0.03	0.409171	2320	0.056479	0.128361
	0.75	0.06	0.421164	2388	0.097876	0.188224
	0.75	0.12	0.43739	2480	0.188786	0.294977
	0.75	0.24	0.404409	2293	0.044705	0.111764
	1.5	0.015	0.33933	1924	0.000737	0.009215
	1.5	0.03	0.473721	2686	0.58197	0.692821
	1.5	0.06	0.46067	2612	0.409463	0.568699
	1.5	0.12	0.415873	2358	0.07732	0.161084
	1.5	0.24	0.370018	2098	0.006328	0.023372
	3	0.015	0.353086	2002	0.002027	0.012055
	3	0.03	0.519048	2943	0.690249	0.719009
	3	0.06	0.471252	2672	0.546901	0.692821
	3	0.12	0.458907	2602	0.388737	0.568699
	3	0.24	0.370547	2101	0.006544	0.023372
	6	0.015	0.477425	2707	0.636456	0.694677
	6	0.03	0.387831	2199	0.018479	0.051329
	6	0.06	0.477601	2708	0.639103	0.694677
	6	0.12	0.353616	2005	0.002105	0.012055
	6	0.24	0.436508	2475	0.182625	0.294977
	12	0.015	0.42522	2411	0.116421	0.207895
	12	0.03	0.471781	2675	0.554327	0.692821
	12	0.06	0.485362	2752	0.759727	0.759727
	12	0.12	0.355556	2016	0.002411	0.012055
	12	0.24	0.292593	1659	1.31E-05	0.000329

Extended Table 4-2. Statistics for comparisons of 4-8 Hz V1-AL PLV for each stimulus between post- and pre- entrainment of SF and TF that matched AL's functional preference.

Extended Table 4-2. Statistics for comparisons of 4-8 Hz V1-AL PLV between post- and pre-experience						
	TF (Hz)	SF (cpd)	CLES	U-val	p-val	p-corr
V1-AL	0.75	0.015	0.359687	1010	0.01645	0.045696
	0.75	0.03	0.276709	777	0.000134	0.000837
	0.75	0.06	0.478632	1344	0.716821	0.775336
	0.75	0.12	0.323718	909	0.002574	0.012872
	0.75	0.24	0.262108	736	4.72E-05	0.000393
	1.5	0.015	0.236823	665	6.74E-06	8.42E-05
	1.5	0.03	0.428775	1204	0.223929	0.329307
	1.5	0.06	0.357906	1005	0.01513	0.045696
	1.5	0.12	0.233008	1145	5.37E-08	1.34E-06
	1.5	0.24	0.330128	927	0.003676	0.015315
	3	0.015	0.464387	1304	0.54415	0.680187
	3	0.03	0.524929	1474	0.671806	0.775336
	3	0.06	0.584046	1640	0.151116	0.236118
	3	0.12	0.657407	1846	0.007116	0.025414
	3	0.24	0.384615	1080	0.048604	0.12151
	6	0.015	0.537393	1509	0.524106	0.680187
	6	0.03	0.603276	1694	0.0776	0.161667
	6	0.06	0.587607	1650	0.134507	0.236118
	6	0.12	0.610399	1714	0.0592	0.134546
	6	0.24	0.58547	1644	0.144294	0.236118
	12	0.015	0.407051	1143	0.112286	0.215935
	12	0.03	0.522436	1467	0.703204	0.775336
	12	0.06	0.54594	1533	0.433432	0.601989
	12	0.12	0.483974	1359	0.786183	0.786183
	12	0.24	0.519231	1458	0.744322	0.775336

Extended Table 5-1. Statistics for 4-8 Hz intra-areal PPC comparisons for each stimulus between post- and pre- entrainment of SF and TF that matched LM's functional preference.

Extended Table 5-1, statistics for 4-8 Hz intra-areal PPC comparisons for each stimulus between post- and pre- experience						
	TF (Hz)	SF (cpd)	CLES	U-val	p-val	p-corr
V1	0.75	0.015	0.661937	509015	3.01E-31	2.51E-30
	0.75	0.03	0.628302	495818	1.46E-20	3.33E-20
	0.75	0.06	0.644663	502605	1.77E-25	6.31E-25
	0.75	0.12	0.71428	684310	4.91E-59	1.23E-57
	0.75	0.24	0.673626	628202	3.95E-39	4.94E-38
	1.5	0.015	0.603062	490826	5.44E-14	9.07E-14
	1.5	0.03	0.646625	528717	1.07E-26	5.34E-26
	1.5	0.06	0.609713	509610	6.46E-16	1.15E-15
	1.5	0.12	0.645944	585152	6.23E-28	3.89E-27
	1.5	0.24	0.612809	538902	4.28E-17	8.23E-17
	3	0.015	0.527963	386418	0.04583	0.04583
	3	0.03	0.568981	431128	7.02E-07	8.35E-07
	3	0.06	0.575127	439931	6.41E-08	8.01E-08
	3	0.12	0.633255	560512	2.95E-23	8.19E-23
	3	0.24	0.628345	517282	5.11E-21	1.28E-20
	6	0.015	0.553529	429968	0.000106	0.000121
	6	0.03	0.550704	417945	0.00026	0.000282
	6	0.06	0.580158	451814	6.32E-09	8.32E-09
	6	0.12	0.586226	502114	1.63E-10	2.27E-10
	6	0.24	0.589383	501645	3.64E-11	5.35E-11
	12	0.015	0.530967	418933	0.024314	0.025327
	12	0.03	0.619211	539167	7.42E-19	1.55E-18
	12	0.06	0.592743	517618	5.75E-12	8.98E-12
	12	0.12	0.633083	593805	6.44E-24	2.01E-23
	12	0.24	0.637476	600797	1.77E-25	6.31E-25
LM	TF (Hz)	SF (cpd)	CLES	U-val	p-val	p-corr
	0.75	0.015	0.628611	74249	6.02E-09	1.88E-08
	0.75	0.03	0.586628	65104	0.000111	0.000132
	0.75	0.06	0.572245	63803	0.001256	0.001365
	0.75	0.12	0.613419	81835	1.13E-07	2.83E-07
	0.75	0.24	0.613358	74523	2.30E-07	4.42E-07
	1.5	0.015	0.605631	60769	4.38E-06	6.45E-06
	1.5	0.03	0.635227	70495	1.85E-09	7.70E-09
	1.5	0.06	0.591611	65796	4.52E-05	5.65E-05
	1.5	0.12	0.552826	69750	0.015283	0.015283
	1.5	0.24	0.639984	80286	1.22E-10	7.64E-10
	3	0.015	0.616249	57570	7.24E-07	1.29E-06
	3	0.03	0.624871	53449	1.86E-07	3.88E-07
	3	0.06	0.602388	56810	1.22E-05	1.60E-05

	3	0.12	0.635255	67647	2.32E-09	8.27E-09
	3	0.24	0.561094	67439	0.005487	0.005716
	6	0.015	0.61316	57068	1.39E-06	2.32E-06
	6	0.03	0.609144	54971	3.89E-06	6.07E-06
	6	0.06	0.657001	69018	6.34E-12	5.29E-11
	6	0.12	0.638042	78862	2.81E-10	1.40E-09
	6	0.24	0.586448	62031	0.000143	0.000163
	12	0.015	0.627028	61534	4.08E-08	1.13E-07
	12	0.03	0.600791	66817	7.18E-06	9.98E-06
	12	0.06	0.652389	82201	2.51E-12	3.14E-11
	12	0.12	0.607088	99441	1.55E-07	3.53E-07
	12	0.24	0.695294	85816	4.96E-19	1.24E-17
AL	TF (Hz)	SF (cpd)	CLES	U-val	p-val	p-corr
	0.75	0.015	0.574185	32763	0.005951	0.019457
	0.75	0.03	0.569643	39278	0.006562	0.019457
	0.75	0.06	0.57846	39053	0.002443	0.010179
	0.75	0.12	0.674207	51771	1.74E-12	4.35E-11
	0.75	0.24	0.562498	43485	0.011922	0.027096
	1.5	0.015	0.53253	30433	0.227039	0.256881
	1.5	0.03	0.548234	40975	0.056389	0.082925
	1.5	0.06	0.611437	45058	1.02E-05	0.000128
	1.5	0.12	0.565958	41882	0.00828	0.020699
	1.5	0.24	0.57121	34685	0.007005	0.019457
	3	0.015	0.473275	27431	0.319035	0.332328
	3	0.03	0.540754	32794	0.122662	0.153327
	3	0.06	0.551941	31369	0.054142	0.082925
	3	0.12	0.55932	32473	0.025321	0.04719
	3	0.24	0.559787	31586	0.026427	0.04719
	6	0.015	0.465158	31694	0.174863	0.208171
	6	0.03	0.548386	35780	0.061972	0.086073
	6	0.06	0.54475	34450	0.089536	0.117811
	6	0.12	0.596734	40921	0.000153	0.000955
	6	0.24	0.54973	42692	0.045122	0.075204
	12	0.015	0.483282	33736	0.511994	0.511994
	12	0.03	0.565781	33002	0.013669	0.028477
	12	0.06	0.598543	39028	0.000138	0.000955
	12	0.12	0.53124	32905	0.23633	0.256881
	12	0.24	0.591002	39304	0.000419	0.002097

Extended Table 6-1. Statistics for 4-8 Hz intra-areal PPC comparisons for each stimulus between post- and pre- entrainment of SF and TF that matched AL's functional preference.

Extended Table 6-1, statistics for 4-8 Hz intra-areal PPC comparisons for each stimulus between post- and pre- experience						
	TF (Hz)	SF (cpd)	CLES	U-val	p-val	p-corr
V1	0.75	0.015	0.6078	288897	4.27E-12	1.34E-11
	0.75	0.03	0.706116	395603	2.27E-43	5.69E-42
	0.75	0.06	0.605348	293866	1.01E-11	2.80E-11
	0.75	0.12	0.556368	296124	0.000196	0.000258
	0.75	0.24	0.563106	301863	2.99E-05	4.15E-05
	1.5	0.015	0.646559	347564	2.60E-22	1.30E-21
	1.5	0.03	0.664155	356763	1.41E-27	1.02E-26
	1.5	0.06	0.583183	309600	4.04E-08	8.42E-08
	1.5	0.12	0.5941	331489	3.24E-10	8.10E-10
	1.5	0.24	0.563136	318163	2.29E-05	3.44E-05
	3	0.015	0.568615	274682	9.95E-06	1.78E-05
	3	0.03	0.60693	302130	3.78E-12	1.34E-11
	3	0.06	0.565569	273767	2.34E-05	3.44E-05
	3	0.12	0.551058	282019	0.000852	0.001014
	3	0.24	0.542721	273529	0.005401	0.006137
	6	0.015	0.587264	316723	7.20E-09	1.64E-08
	6	0.03	0.666532	338785	1.63E-27	1.02E-26
	6	0.06	0.553939	280989	0.000435	0.000544
	6	0.12	0.473835	243357	0.087396	0.091038
	6	0.24	0.534302	279490	0.024311	0.026425
	12	0.015	0.615939	347959	7.33E-15	3.06E-14
	12	0.03	0.66531	387809	5.27E-29	6.58E-28
	12	0.06	0.566771	294490	1.17E-05	1.95E-05
	12	0.12	0.525084	294804	0.09363	0.09363
	12	0.24	0.566902	321709	7.33E-06	1.41E-05
LM	TF (Hz)	SF (cpd)	CLES	U-val	p-val	p-corr
	0.75	0.015	0.567305	38191	0.008417	0.042085
	0.75	0.03	0.557203	45256	0.018328	0.065457
	0.75	0.06	0.511594	41126	0.633579	0.729123
	0.75	0.12	0.532648	47623	0.169952	0.32683
	0.75	0.24	0.530735	41098	0.212293	0.379095
	1.5	0.015	0.536601	36725	0.148567	0.309514
	1.5	0.03	0.560075	40951	0.015753	0.065457
	1.5	0.06	0.505114	34421	0.840571	0.875595
	1.5	0.12	0.498768	39273	0.960028	0.960028
	1.5	0.24	0.567481	48321	0.004911	0.030696
	3	0.015	0.453507	21918	0.095174	0.237934
	3	0.03	0.562106	29976	0.021523	0.067259
	3	0.06	0.460319	26072	0.135884	0.308828

	3	0.12	0.581674	45032	0.00088	0.007333
	3	0.24	0.521884	36427	0.387583	0.53831
	6	0.015	0.4846	29800	0.554318	0.692897
	6	0.03	0.607138	43108	1.88E-05	0.000469
	6	0.06	0.55254	32517	0.04612	0.128112
	6	0.12	0.517841	37283	0.476852	0.627437
	6	0.24	0.522828	32637	0.379935	0.53831
	12	0.015	0.511235	29987	0.670794	0.729123
	12	0.03	0.526002	38172	0.29741	0.495683
	12	0.06	0.523918	38618	0.337607	0.527511
	12	0.12	0.511015	43283	0.648537	0.729123
	12	0.24	0.585306	45195	0.000515	0.006437
AL	TF (Hz)	SF (cpd)	CLES	U-val	p-val	p-corr
	0.75	0.015	0.583081	56560	0.000333	0.004164
	0.75	0.03	0.574372	66201	0.000797	0.006639
	0.75	0.06	0.564148	53400	0.006083	0.030416
	0.75	0.12	0.542643	55558	0.06194	0.119116
	0.75	0.24	0.472088	48161	0.223342	0.398825
	1.5	0.015	0.565407	58765	0.004057	0.025354
	1.5	0.03	0.500446	57216	0.984171	0.993264
	1.5	0.06	0.543875	51890	0.060434	0.119116
	1.5	0.12	0.478318	43349	0.358075	0.559493
	1.5	0.24	0.562994	51103	0.007475	0.031147
	3	0.015	0.484121	44072	0.499999	0.735292
	3	0.03	0.550195	55611	0.028517	0.079214
	3	0.06	0.486646	41105	0.578136	0.802967
	3	0.12	0.499784	37021	0.993264	0.993264
	3	0.24	0.473571	35532	0.285914	0.476523
	6	0.015	0.50076	53354	0.973351	0.993264
	6	0.03	0.641247	55716	3.17E-09	7.93E-08
	6	0.06	0.503148	50979	0.890936	0.993264
	6	0.12	0.489133	44829	0.644103	0.805128
	6	0.24	0.49739	49162	0.910282	0.993264
	12	0.015	0.489751	56434	0.644099	0.805128
	12	0.03	0.555031	63046	0.013614	0.042544
	12	0.06	0.546538	52853	0.044608	0.101383
	12	0.12	0.44376	46727	0.013158	0.042544
	12	0.24	0.547174	57438	0.037699	0.094248

Extended Table 7-1. Statistics for synchrony index std. comparisons between post- and pre-experience for each functional group.

Extended Table 7-1, statistics for synchrony index comparisons between post- and pre-entrainment of SF and TF that matched LM's functional preference for each functional group								
	V1-LM visually locked unit pair groups							
	TF (Hz)	SF (cpd)	Post unit pair N	Pre unit pair N	CLES	U-val	p-val	p-corr
Entrainment of SF and TF that matched LM's functional preference	0.75	0.015	182	68	0.378313	4682	0.003086	0.011023
	0.75	0.03	144	38	0.431469	2361	0.194833	0.270601
	0.75	0.06	122	64	0.336962	2631	0.000264	0.001321
	0.75	0.12	74	41	0.599868	1820	0.077335	0.129398
	0.75	0.24	137	65	0.466816	4157	0.447219	0.559024
	1.5	0.015	120	60	0.419167	3018	0.077639	0.129398
	1.5	0.03	194	54	0.554219	5806	0.223531	0.29412
	1.5	0.06	139	65	0.391256	3535	0.012435	0.034542
	1.5	0.12	138	54	0.495035	3689	0.916034	0.916034
	1.5	0.24	120	98	0.280697	3301	2.61E-08	3.26E-07
	3	0.015	102	77	0.383881	3015	0.007916	0.024739
	3	0.03	153	53	0.528055	4282	0.543889	0.640037
	3	0.06	108	60	0.229475	1487	6.58E-09	1.65E-07
	3	0.12	137	88	0.403865	4869	0.015047	0.037616
	3	0.24	127	66	0.430446	3608	0.113562	0.167003
	6	0.015	128	82	0.477706	5014	0.586764	0.640037
	6	0.03	130	46	0.420569	2515	0.110114	0.167003
	6	0.06	143	74	0.482612	5107	0.675568	0.703717
	6	0.12	157	77	0.478203	5781	0.588834	0.640037
	6	0.24	125	89	0.316404	3520	4.79E-06	3.73E-05
	12	0.015	134	71	0.34938	3324	0.000393	0.001638
	12	0.03	141	90	0.407329	5169	0.017634	0.040076
	12	0.06	171	76	0.575331	7477	0.059015	0.122948
	12	0.12	105	65	0.29304	2000	5.96E-06	3.73E-05
	12	0.24	122	87	0.42557	4517	0.066971	0.128791
	V1-LM post-stimulus unit pair groups							
	TF (Hz)	SF (cpd)	Post unit pair N	Pre unit pair N	CLES	U-val	p-val	p-corr
	0.75	0.015	75	25	0.682133	1279	0.006638	0.033192
	0.75	0.03	85	36	0.606536	1856	0.064973	0.108288
	0.75	0.06	57	26	0.587045	870	0.207084	0.304535
	0.75	0.12	53	26	0.661103	911	0.020834	0.052495
	0.75	0.24	51	33	0.65003	1094	0.020998	0.052495
	1.5	0.015	56	32	0.533482	956	0.605776	0.721162

	1.5	0.03	114	37	0.674727	2846	0.001441	0.018012
	1.5	0.06	55	29	0.638871	1019	0.0376	0.072308
	1.5	0.12	65	24	0.637821	995	0.047361	0.084574
	1.5	0.24	41	36	0.563008	831	0.344981	0.453922
	3	0.015	48	28	0.600446	807	0.147524	0.230507
	3	0.03	45	31	0.502509	701	0.974704	0.974704
	3	0.06	56	31	0.668779	1161	0.009531	0.038575
	3	0.12	51	36	0.649237	1192	0.01842	0.052495
	3	0.24	61	38	0.632873	1467	0.026934	0.056112
	6	0.015	46	22	0.524704	531	0.748078	0.787879
	6	0.03	41	21	0.713124	614	0.006491	0.033192
	6	0.06	36	25	0.556667	501	0.458955	0.573694
	6	0.12	101	34	0.707047	2428	0.000316	0.007909
	6	0.24	57	52	0.433198	1284	0.230847	0.32062
	12	0.015	63	21	0.715042	946	0.003349	0.02791
	12	0.03	62	34	0.51945	1095	0.756364	0.787879
	12	0.06	77	34	0.632544	1656	0.026646	0.056112
	12	0.12	41	34	0.530846	740	0.651042	0.73982
	12	0.24	65	36	0.653846	1530	0.010801	0.038575
	V1-AL visually locked unit pair groups							
	TF (Hz)	SF (cpd)	Post unit pair N	Pre unit pair N	CLES	U-val	p-val	p-corr
	0.75	0.015	50	98	0.636735	3120	0.006643	0.015097
	0.75	0.03	61	93	0.651683	3697	0.001488	0.005315
	0.75	0.06	52	108	0.564637	3171	0.186634	0.245617
	0.75	0.12	32	109	0.569954	1988	0.230702	0.274645
	0.75	0.24	56	173	0.523844	5075	0.592712	0.644083
	1.5	0.015	50	105	0.635429	3336	0.006535	0.015097
	1.5	0.03	80	113	0.627323	5671	0.002617	0.008178
	1.5	0.06	68	110	0.654278	4894	0.000554	0.002769
	1.5	0.12	94	110	0.745455	7708	1.56E-09	3.91E-08
	1.5	0.24	74	149	0.554417	6113	0.186355	0.245617
	3	0.015	41	110	0.444346	2004	0.294609	0.334782
	3	0.03	76	111	0.642129	5417	0.000978	0.004076
	3	0.06	60	95	0.60807	3466	0.023753	0.049486
	3	0.12	64	113	0.559873	4049	0.186669	0.245617
	3	0.24	56	147	0.556365	4580	0.215344	0.26918
	6	0.015	77	141	0.726167	7884	3.48E-08	4.35E-07
	6	0.03	94	120	0.678989	7659	7.12E-06	5.94E-05
	6	0.06	68	114	0.628999	4876	0.003649	0.010137
	6	0.12	82	151	0.579309	7173	0.045775	0.081742
	6	0.24	67	171	0.520817	5967	0.618319	0.644083
	12	0.015	68	112	0.598477	4558	0.027011	0.051944

	12	0.03	64	165	0.567045	5988	0.115809	0.193015
	12	0.06	52	230	0.495234	5923	0.915277	0.915277
	12	0.12	58	148	0.56815	4877	0.128774	0.201209
	12	0.24	103	195	0.648145	13018	2.61E-05	0.000163
	V1-AL post-stimulus unit pair groups							
	TF (Hz)	SF (cpd)	Post unit pair N	Pre unit pair N	CLES	U-val	p-val	p-corr
	0.75	0.015	24	55	0.417424	551	0.24743	0.475827
	0.75	0.03	35	37	0.582239	754	0.232375	0.475827
	0.75	0.06	32	46	0.346467	510	0.02198	0.137377
	0.75	0.12	37	56	0.510618	1058	0.865985	0.905563
	0.75	0.24	54	56	0.675595	2043	0.001514	0.012619
	1.5	0.015	29	53	0.372154	572	0.057309	0.204673
	1.5	0.03	46	64	0.443274	1305	0.312993	0.558916
	1.5	0.06	48	54	0.574846	1490	0.194533	0.442121
	1.5	0.12	36	44	0.725379	1149	0.000565	0.007067
	1.5	0.24	44	33	0.550275	799	0.455502	0.669856
	3	0.015	38	60	0.450877	1028	0.416229	0.650358
	3	0.03	40	39	0.476282	743	0.720409	0.900512
	3	0.06	28	45	0.511905	645	0.86934	0.905563
	3	0.12	39	44	0.598485	1027	0.124191	0.310477
	3	0.24	20	56	0.479464	537	0.790693	0.905563
	6	0.015	28	46	0.611801	788	0.109734	0.304818
	6	0.03	68	48	0.710172	2318	0.000122	0.003043
	6	0.06	33	34	0.645276	724	0.041555	0.173146
	6	0.12	28	65	0.507143	923	0.916623	0.916623
	6	0.24	44	62	0.48717	1329	0.824933	0.905563
	12	0.015	35	42	0.440816	648	0.376203	0.627006
	12	0.03	33	56	0.468074	865	0.619255	0.819835
	12	0.06	34	46	0.532609	833	0.623075	0.819835
	12	0.12	25	56	0.385714	540	0.102949	0.304818
	12	0.24	47	57	0.619634	1660	0.036612	0.173146

Extended Table 8-1. Statistics for synchrony index comparisons between post- and pre-entrainment of SF and TF that matched AL's functional preference for each functional group.

Extended Table 8-1, statistics for synchrony index comparisons between post- and pre-entrainment of SF and TF that matched AL's functional preference for each functional group								
	V1-LM visually locked unit pair groups							
	TF (Hz)	SF (cpd)	Post unit pair N	Pre unit pair N	CLES	U-val	p-val	p-corr
Entrainment of SF and TF that matched AL's functional preference	0.75	0.015	44	44	0.247934	480	4.73E-05	0.000296
	0.75	0.03	50	22	0.57	627	0.349697	0.485943
	0.75	0.06	66	36	0.443603	1054	0.349879	0.485943
	0.75	0.12	50	20	0.769	769	0.000482	0.002008
	0.75	0.24	54	45	0.557613	1355	0.326935	0.485943
	1.5	0.015	41	44	0.402993	727	0.124862	0.222968
	1.5	0.03	59	42	0.510492	1265	0.860527	0.860527
	1.5	0.06	40	47	0.458511	862	0.509226	0.578666
	1.5	0.12	68	33	0.456774	1025	0.484724	0.577052
	1.5	0.24	94	49	0.5901	2718	0.077887	0.164017
	3	0.015	37	61	0.257421	581	6.11E-05	0.000305
	3	0.03	51	40	0.193137	394	5.69E-07	7.11E-06
	3	0.06	48	36	0.401042	693	0.12329	0.222968
	3	0.12	35	55	0.243117	468	4.34E-05	0.000296
	3	0.24	56	48	0.515253	1385	0.791718	0.860527
	6	0.015	50	49	0.453061	1110	0.422939	0.528674
	6	0.03	184	36	0.783062	5187	8.01E-08	2.00E-06
	6	0.06	96	48	0.600043	2765	0.050991	0.141643
	6	0.12	56	28	0.375638	589	0.064956	0.162391
	6	0.24	68	35	0.606303	1443	0.078728	0.164017
	12	0.015	84	47	0.510638	2016	0.842152	0.860527
	12	0.03	95	60	0.558772	3185	0.219141	0.365234
	12	0.06	80	42	0.674702	2267	0.001576	0.005628
	12	0.12	75	49	0.386395	1420	0.033065	0.103328
	12	0.24	48	53	0.449686	1144	0.385917	0.507785
	V1-LM post-stimulus unit pair groups							
	TF (Hz)	SF (cpd)	Post unit pair N	Pre unit pair N	CLES	U-val	p-val	p-corr
	0.75	0.015	35	49	0.48863	838	0.863134	0.907004
	0.75	0.03	41	62	0.36664	932	0.022573	0.112867
	0.75	0.06	42	57	0.507101	1214	0.907004	0.907004
	0.75	0.12	23	44	0.568182	575	0.3657	0.609686
	0.75	0.24	34	48	0.408088	666	0.15939	0.398476
	1.5	0.015	17	40	0.367647	250	0.118488	0.329133

	1.5	0.03	30	52	0.425641	664	0.266175	0.554531
	1.5	0.06	21	58	0.468801	571	0.677298	0.806307
	1.5	0.12	22	48	0.433712	458	0.379264	0.609686
	1.5	0.24	33	48	0.44697	708	0.422213	0.620901
	3	0.015	21	58	0.448276	546	0.48794	0.636614
	3	0.03	42	43	0.508306	918	0.898582	0.907004
	3	0.06	26	68	0.617081	1091	0.080906	0.288951
	3	0.12	29	62	0.491657	884	0.901711	0.907004
	3	0.24	32	49	0.358418	562	0.032366	0.13486
	6	0.015	32	40	0.546875	700	0.500132	0.636614
	6	0.03	48	39	0.60203	1127	0.103973	0.324915
	6	0.06	32	57	0.444627	811	0.390199	0.609686
	6	0.12	28	64	0.324777	582	0.007809	0.065075
	6	0.24	28	93	0.285714	744	0.000612	0.007646
	12	0.015	35	52	0.43956	800	0.343219	0.609686
	12	0.03	18	51	0.301743	277	0.013129	0.082055
	12	0.06	33	65	0.429371	921	0.256331	0.554531
	12	0.12	28	57	0.261278	417	0.000374	0.007646
	12	0.24	27	73	0.456621	900	0.509291	0.636614
	V1-AL visually locked unit pair groups							
	TF (Hz)	SF (cpd)	Post unit pair N	Pre unit pair N	CLES	U-val	p-val	p-corr
	0.75	0.015	30	78	0.57265	1340	0.244982	0.382785
	0.75	0.03	52	68	0.718609	2541	4.29E-05	0.001073
	0.75	0.06	30	96	0.647917	1866	0.014801	0.037003
	0.75	0.12	15	108	0.564815	915	0.419276	0.616582
	0.75	0.24	53	145	0.482498	3708	0.707393	0.805911
	1.5	0.015	44	85	0.663904	2483	0.002343	0.009763
	1.5	0.03	44	85	0.648663	2426	0.005785	0.018078
	1.5	0.06	38	85	0.626006	2022	0.026078	0.054329
	1.5	0.12	28	103	0.63939	1844	0.024184	0.054329
	1.5	0.24	45	102	0.627015	2878	0.014357	0.037003
	3	0.015	64	113	0.652793	4721	0.000746	0.00466
	3	0.03	39	107	0.524323	2188	0.655082	0.805911
	3	0.06	35	90	0.719365	2266	0.000147	0.001731
	3	0.12	35	103	0.710402	2561	0.000208	0.001731
	3	0.24	18	128	0.467882	1078	0.661749	0.805911
	6	0.015	44	115	0.591107	2991	0.076245	0.136151
	6	0.03	39	126	0.596052	2929	0.07054	0.135654
	6	0.06	28	97	0.4919	1336	0.898691	0.898691
	6	0.12	28	136	0.480042	1828	0.741438	0.805911
	6	0.24	24	131	0.485051	1525	0.818087	0.852174
	12	0.015	54	92	0.648148	3220	0.002869	0.010247

	12	0.03	51	123	0.425315	2668	0.121786	0.202977
	12	0.06	36	164	0.518462	3061	0.730076	0.805911
	12	0.12	25	113	0.711858	2011	0.000947	0.004735
	12	0.24	36	151	0.468175	2545	0.554453	0.770074
	V1-AL post-stimulus unit pair groups							
	TF (Hz)	SF (cpd)	Post unit pair N	Pre unit pair N	CLES	U-val	p-val	p-corr
	0.75	0.015	15	47	0.547518	386	0.587526	0.77306
	0.75	0.03	19	42	0.684211	546	0.022516	0.064509
	0.75	0.06	10	48	0.591667	284	0.370555	0.617592
	0.75	0.12	18	48	0.512731	443	0.879836	0.956344
	0.75	0.24	27	79	0.582278	1242	0.204462	0.425963
	1.5	0.015	22	57	0.582935	731	0.257645	0.49547
	1.5	0.03	17	46	0.476982	373	0.786407	0.936199
	1.5	0.06	31	56	0.866935	1505	1.69E-08	4.22E-07
	1.5	0.12	13	45	0.45641	267	0.641107	0.801384
	1.5	0.24	19	37	0.769559	541	0.001073	0.005365
	3	0.015	26	44	0.557692	638	0.42595	0.665547
	3	0.03	19	39	0.68556	508	0.023223	0.064509
	3	0.06	19	33	0.778309	488	0.000945	0.005365
	3	0.12	9	48	0.509259	220	0.938945	0.978068
	3	0.24	13	61	0.519546	412	0.831275	0.944631
	6	0.015	18	47	0.799054	676	0.000214	0.001785
	6	0.03	35	35	0.820408	1005	4.14E-06	5.17E-05
	6	0.06	23	38	0.580092	507	0.301021	0.537538
	6	0.12	16	50	0.5625	450	0.458905	0.674861
	6	0.24	23	59	0.545321	740	0.528931	0.734626
	12	0.015	22	43	0.742072	702	0.001536	0.0064
	12	0.03	21	55	0.722944	835	0.002833	0.010118
	12	0.06	8	59	0.722458	341	0.04175	0.094887
	12	0.12	15	77	0.331602	383	0.040316	0.094887
	12	0.24	8	61	0.502049	245	0.992666	0.992666

REFERENCES

Adamantidis AR, Gutierrez Herrera C, Gent TC (2019) Oscillating circuitries in the sleeping brain. Nat Rev Neurosci 20:746-762.

Adesnik H, Bruns W, Taniguchi H, Huang ZJ, Scanziani M (2012) A neural circuit for spatial summation in visual cortex. Nature 490:226-231.

Andermann ML, Kerlin AM, Roumis DK, Glickfeld LL, Reid RC (2011) Functional specialization of mouse higher visual cortical areas. Neuron 72:1025-1039.

Aydore S, Pantazis D, Leahy RM (2013) A note on the phase locking value and its properties. Neuroimage 74:231-244.

Bartos M, Vida I, Jonas P (2007) Synaptic mechanisms of synchronized gamma oscillations in inhibitory interneuron networks. Nat Rev Neurosci 8:45-56.

Bastos AM, Vezoli J, Fries P (2015a) Communication through coherence with inter-areal delays. Curr Opin Neurobiol 31:173-180.

Bastos AM, Usrey WM, Adams RA, Mangun GR, Fries P, Friston KJ (2012) Canonical microcircuits for predictive coding. Neuron 76:695-711.

Bastos AM, Vezoli J, Bosman CA, Schoffelen JM, Oostenveld R, Dowdall JR, De Weerd P, Kennedy H, Fries P (2015b) Visual areas exert feedforward and feedback influences through distinct frequency channels. Neuron 85:390-401.

Benner EJ, Luciano D, Jo R, Abdi K, Paez-Gonzalez P, Sheng H, Warner DS, Liu C, Eroglu C, Kuo CT (2013) Protective astrogenesis from the SVZ niche after injury is controlled by Notch modulator Thbs4. Nature 497:369-373.

Blanchard JW, Eade KT, Szűcs A, Lo Sardo V, Tsunemoto RK, Williams D, Sanna PP, Baldwin KK (2014) Selective conversion of fibroblasts into peripheral sensory neurons. Nature Neuroscience 18:25.

Brulet R, Matsuda T, Zhang L, Miranda C, Giacca M, Kaspar BK, Nakashima K, Hsieh J (2017) NEUROD1 Instructs Neuronal Conversion in Non-Reactive Astrocytes. Stem Cell Reports 8:1506-1515.

Buzsaki G, Draguhn A (2004) Neuronal oscillations in cortical networks. Science 304:1926-1929.

Cardin JA (2018) Inhibitory Interneurons Regulate Temporal Precision and Correlations in Cortical Circuits. Trends Neurosci 41:689-700.

Chen G, Wernig M, Berninger B, Nakafuku M, Parmar M, Zhang CL (2015) In Vivo Reprogramming for Brain and Spinal Cord Repair. eNeuro 2.

Chen G, Zhang Y, Li X, Zhao XC, Ye Q, Lin YX, Tao HZW, Rasch MJ, Zhang XH (2017) Distinct Inhibitory Circuits Orchestrate Cortical beta and gamma Band Oscillations. Neuron 96:1403-+.

Chen YC, Ma NX, Pei ZF, Wu Z, Do-Monte FH, Keefe S, Yellin E, Chen MS, Yin JC, Lee G, Minier-Toribio A, Hu Y, Bai YT, Lee K, Quirk GJ, Chen G (2020) A NeuroD1 AAV-Based Gene Therapy for Functional Brain Repair after Ischemic Injury through In Vivo Astrocyte-to-Neuron Conversion. Mol Ther 28:217-234.

Chubykin AA, Roach EB, Bear MF, Shuler MG (2013) A cholinergic mechanism for reward timing within primary visual cortex. Neuron 77:723-735.

Connors BW, Gutnick MJ (1990) Intrinsic firing patterns of diverse neocortical neurons. Trends Neurosci 13:99-104.

D'Souza RD, Wang Q, Ji W, Meier AM, Kennedy H, Knoblauch K, Burkhalter A (2022) Hierarchical and nonhierarchical features of the mouse visual cortical network. Nat Commun 13:503.

Dadarlat MC, Stryker MP (2017) Locomotion Enhances Neural Encoding of Visual Stimuli in Mouse V1. J Neurosci 37:3764-3775.

Douglas RM, Neve A, Quittenbaum JP, Alam NM, Prusky GT (2006) Perception of visual motion coherence by rats and mice. Vision Res 46:2842-2847.

Engel AK, Kreiter AK, Konig P, Singer W (1991) Synchronization of oscillatory neuronal responses between striate and extrastriate visual cortical areas of the cat. Proc Natl Acad Sci U S A 88:6048-6052.

Erdo F, Buhrle C, Blunk J, Hoehn M, Xia Y, Fleischmann B, Focking M, Kustermann E, Kolossov E, Hescheler J, Hossmann KA, Trapp T (2003) Host-dependent tumorigenesis of embryonic stem cell transplantation in experimental stroke. Journal of cerebral blood flow and metabolism : official journal of the International Society of Cerebral Blood Flow and Metabolism 23:780-785.

Faiz M, Sachewsky N, Gascon S, Bang KW, Morshead CM, Nagy A (2015) Adult Neural Stem Cells from the Subventricular Zone Give Rise to Reactive Astrocytes in the Cortex after Stroke. Cell stem cell 17:624-634.

Falkner S, Grade S, Dimou L, Conzelmann KK, Bonhoeffer T, Gotz M, Hubener M (2016) Transplanted embryonic neurons integrate into adult neocortical circuits. Nature 539:248-253.

Fiser A, Mahringer D, Oyibo HK, Petersen AV, Leinweber M, Keller GB (2016) Experience-dependent spatial expectations in mouse visual cortex. Nat Neurosci 19:1658-1664.

Fitch MT, Silver J (2008) CNS injury, glial scars, and inflammation: Inhibitory extracellular matrices and regeneration failure. Exp Neurol 209:294-301.

Fournier J, Saleem AB, Diamanti EM, Wells MJ, Harris KD, Carandini M (2020) Mouse Visual Cortex Is Modulated by Distance Traveled and by Theta Oscillations. Current Biology 30:3811-+.

Frenkel MY, Sawtell NB, Diogo AC, Yoon B, Neve RL, Bear MF (2006) Instructive effect of visual experience in mouse visual cortex. Neuron 51:339-349.

Fries P (2005) A mechanism for cognitive dynamics: neuronal communication through neuronal coherence. Trends Cogn Sci 9:474-480.

Gao M, Lim S, Chubykin AA (2021) Visual Familiarity Induced 5-Hz Oscillations and Improved Orientation and Direction Selectivities in V1. J Neurosci 41:2656-2667.

Garner AR, Keller GB (2022) A cortical circuit for audio-visual predictions. Nat Neurosci 25:98-105.

Garrett ME, Nauhaus I, Marshel JH, Callaway EM (2014) Topography and areal organization of mouse visual cortex. J Neurosci 34:12587-12600.

Ge LJ, Yang FH, Li W, Wang T, Lin Y, Feng J, Chen NH, Jiang M, Wang JH, Hu XT, Chen G (2020) In vivo Neuroregeneration to Treat Ischemic Stroke Through NeuroD1 AAV-Based Gene Therapy in Adult Non-human Primates. Front Cell Dev Biol 8:590008.

Glickfeld LL, Histed MH, Maunsell JH (2013a) Mouse primary visual cortex is used to detect both orientation and contrast changes. J Neurosci 33:19416-19422.

Glickfeld LL, Reid RC, Andermann ML (2014) A mouse model of higher visual cortical function. Curr Opin Neurobiol 24:28-33.

Glickfeld LL, Andermann ML, Bonin V, Reid RC (2013b) Cortico-cortical projections in mouse visual cortex are functionally target specific. Nat Neurosci 16:219-226.

Goldbach HC, Akitake B, Leedy CE, Histed MH (2021) Performance in even a simple perceptual task depends on mouse secondary visual areas. Elife 10.

Goltstein PM, Reinert S, Bonhoeffer T, Hubener M (2021) Mouse visual cortex areas represent perceptual and semantic features of learned visual categories. Nat Neurosci 24:1441-1451.

Gorenberg EL, Chandra SS (2017) The Role of Co-chaperones in Synaptic Proteostasis and Neurodegenerative Disease. Front Neurosci 11:248.

Gouwens NW et al. (2019) Classification of electrophysiological and morphological neuron types in the mouse visual cortex. Nat Neurosci 22:1182-1195.

Grade S, Gotz M (2017) Neuronal replacement therapy: previous achievements and challenges ahead. NPJ Regen Med 2:29.

Grande A, Sumiyoshi K, Lopez-Juarez A, Howard J, Sakthivel B, Aronow B, Campbell K, Nakafuku M (2013) Environmental impact on direct neuronal reprogramming in vivo in the adult brain. Nat Commun 4:2373.

Guo Z, Zhang L, Wu Z, Chen Y, Wang F, Chen G (2014) In vivo direct reprogramming of reactive glial cells into functional neurons after brain injury and in an Alzheimer's disease model. Cell Stem Cell 14:188-202.

Han H-B, Lee KE, Choi JH (2019) Functional Dissociation of θ Oscillations in the Frontal and Visual Cortices and Their Long-Range Network during Sustained Attention. eneuro 6:ENEURO.0248-0219.2019.

Han X, Vermaercke B, Bonin V (2020) Cellular organization of visual information processing channels in the mouse visual cortex. bioRxiv:441014.

Han Y, Kebschull JM, Campbell RAA, Cowan D, Imhof F, Zador AM, Mrsic-Flogel TD (2018) The logic of single-cell projections from visual cortex. Nature 556:51-56.

Harris KD, Shepherd GM (2015) The neocortical circuit: themes and variations. Nat Neurosci 18:170-181.

Harrison SA, Tong F (2009) Decoding reveals the contents of visual working memory in early visual areas. Nature 458:632-635.

Heinrich C, Bergami M, Gascon S, Lepier A, Vigano F, Dimou L, Sutor B, Berninger B, Gotz M (2014) Sox2-mediated conversion of NG2 glia into induced neurons in the injured adult cerebral cortex. Stem Cell Reports 3:1000-1014.

Henze DA, Borhegyi Z, Csicsvari J, Mamiya A, Harris KD, Buzsaki G (2000) Intracellular features predicted by extracellular recordings in the hippocampus in vivo. J Neurophysiol 84:390-400.

Hoy JL, Yavorska I, Wehr M, Niell CM (2016) Vision Drives Accurate Approach Behavior during Prey Capture in Laboratory Mice. Curr Biol 26:3046-3052.

Huang P, Xiang X, Chen X, Li H (2020a) Somatostatin Neurons Govern Theta Oscillations Induced by Salient Visual Signals. Cell Rep 33:108415.

Huang PC, Xiang XK, Chen XF, Li HH (2020b) Somatostatin Neurons Govern Theta Oscillations Induced by Salient Visual Signals. Cell Reports 33.

Huerta PT, Lisman JE (1995) Bidirectional synaptic plasticity induced by a single burst during cholinergic theta oscillation in CA1 in vitro. Neuron 15:1053-1063.

Huh CYL, Peach JP, Bennett C, Vega RM, Hestrin S (2018) Feature-Specific Organization of Feedback Pathways in Mouse Visual Cortex. Curr Biol 28:114-120 e115.

Jia X, Tanabe S, Kohn A (2013) gamma and the coordination of spiking activity in early visual cortex. Neuron 77:762-774.

Jin M, Glickfeld LL (2020) Mouse Higher Visual Areas Provide Both Distributed and Specialized Contributions to Visually Guided Behaviors. Curr Biol 30:4682-4692 e4687.

Juavinett AL, Kim EJ, Collins HC, Callaway EM (2020) A systematic topographical relationship between mouse lateral posterior thalamic neurons and their visual cortical projection targets. J Comp Neurol 528:95-107.

Jurjut O, Georgieva P, Busse L, Katzner S (2017) Learning Enhances Sensory Processing in Mouse V1 before Improving Behavior. J Neurosci 37:6460-6474.

Kawano H, Kimura-Kuroda J, Komuta Y, Yoshioka N, Li HP, Kawamura K, Li Y, Raisman G (2012) Role of the lesion scar in the response to damage and repair of the central nervous system. Cell and tissue research 349:169-180.

Keller AJ, Roth MM, Scanziani M (2020) Feedback generates a second receptive field in neurons of the visual cortex. Nature 582:545-549.

Kim MH, Znamenskiy P, Iacaruso MF, Mrsic-Flogel TD (2018) Segregated Subnetworks of Intracortical Projection Neurons in Primary Visual Cortex. Neuron 100:1313-1321 e1316.

Kissinger ST, Pak A, Tang Y, Masmanidis SC, Chubykin AA (2018) Oscillatory Encoding of Visual Stimulus Familiarity. J Neurosci 38:6223-6240.

Kissinger ST, Wu Q, Quinn CJ, Anderson AK, Pak A, Chubykin AA (2020) Visual Experience-Dependent Oscillations and Underlying Circuit Connectivity Changes Are Impaired in Fmr1 KO Mice. Cell Rep 31:107486.

Ko H, Hofer SB, Pichler B, Buchanan KA, Sjostrom PJ, Mrsic-Flogel TD (2011) Functional specificity of local synaptic connections in neocortical networks. Nature 473:87-91.

Kohn A, Jasper AI, Semedo JD, Gokcen E, Machens CK, Yu BM (2020) Principles of Corticocortical Communication: Proposed Schemes and Design Considerations. Trends in Neurosciences 43:725-737.

Lee H, Simpson GV, Logothetis NK, Rainer G (2005) Phase locking of single neuron activity to theta oscillations during working memory in monkey extrastriate visual cortex. Neuron 45:147-156.

Li H, Chen G (2016) In Vivo Reprogramming for CNS Repair: Regenerating Neurons from Endogenous Glial Cells. Neuron 91:728-738.

Li Y, Van Hooser SD, Mazurek M, White LE, Fitzpatrick D (2008) Experience with moving visual stimuli drives the early development of cortical direction selectivity. Nature 456:952-956.

Liebe S, Hoerzer GM, Logothetis NK, Rainer G (2012) Theta coupling between V4 and prefrontal cortex predicts visual short-term memory performance. Nat Neurosci 15:456-462, S451-452.

Lien AD, Scanziani M (2013) Tuned thalamic excitation is amplified by visual cortical circuits. Nat Neurosci 16:1315-1323.

Lien AD, Scanziani M (2018) Cortical direction selectivity emerges at convergence of thalamic synapses. Nature 558:80-86.

Lim S (2019) Mechanisms underlying sharpening of visual response dynamics with familiarity. Elife 8.

Liu BH, Li YT, Ma WP, Pan CJ, Zhang LI, Tao HW (2011) Broad inhibition sharpens orientation selectivity by expanding input dynamic range in mouse simple cells. Neuron 71:542-554.

Makino H, Komiyama T (2015) Learning enhances the relative impact of top-down processing in the visual cortex. Nat Neurosci 18:1116-1122.

Marei HE, Hasan A, Rizzi R, Althani A, Afifi N, Cenciarelli C, Caceci T, Shuaib A (2018) Potential of Stem Cell-Based Therapy for Ischemic Stroke. Front Neurol 9:34.

Marques T, Nguyen J, Fioreze G, Petreanu L (2018) The functional organization of cortical feedback inputs to primary visual cortex. Nat Neurosci 21:757-764.

Marro S, Pang ZP, Yang N, Tsai MC, Qu K, Chang HY, Sudhof TC, Wernig M (2011) Direct lineage conversion of terminally differentiated hepatocytes to functional neurons. Cell Stem Cell 9:374-382.

Marshel JH, Garrett ME, Nauhaus I, Callaway EM (2011) Functional specialization of seven mouse visual cortical areas. Neuron 72:1040-1054.

Mattugini N, Bocchi R, Scheuss V, Russo GL, Torper O, Lao CL, Gotz M (2019) Inducing Different Neuronal Subtypes from Astrocytes in the Injured Mouse Cerebral Cortex. Neuron 103:1086-1095 e1085.

Mazurek M, Kager M, Van Hooser SD (2014) Robust quantification of orientation selectivity and direction selectivity. Front Neural Circuits 8:92.

McAfee SS, Liu Y, Dhamala M, Heck DH (2018) Thalamocortical Communication in the Awake Mouse Visual System Involves Phase Synchronization and Rhythmic Spike Synchrony at High Gamma Frequencies. Front Neurosci 12:837.

Mejias JF, Murray JD, Kennedy H, Wang XJ (2016) Feedforward and feedback frequency-dependent interactions in a large-scale laminar network of the primate cortex. Sci Adv 2:e1601335.

Michalareas G, Vezoli J, van Pelt S, Schoffelen JM, Kennedy H, Fries P (2016) Alpha-Beta and Gamma Rhythms Subserve Feedback and Feedforward Influences among Human Visual Cortical Areas. Neuron 89:384-397.

Michelsen KA, Acosta-Verdugo S, Benoit-Marand M, Espuny-Camacho I, Gaspard N, Saha B, Gaillard A, Vanderhaeghen P (2015) Area-specific reestablishment of damaged circuits in the adult cerebral cortex by cortical neurons derived from mouse embryonic stem cells. Neuron 85:982-997.

Milner AD, Goodale MA (2008) Two visual systems re-viewed. Neuropsychologia 46:774-785.

Minlebaev M, Colonnese M, Tsintsadze T, Sirota A, Khazipov R (2011) Early gamma oscillations synchronize developing thalamus and cortex. Science 334:226-229.

Murakami T, Matsui T, Ohki K (2017) Functional Segregation and Development of Mouse Higher Visual Areas. J Neurosci 37:9424-9437.

Nahmani M, Turrigiano GG (2014) Adult cortical plasticity following injury: Recapitulation of critical period mechanisms? Neuroscience 283:4-16.

Nase G, Singer W, Monyer H, Engel AK (2003) Features of neuronal synchrony in mouse visual cortex. J Neurophysiol 90:1115-1123.

Nauhaus I, Benucci A, Carandini M, Ringach DL (2008) Neuronal selectivity and local map structure in visual cortex. Neuron 57:673-679.

Niell CM, Stryker MP (2008) Highly selective receptive fields in mouse visual cortex. J Neurosci 28:7520-7536.

Niell CM, Scanziani M (2021) How Cortical Circuits Implement Cortical Computations: Mouse Visual Cortex as a Model. Annu Rev Neurosci 44:517-546.

Niu W, Zang T, Zou Y, Fang S, Smith DK, Bachoo R, Zhang CL (2013) In vivo reprogramming of astrocytes to neuroblasts in the adult brain. Nat Cell Biol 15:1164-1175.

Nolbrant S, Giacomoni J, Hoban DB, Bruzelius A, Birtele M, Chandler-Militello D, Pereira M, Ottosson DR, Goldman SA, Parmar M (2020) Direct Reprogramming of Human Fetal- and Stem Cell-Derived Glial Progenitor Cells into Midbrain Dopaminergic Neurons. Stem Cell Reports 15:869-882.

Nurminen L, Angelucci A (2014) Multiple components of surround modulation in primary visual cortex: multiple neural circuits with multiple functions? Vision Res 104:47-56.

Nurminen L, Merlin S, Bijanzadeh M, Federer F, Angelucci A (2018) Top-down feedback controls spatial summation and response amplitude in primate visual cortex. Nat Commun 9:2281.

Ohki K, Reid RC (2007) Specificity and randomness in the visual cortex. Curr Opin Neurobiol 17:401-407.

Okuyama-Uchimura F, Komai S (2016) Mouse Ability to Perceive Subjective Contours. Perception 45:315-327.

Olgiati S et al. (2016) DNAJC6 Mutations Associated With Early-Onset Parkinson's Disease. Ann Neurol 79:244-256.

oude Lohuis MN, Cantón AC, Pennartz CMA, Olcese U (2021) Higher-order visual areas broaden stimulus responsiveness in mouse primary visual cortex. bioRxiv:2021.2002.2016.431393.

Pachitariu M, Steinmetz N, Kadir S, Carandini M, Harris KD (2016) Kilosort: realtime spike-sorting for extracellular electrophysiology with hundreds of channels. bioRxiv:061481.

Pak A, Kissinger ST, Chubykin AA (2021) Impaired Adaptation and Laminar Processing of the Oddball Paradigm in the Primary Visual Cortex of Fmr1 KO Mouse. Front Cell Neurosci 15:668230.

Pak A, Ryu E, Li C, Chubykin AA (2020) Top-Down Feedback Controls the Cortical Representation of Illusory Contours in Mouse Primary Visual Cortex. J Neurosci 40:648-660.

Pakan JMP, Currie SP, Fischer L, Rochefort NL (2018) The Impact of Visual Cues, Reward, and Motor Feedback on the Representation of Behaviorally Relevant Spatial Locations in Primary Visual Cortex. Cell Rep 24:2521-2528.

Peirce JW (2007) PsychoPy--Psychophysics software in Python. J Neurosci Methods 162:8-13.

Piscopo DM, El-Danaf RN, Huberman AD, Niell CM (2013) Diverse visual features encoded in mouse lateral geniculate nucleus. J Neurosci 33:4642-4656.

Poort J, Khan AG, Pachitariu M, Nemri A, Orsolic I, Krupic J, Bauza M, Sahani M, Keller GB, Mrsic-Flogel TD, Hofer SB (2015) Learning Enhances Sensory and Multiple Non-sensory Representations in Primary Visual Cortex. Neuron 86:1478-1490.

Rossant C, Kadir SN, Goodman DFM, Schulman J, Hunter MLD, Saleem AB, Grosmark A, Belluscio M, Denfield GH, Ecker AS, Tolias AS, Solomon S, Buzsaki G, Carandini M, Harris KD (2016) Spike sorting for large, dense electrode arrays. Nat Neurosci 19:634-641.

Rutishauser U, Ross IB, Mamelak AN, Schuman EM (2010) Human memory strength is predicted by theta-frequency phase-locking of single neurons. Nature 464:903-907.

Salkoff DB, Zagha E, Yuzgec O, McCormick DA (2015) Synaptic Mechanisms of Tight Spike Synchrony at Gamma Frequency in Cerebral Cortex. J Neurosci 35:10236-10251.

Schneider M, Broggini AC, Dann B, Tzanou A, Uran C, Sheshadri S, Scherberger H, Vinck M (2021) A mechanism for inter-areal coherence through communication based on connectivity and oscillatory power. Neuron 109:4050-+.

Schuett S, Bonhoeffer T, Hubener M (2002) Mapping retinotopic structure in mouse visual cortex with optical imaging. J Neurosci 22:6549-6559.

Seabrook TA, Burbridge TJ, Crair MC, Huberman AD (2017) Architecture, Function, and Assembly of the Mouse Visual System. Annu Rev Neurosci 40:499-538.

Shen J, Colonnese MT (2016) Development of Activity in the Mouse Visual Cortex. J Neurosci 36:12259-12275.

Sheth BR, Young R (2016) Two Visual Pathways in Primates Based on Sampling of Space: Exploitation and Exploration of Visual Information. Front Integr Neurosci 10:37.

Shobe JL, Claar LD, Parhami S, Bakhurin KI, Masmanidis SC (2015) Brain activity mapping at multiple scales with silicon microprobes containing 1,024 electrodes. Journal of neurophysiology 114:2043-2052.

Siegle JH, Lopez AC, Patel YA, Abramov K, Ohayon S, Voigts J (2017) Open Ephys: an open-source, plugin-based platform for multichannel electrophysiology. J Neural Eng 14:045003.

Siegle JH et al. (2021) Survey of spiking in the mouse visual system reveals functional hierarchy. Nature.

Silver J, Miller JH (2004) Regeneration beyond the glial scar. Nat Rev Neurosci 5:146-156.

Smith IT, Townsend LB, Huh R, Zhu H, Smith SL (2017) Stream-dependent development of higher visual cortical areas. Nat Neurosci 20:200-208.

Smith MA, Kohn A (2008) Spatial and temporal scales of neuronal correlation in primary visual cortex. J Neurosci 28:12591-12603.

Somaa FA, Wang TY, Niclis JC, Bruggeman KF, Kauhausen JA, Guo H, McDougall S, Williams RJ, Nisbet DR, Thompson LH, Parish CL (2017) Peptide-Based Scaffolds Support Human Cortical Progenitor Graft Integration to Reduce Atrophy and Promote Functional Repair in a Model of Stroke. Cell Rep 20:1964-1977.

Spyropoulos G, Bosman CA, Fries P (2018) A theta rhythm in macaque visual cortex and its attentional modulation. Proc Natl Acad Sci U S A 115:E5614-E5623.

Stark E, Eichler R, Roux L, Fujisawa S, Rotstein HG, Buzsaki G (2013) Inhibition-induced theta resonance in cortical circuits. Neuron 80:1263-1276.

Steinbeck JA, Koch P, Derouiche A, Brustle O (2012) Human embryonic stem cell-derived neurons establish region-specific, long-range projections in the adult brain. Cell Mol Life Sci 69:461-470.

Stirman J, Townsend LB, Smith S (2016) A touchscreen based global motion perception task for mice. Vision Res 127:74-83.

Tamura M, Spellman TJ, Rosen AM, Gogos JA, Gordon JA (2017) Hippocampal-prefrontal theta-gamma coupling during performance of a spatial working memory task. Nat Commun 8:2182.

Tang Y, Wu Q, Gao M, Ryu E, Pei Z, Kissinger ST, Chen Y, Rao AK, Xiang Z, Wang T, Li W, Chen G, Chubykin AA (2021) Restoration of Visual Function and Cortical Connectivity After Ischemic Injury Through NeuroD1-Mediated Gene Therapy. Front Cell Dev Biol 9:720078.

Tornero D, Wattananit S, Gronning Madsen M, Koch P, Wood J, Tatarishvili J, Mine Y, Ge R, Monni E, Devaraju K, Hevner RF, Brustle O, Lindvall O, Kokaia Z (2013) Human induced pluripotent stem cell-derived cortical neurons integrate in stroke-injured cortex and improve functional recovery. Brain 136:3561-3577.

Tornero D, Tsupykov O, Granmo M, Rodriguez C, Gronning-Hansen M, Thelin J, Smozhanik E, Laterza C, Wattananit S, Ge R, Tatarishvili J, Grealish S, Brustle O, Skibo G, Parmar M, Schouenborg J, Lindvall O, Kokaia Z (2017) Synaptic inputs from stroke-injured brain to grafted human stem cell-derived neurons activated by sensory stimuli. Brain 140:692-706.

Torper O, Ottosson DR, Pereira M, Lau S, Cardoso T, Grealish S, Parmar M (2015) In Vivo Reprogramming of Striatal NG2 Glia into Functional Neurons that Integrate into Local Host Circuitry. Cell Rep 12:474-481.

Trainito C, von Nicolai C, Miller EK, Siegel M (2019) Extracellular Spike Waveform Dissociates Four Functionally Distinct Cell Classes in Primate Cortex. Curr Biol 29:2973-2982 e2975.

Vallat R (2018a) Pingouin: statistics in Python. Journal of Open Source Software 3.

Vallat R (2018b) Pingouin: statistics in Python. The Journal of Open Source Software 3:1026.

van Kerkoerle T, Self MW, Dagnino B, Gariel-Mathis MA, Poort J, van der Togt C, Roelfsema PR (2014) Alpha and gamma oscillations characterize feedback and feedforward processing in monkey visual cortex. Proc Natl Acad Sci U S A 111:14332-14341.

Veit J, Hakim R, Jadi MP, Sejnowski TJ, Adesnik H (2017) Cortical gamma band synchronization through somatostatin interneurons. Nat Neurosci 20:951-959.

Vierbuchen T, Ostermeier A, Pang ZP, Kokubu Y, Sudhof TC, Wernig M (2010) Direct conversion of fibroblasts to functional neurons by defined factors. Nature 463:1035-1041.

Vinck M, Batista-Brito R, Knoblich U, Cardin JA (2015) Arousal and Locomotion Make Distinct Contributions to Cortical Activity Patterns and Visual Encoding. Neuron 86:740-754.

Vinck M, van Wingerden M, Womelsdorf T, Fries P, Pennartz CM (2010) The pairwise phase consistency: a bias-free measure of rhythmic neuronal synchronization. Neuroimage 51:112-122.

Wang F, Cheng L, Zhang X (2021) Reprogramming Glial Cells into Functional Neurons for Neuro-regeneration: Challenges and Promise. Neurosci Bull 37:1625-1636.

Wang Q, Burkhalter A (2013) Stream-related preferences of inputs to the superior colliculus from areas of dorsal and ventral streams of mouse visual cortex. J Neurosci 33:1696-1705.

Wang Q, Gao E, Burkhalter A (2011) Gateways of ventral and dorsal streams in mouse visual cortex. J Neurosci 31:1905-1918.

Wang Q, Sporns O, Burkhalter A (2012) Network analysis of corticocortical connections reveals ventral and dorsal processing streams in mouse visual cortex. J Neurosci 32:4386-4399.

Wang Y, Dragoi V (2015) Rapid learning in visual cortical networks. Elife 4.

Wu Z, Parry M, Hou XY, Liu MH, Wang H, Cain R, Pei ZF, Chen YC, Guo ZY, Abhijeet S, Chen G (2020) Gene therapy conversion of striatal astrocytes into GABAergic neurons in mouse models of Huntington's disease. Nat Commun 11:1105.

Xiang Z, Xu L, Liu M, Wang Q, Li W, Lei W, Chen G (2021) Lineage tracing of direct astrocyte-to-neuron conversion in the mouse cortex. Neural Regen Res 16:750-756.

Yang N, Ng YH, Pang ZP, Südhof TC, Wernig M (2011) Induced neuronal cells: how to make and define a neuron. Cell stem cell 9:517-525.

Yilmaz M, Meister M (2013) Rapid innate defensive responses of mice to looming visual stimuli. Curr Biol 23:2011-2015.

Yim YI, Sun T, Wu LG, Raimondi A, De Camilli P, Eisenberg E, Greene LE (2010) Endocytosis and clathrin-uncoating defects at synapses of auxilin knockout mice. P Natl Acad Sci USA 107:4412-4417.

Yu Y, Hira R, Stirman JN, Yu W, Smith IT, Smith SL (2018) Mice use robust and common strategies to discriminate natural scenes. Sci Rep 8:1379.

Zhang S, Xu M, Kamigaki T, Hoang Do JP, Chang WC, Jenvay S, Miyamichi K, Luo L, Dan Y (2014a) Selective attention. Long-range and local circuits for top-down modulation of visual cortex processing. Science 345:660-665.

Zhang SY, Xu M, Kamigaki T, Do JPH, Chang WC, Jenvay S, Miyamichi K, Luo LQ, Dan Y (2014b) Long-range and local circuits for top-down modulation of visual cortex processing. Science 345:660-665.

Zhang Y, Zhang X (2021) Portrait of visual cortical circuits for generating neural oscillation dynamics. Cogn Neurodyn 15:3-16.

Zhang Y, Pak C, Han Y, Ahlenius H, Zhang Z, Chanda S, Marro S, Patzke C, Acuna C, Covy J, Xu W, Yang N, Danko T, Chen L, Wernig M, Sudhof TC (2013) Rapid single-step induction of functional neurons from human pluripotent stem cells. Neuron 78:785-798.

Zhuang J, Ng L, Williams D, Valley M, Li Y, Garrett M, Waters J (2017) An extended retinotopic map of mouse cortex. Elife 6.

Zold CL, Hussain Shuler MG (2015) Theta Oscillations in Visual Cortex Emerge with Experience to Convey Expected Reward Time and Experienced Reward Rate. J Neurosci 35:9603-9614.

VITA

Yu Tang

Summary of Qualifications

Highly motivated neuroscientist with broad research experience in *in vivo* neuroscience. Highly skilled in *in vivo* extracellular recording in awake mice, brain slice immunohistochemistry, confocal microscopy imaging, freely moving mouse behavior experiments, optogenetic manipulations, high density electrophysiological data analyses using Python/Matlab, brain slice image analyses using ImageJ/Python/Matlab, machine learning using scikit-learn, basic query and storing operations for SQL database using Python. Publication record demonstrates adaptive and collaborative nature in team projects.

Education

2022 May **Ph.D., Neuroscience**, Purdue University, West Lafayette, USA

2014-2016 **B.S., Biological Sciences**, minor in Psychology, Purdue University, West Lafayette, USA

2012-2014 **B.S., Biological Sciences**, China Agricultural University, Beijing, China

Publications

1. **Y Tang** and AA Chubykin. Visual perceptual experience induces 4-8 Hz synchrony and spike synchrony between V1 and higher-order visual areas. *In preparation.*
2. Hengying Shan, John Peterson III, Nathan J. Conrad, **Yu Tang**, Yuhang Zhu, Shabnam Ghotbi, Sutton Hathorn, Alex Chubykin, Saeed Mohammadi. A 0.43g Wireless Battery-less Neural Recorder with On-chip Microelectrode Array and Integrated Flexible Antenna. *IEEE Microwave and Wireless Components Letters - Manuscript ID MWCL-22-0254*
3. **Y Tang***, Q Wu*, M Gao*, E Ryu, Z Pei, ST Kissinger, Y Chen, A Rao, G Chen, AA Chubykin. Restoration of visual cortical connectivity and function after ischemic injury through NeuroD1-mediated gene therapy. *Frontiers in Cell and Developmental Biology*. *Co-first authors.

4. F Xu*, D Ma*, KP MacPherson, S Liu, Y Bu, Y Wang, **Y Tang**, C Bi, T Kwok, AA Chubykin, P Yin, S Calve, G E. Landreth, F Huang. Three-dimensional nanoscopy of whole cells and tissues with in situ point spread function retrieval. (2020) *Nature Methods* 17(1): 531–540. *Co-first authors.
5. Kissinger ST*, Pak A*, **Tang Y**, Masmanidis S, Chubykin AA**.**, *'Oscillatory encoding of visual stimulus familiarity', Journal of Neuroscience* (July 4, 2018), 38, 27, 6223-6240. *Co-first authors.

Select Research Experience

Project I: Functional characterization of visual cortical recovery following NeuroD1 gene therapy

- Designed, executed, troubleshot, and interpreted experiments (*in vivo* extracellular recording, brain slice immunohistochemistry, confocal microscopy, optogenetics, patch clamp statistics)
- Characterized longitudinal functional recovery in the visual cortex in ischemia following AAV-NeuroD1 gene therapy
- Led the research project with a large collaborative team across multiple research institutes
- Presented the work at multiple conferences and published a scientific paper

Project II: Functional characterization of oscillatory synchrony between visual cortical areas

- Characterized inter-areal circuit dynamics after normal visual experience/learning using high density silicon probes
- Improved data acquisition pipeline to acquire/save larger amount of data at a time
- Implemented inter-areal synchrony analyses using Python
- Mapped brain regions using Allen Mouse Brain Common Coordinate Framework in Matlab
- Conducted pilot freely moving mouse behavior experiments using touch-screen chambers
- Presented the work at multiple conferences, in process of submitting the paper

Project III: Characterization of visual cortical impairments in Auxilin KO mice (Collaboration with a molecular neuroscience group led by Dr. Sreeganga Chandra)

- Characterized visual adaptation impairments in Auxilin KO mice using extracellular recordings
- Interpreted data to reconcile *in vivo* and *ex vivo* experiments and drafted a paper

Project IV: Validation of INSPR, an improved method for single-molecule super-resolution imaging (Collaboration with an optical imaging engineer group led by Dr. Fang Huang**)**

- Prepared brain slice samples for collaborators to image nanoscale structures
- Effectively communicated and discussed experiment details to facilitate project progress
- Assisted in writing a scientific publication

Project V: Validation of a lightweight wireless neural recorder (Collaboration with an electrical device engineer group led by Dr. Saeed Mohammadi)

- Performed neural recorder implantation into living mice
- Assisted in analyzing decoded neural signals
- Assisted in drafting a conference paper

Technical Skills

- ***In vivo* extracellular recording**: Record awake mouse visual cortical activity using high density silicon probes, set up electrophysiology rig and data acquisition pipeline (OpenEphys, Arduino event synchronization), design visual stimulation using PsychoPy/Python/Matlab, implement patterned optogenetic manipulation
- **Brain slice immunohistochemistry:** Mouse perfusion, brain slice immunohistochemistry (staining for NeuN, Satb2, GABA, GFAP, Tbr1, Cux1, Ctip2), confocal microscopy imaging, image data analyses using ImageJ, Python, and Matlab
- **Data analyses:** Implement neural signal analyses (local field potential, single units, synchrony analyses including phase-locking, pairwise phase consistency, cross-correlation and etc.) in Python, analyze high density silicon probe recording data using Matlab/Python, preprocessing brain slice fluorescence images using ImageJ, statistical analyses and machine learning (scikit-learn) in Python, basic query and storing operations for SQL databases (idbs) using Python
- **Animal surgeries**: Stereotaxic mouse surgeries, headplate installation, intracranial virus injection, optogenetics, cranial window installation
- **Freely moving mouse behavior** (touch screen chambers): Set up commercial system (Lafayette instrument) with customized optogenetics implementation, design, execute, and troubleshoot experiments, analyze and interpret data of mouse visual discrimination task (go/no-go) in touch screen chambers (Python)
- **Adobe Illustrator:** Scientific figure editing

Awards and Fellowships

2021	Finalist for the BRAIN initiative Show us your BRAINS competition
2016-2017	Lynn Fellowship, PULSe, Purdue University, USA
2015	HHMI funded undergraduate summer research, Purdue University, USA

Teaching, Mentorship, and Services

2020	Teaching assistant, Data Analysis in Neuroscience using Python
2019	Mentor for undergraduate summer research, SURF, Purdue University
2018	Diversity and Inclusion Chair, PULSe Graduate Student Organization
2017	Teaching volunteer in Science in School events, introduced simple scientific concepts to elementary school students

Professional Activities

Society for Neuroscience

Oral and Poster Presentations

03/2022	**Selected 5-minute thesis oral presentation**, *'Visual experience induces theta synchrony between visual cortices'*, Purdue University
11/2021	Video poster presentation, *'Theta synchrony between mouse primary and lateromedial visual cortices following visual experience'*, Society of Neuroscience meeting, Virtual
07/2021	Poster presentation, *'Visual function recovery after ischemia through NeuroD1 therapy'*, 7th Annual BRAIN Initiative Investigators Meeting, Virtual
05/2021	**Selected oral presentation**, *'Visual function recovery after ischemia through NeuroD1 therapy'*, Spring Reception 2021, Office of Interdisciplinary Graduate Program, Purdue University
10/2019	Poster presentation, '*Cortical feedback modulation of experience-dependent oscillations in V1'*, Society of Neuroscience meeting, Chicago
05/2019	Poster presentation, '*In vivo direct reprogramming restores visually evoked responses after focal stroke'*, OIGP Spring Reception, Purdue University

01/2018 Poster presentation, '*In vivo direct reprogramming restores visually evoked responses after focal stroke'*, BSCI IU/Purdue Symposium, IUPUI

12/2017 Poster presentation, '*In vivo direct reprogramming restores visually evoked responses after focal stroke'*, Indiana CTSI, IUPUI